IVW - Schriftenreihe Band 109
Institut für Verbundwerkstoffe GmbH - Kaiserslautern

Ron Sebastian

Advanced in-situ Measurements within Sliding Contacts

Bibliografische Information Der Deutschen Bibliothek

Die Deutsche Bibliothek verzeichnet diese Publikation in der Deutschen Nationalbibliografie; detaillierte bibliografische Daten sind im Internet über <http://dnb.ddb.de> abrufbar.

Bibliographic information published by Die Deutsche Bibliothek

Die Deutsche Bibliothek lists this publication in the Deutsche Nationalbibliografie; detailed bibliographic data is available in the Internet at <http://dnb.ddb.de>.

Herausgeber: Institut für Verbundwerkstoffe GmbH
Prof. Dr.-Ing. Ulf Breuer
Erwin-Schrödinger-Straße
TU Kaiserslautern, Gebäude 58
67663 Kaiserslautern
http://www.ivw.uni-kl.de

Verlag: Institut für Verbundwerkstoffe GmbH

Druck: Technische Universität Kaiserslautern
ZBT – Abteilung Foto-Repro-Druck

D 386

Als Manuskript gedruckt. Printed in Germany.
ISSN 1615-021X
ISBN 978-3-944440-05-7

Advanced in-situ Measurements within Sliding Contacts

Vom Fachbereich für Maschinenbau und Verfahrenstechnik
der Technischen Universität Kaiserslautern
zur Erlangung des akademischen Grades

Doktor-Ingenieur (Dr.-Ing.)

genehmigte

Dissertation

von

Herrn

Dipl.-Ing. Ron Sebastian

aus Heidelberg

2014

Tag der mündlichen Prüfung:	28.03.2014
Dekan:	Prof. Dr.-Ing. Bernd Sauer
Prüfungsvorsitzender:	Prof. Dr.-Ing. Bernd Sauer
1. Berichterstatter:	Prof. Dr.-Ing. Ulf Breuer
2. Berichterstatter:	Prof. Dr.-Ing. Dr. h.c. mult. Klaus Friedrich

D386

Vorwort

Die vorliegende Arbeit entstand während meiner Tätigkeit als wissenschaftlicher Mitarbeiter in der Abteilung „Werkstoffwissenschaft“ im Kompetenzfeld „Tribologie“ der Institut für Verbundwerkstoffe GmbH an der Technischen Universität Kaiserslautern.

Ich möchte an dieser Stelle Herrn Prof. Dr.-Ing. Ulf Breuer für das entgegengebrachte Vertrauen, sowie für die Förderung meiner Person und meiner Arbeit danken. Darüber hinaus gilt mein Dank Prof. Dr.-Ing. h.c. mult. Klaus Friedrich sowie Prof. Dr.-Ing. Bernd Sauer für die Übernahme des Koreferats bzw. des Prüfungsvorsitzes.

Besonders danken möchte ich an dieser Stelle meinen Kollegen, studentischen Mitarbeitern und Vorgesetzten Moritz Hübler, Markus Hentzel, Joachim Stephan, Ralf Schimmele, Martin Priebe, Hermann Giertzsch, Thorsten Becker, Rolf Walter, Petra Volk, Pia Eichert, Stefan Schmitt, Nicole Pfeiffer, Eugen Padenko, Harald Weber, Mark Dully, Ilona Pointner, Dr. Ga Zhang, Thai Bao Nguyen, Florian Kühn, Joschua Hoffmann, Tobias Kurzschenkel, Joshua Müller, Bai Cheng Jim, Björn Linse, Dr. rer. nat. Martin Gurka sowie Dr. Bernd Wetzel für deren uneingeschränkte Unterstützung und eine unvergessliche Zeit. Für die anregenden Diskussionen über thermoelektrische Effekte danke ich an dieser Stelle außerdem Dr. Hans Sterzel.

Florian Kühn, Henrik Sterzel, Markus Fiehn, Christian Doppler, Markus Bätz, Moritz Hübler und Bai Cheng Jim danke ich für ihre Freundschaft, auf die ich stets uneingeschränkt zählen kann.

Ein besonderer Dank gilt meinen Eltern Heinz und Andrea Sebastian sowie meiner Lebensgefährtin Elise Bart, ohne deren Verständnis, Geduld und Unterstützung in den letzten Jahren diese Arbeit nicht möglich gewesen wäre.

Kaiserslautern, im April 2014 Ron Sebastian

Table of Contents

Table of Figures

Abstract

In recent years the field of polymer tribology experienced a tremendous development leading to an increased demand for highly sophisticated in-situ measurement methods. Therefore, advanced measurement techniques were developed and established in this study. Innovative approaches based on dynamic thermocouple, resistive electrical conductivity, and confocal distance measurement methods were developed in order to in-situ characterize both the temperature at sliding interfaces and real contact area, and furthermore the thickness of transfer films. Although dynamic thermocouple and real contact area measurement techniques were already used in similar applications for metallic sliding pairs, comprehensive modifications were necessary to meet the specific demands and characteristics of polymers and composites since they have significantly different thermal conductivities and contact kinematics. By using tribologically optimized PEEK compounds as reference a new measurement and calculation model for the dynamic thermocouple method was set up. This method allows the determination of hot spot temperatures for PEEK compounds, and it was found that they can reach up to 1000 °C in case of short carbon fibers present in the polymer. With regard to the non-isotropic characteristics of the polymer compound, the contact situation between short carbon fibers and steel counterbody could be successfully monitored by applying a resistive measurement method for the real contact area determination. Temperature compensation approaches were investigated for the transfer film layer thickness determination, resulting in in-situ measurements with a resolution of ~0.1 µm. In addition to a successful implementation of the measurement systems, failure mechanism processes were clarified for the PEEK compound used. For the first time in polymer tribology the behavior of the most interesting system parameters could be monitored simultaneously under increasing load conditions. It showed an increasing friction coefficient, wear rate, transfer film layer thickness, and specimen overall temperature when frictional energy exceeded the thermal transport capabilities of the specimen. In contrast, the real contact area between short carbon fibers and steel decreased due to the separation effect caused by the transfer film layer. Since the sliding contact was more and more matrix dominated, the hot spot temperatures on the fibers dropped, too. The results of this failure mechanism investigation already demonstrate the opportunities which the new measurement techniques provide for a deeper understanding of tribological processes, enabling improvements in material composition and application design.

Kurzfassung

Der Bedarf an tribologisch optimierten Werkstoffen nimmt im Zuge immer höherer Anforderungen an energetisch optimierte Baugruppen stetig zu. Insbesondere sind polymere Verbundwerkstoffe aufgrund ihrer hervorragenden intrinsischen Eigenschaften im Fokus der Forschung. Neben einem geringeren Gewicht gegenüber metallischen Gleitpaarungen, den inhärenten Notlaufeigenschaften sowie günstigen Produktionskosten, zeichnet sie insbesondere die Möglichkeit aus, dass, mittels Variation diverser Füllstoffe, maßgeschneiderte Materialien für spezifische Applikationen hergestellt werden können.

Die Entwicklung von polymeren Verbundwerkstoffen findet oftmals auf abstrahierten Modellprüfständen statt. Hierbei werden üblicherweise makroskopische Gleiteigenschaften wie etwa die Reibkraft bzw. der Reibungskoeffizient sowie der Verschleiß gemessen. Zusätzlich werden vergleichsweise einfache Messungen, z.B. Oberflächentemperaturen von Probe und Gegenkörper, ermittelt. Weitergehende Untersuchungen finden zumeist ex-situ, d.h. nach Prüfung der Gleiteigenschaften, mittels zusätzlicher Analytik, wie Mikroskopie oder auch Profilometrie, statt. Die Erfassung solcher Informationen liefert niemals die Historie, sondern immer nur eine Momentaufnahme und ist mit erheblichem zusätzlichem Aufwand verbunden. Kontinuierlich gewonnene Informationen zur Historie von Parametern und tribologischen Kennwerten sind aber von großem Wert, um ein tieferes Verständnis des tribologischen Systems zu gewinnen. Gerade durch die steigende Anzahl möglicher Füllstoffe, welche sich in den letzten Jahren um eine Vielzahl von nanoskaligen Partikeln erweitert hat, ist es unerlässlich, Mechanismen und Struktur-Eigenschaftsbeziehungen detailliert abzubilden und zu überwachen. Dies ermöglicht die Durchführung einer kosteneffiziente Entwicklung von maßgeschneiderten Hochleistungspolymeren. Neben einer Verbesserung bestehender Werkstoffrezepturen könnten detaillierte Systemkenntnisse auch neue Wege in der Grundlagenforschung eröffnen.

Ingenieure und Werkstoffwissenschaftler wollen über einfach anwendbare und möglichst exakte Messmöglichkeiten verfügen, die ihnen eine effiziente Werkstoffentwicklung ermöglichen. Solche Messmethoden sind in der Polymertribologie noch wenig verbreitet. Jedoch gibt es bereits für metallische Reibpartner eine Vielzahl von Verfahren, welche Aufschlüsse über wichtige Systemparameter geben können. Ziel dieser Arbeit ist die systematische Entwicklung von neuen, in-situ fähigen Messmethoden zur Anwendung in kontinuierlichen Gleitprozessen zwischen polymerbasierten Verbundwerkstoffen und metallischem Gegenkörpern.

Bevor die eigentliche Entwicklung und Integration der neuen Messmethoden durchgeführt werden kann, war zunächst die theoretische Aufarbeitung des aktuellen Standes der Technik im Hinblick auf das tribologische System für polymere Verbundwerkstoffe und dessen Charakteristiken nötig. Hierdurch konnten wesentliche Parameter, welche für den Gleitprozess von entscheidender Bedeutung sind, herausgearbeitet werden. In einem nächsten Schritt wurden Messmethoden aus der Tribologie der Metalle analysiert; hierzu zählen Methoden zur Messung der realen Kontaktfläche zwischen beiden Gleitpartnern sowie der Dicke eines Zwischenstoffes und der Kontakttemperatur.

Auf dieser Basis wurden schließlich für die folgenden Kenngrößen Messmethoden ausgewählt und entwickelt, deren Transfer für polymere Verbundwerkstoffe vielversprechend erschien, wenn auch stellenweise eine starke Anpassung an die neuen Systemgegebenheiten erforderlich war:

1) Die elektrische Durchgangsleitfähigkeit der Gleitkontaktpaarung. Sie ist systembedingt abhängig von Reib- und Verschleißmechanismen, da Sie von der realen Kontaktfläche zwischen elektrisch leitfähigen Fasern und Reibpartner determiniert wird.

2) Die Entstehungshistorie von Tribofilmen (Zwischenschichten) auf dem Gegenkörper, die durch konfokale Distanzmessung erfasst und analysiert wurde.

3) Reale Kontakttemperaturen („Blitztemperaturen“), die durch Bildung eines dynamischen Thermoelementes mittels der elektrisch leitfähigen Reibpartner ermittelt wurden.

Für 1) und 3) wurden neue theoretische Modelle erstellt, wobei die mathematische Beschreibung für die Berechnung von Kontakttemperaturen sowie der experimentelle Aufbau für die Validierung angepasst wurden. Aufgrund starker Diskrepanzen zwischen dem Stand der Technik und eigenen experimentellen Beobachtungen mussten insbesondere für die Messung der Kontakttemperaturen zusätzliche theoretische Überlegungen und praktische Experimente angestellt werden. Besonderes Augenmerk wurde auf die Auswirkungen äußerer Einflüsse gelegt. Bei der Dickenbestimmung des Zwischenstoffes mittels konfokaler Distanzmessung würde beispielsweise ohne Temperaturkompensation das Messergebnis vorrangig die Temperaturausdehnung des Gegenkörpers liefern, da diese das eigentliche Messergebnis um bis zu zwei Dekaden überlagert.

Für jede der Messmethoden wurde nach erfolgter technischer Implementierung eine systematische Validierung durchgeführt. Unter verschiedenen, wechselnden Belastungszuständen gewonnene Messergebnisse wurden analysiert und mit anderen experimentellen Daten sowie Berechnungen korreliert.

Eine im Hinblick auf örtliches als auch zeitliches Auflösungsvermögen bislang nicht erreichte Performance mit einer Wiederholgenauigkeit von besser als 0,1 µm konnte gezeigt werden. Die Bestimmung der Dicke eines Zwischenstoffes konnte nur für Trockenreibung etabliert werden.

Eine spezielle Versuchsreihe wurde mit einem Referenzwerkstoff durchgeführt, um die neu entwickelten Messmethoden kombiniert unter Trockenreibung mit Augenmerk auf den Versagenspunkt eines Materials unter steigender tribologischer Belastung einzusetzen. Der Werkstoff entsprach hierbei einem industriell eingesetzten Verbundwerkstoff auf Basis von Polyetheretherketon, gefüllt mit Kurzkohlenstofffasern, Graphit sowie Zinksulfid und Titaniumdioxid. Starke Abhängigkeiten zwischen Reibkoeffizient, Transferfilmdicke, realer Kontaktfläche sowie Kontakttemperatur waren ersichtlich. Damit konnte ein klares Verständnis dafür geschaffen werden, wie es zu einem thermischen Kollaps des tribologischen Systems durch Reibwärme oder durch zusätzlich eingebrachte thermische Energie kommt. Während eine steigende mechanische Belastung zu lokaler, mikroskopischer Überhitzung und somit zu schnell fortschreitendem Verschleiß führt, konnte für die von außen zugeführte thermische Wärmeenergie makroskopisches Versagen der Matrix als Auslöser für das finale Versagen des tribologischen Systems identifiziert werden.

Wie durch die beispielhafte Untersuchung gezeigt werden konnte, ermöglichen die neuen Messmethoden eine wirtschaftliche und tiefgreifende Untersuchung sowie online Überwachung von tribologischen Systemen. Struktur-Eigenschaftsbeziehungen können zukünftig noch besser korreliert werden, was eine optimale Materialentwicklung ermöglicht. Insbesondere die Erkenntnisse thermischer Systemeigenschaften können direkt bei der konstruktiven Auslegung von Gleitlagern angewendet werden.

Abbreviations and Variables

Abbreviations

AFM	Atomic Force Microscope
BoR	Block-on-Ring
CCD	Charge-Coupled-Device
CNT	Carbon Nanotubes
CoF	Friction Coefficient
CuO	Copper Oxide
DAQ	Data Acquisition
EHD	Elastohydrodynamic
EMI	Electromagnetic Induction
ESD	Electrostatic-Discharge Sensitive Devices
FEM	Finite Element Method
FFM	Friction Force Microscope
FSRCA	Fiber-Steel Real Contact Area
IR	Infrared
LFT	Lubrication Film Thickness
MWCNT	Multi-Walled-Carbon-Nanotubes
OM	Optical Microscope
PEEK	Polyetheretherketone
PEEK-TC	PEEK Tribocompound
PoR	Plate-on-Ring
PPS	Polyphenylensulfide
RCA	Real Contact Area
RT	Room Temperature
SCF	Short Carbon Fibers
SEM	Scanning Electron Microscopy
SiC	Silicon Carbides
SiO_2	Silicium Dioxide
TEM	Transmission Electron Microscopes
TFL	Transfer Film Layer
TIM	Thermo-Imager Camera
TiO_2	Titanium-Dioxide
UHMWPE	Ultra-High-Molecular-Weight-Polyethylene
WLP	White Light Profilometer
XC-2N/A/P	Normal/Axial/Parallel Orientated Fibers for XC-2 Material

Variables

A	[1]	Aspect Ratio for Heat Flux Distribution
A_0	[mm²]	Ideal Contact Area
A_C	[mm²]	Asperity Contact Surface
A_n	[mm²]	Nominal Contact Area
A_r	[mm²]	Real Contact Area
a	[1]	General Variable
b	[1]	Y-Axis Intercept
c	[1]	General Variable
c_p	[J/gK]	Specific Thermal Capacity
d	[1]	Y-Axis Intercept
E	[GPa]	E-Modulus
F_f	[N]	Friction Force
F_n	[N]	Normal Force
F_s	[N]	Seizure Load
G	[V/m]	Electrical Field
HV	[1]	Vickers Hardness
H_0	[N/m²]	Materials Hardness
H_{min}	[mm]	Smallest LFT Height
I	[A]	Electrical Current
k	[W/mK]	Thermal Conductivity
L_0	[mm]	Ideal Specimen's Length
l_{Aa}	[mm]	Thermal Diffusion Distance Body A; T_a to T_0
l_{Af}	[mm]	Thermal Diffusion Distance Body A; T_f to T_a
l_{Ba}	[mm]	Thermal Diffusion Distance Body B; T_a to T_0
l_{Bf}	[mm]	Thermal Diffusion Distance Body B; T_f to T_a
l_{eff}	[mm]	Effective Contact Length of Contacting Bodies
m	[g]	(Specimen) Mass
p	[MPa]	normal pressure
p_0	[MPa]	Maximum Hertzian Pressure
q_{av}	[kgm²/s³]	Average Heat Flux
R	[ohm]	Electrical Resistance
Ra	[µm]	Average Surface Roughness
Rz	[µm]	Maximum Surface Roughness
r	[mm]	Radius of a Contacting Body / Counterbody
r_a	[mm]	Asperity Radius
r_{a0}	[mm]	Asperity Radius in Undeformed Shape

S	[s/m]	Electrical Conductivity
S_C^A	[µV/K]	Seebeck-coefficient Material A
S_C^{AL}	[µV/K]	Seebeck-coefficient Aluminium
S_C^B	[µV/K]	Seebeck-coefficient Material B
S_C^C	[µV/K]	Seebeck-coefficient Counterbody
S_C^P	[µV/K]	Seebeck-coefficient Polymer
S_c	[µV/K]	Seebeck-coefficient
s	[m]	Sliding Distance
T	[K]	Temperature
T_0	[°C]	Heat Sink Temperature
T_C	[°C]	Contact Temperature
T_C^A	[°C]	Contact Temperature Material A
T_C^B	[°C]	Contact Temperature Material B
T_C^C	[°C]	Counterbody Contact Temperature
T_{CbB}	[°C]	Counterbody Bulk Temperature
T_R	[°C]	Heat Sink (Reference / Heat Sink) Tempreature
T_a	[°C]	Average Surface Temperature
T_a'	[°C]	Modified Average Surface Temperature
T_b	[°C]	Bulk Temperature
T_f	[°C]	Flash Temperature
T_f^A	[°C]	Flash Temperature Body A
T_f^A	[°C]	Flash Temperature Body B
t	[h]	Time
U	[V]	Electrical Potential
u_h	[m/s]	Hydrodynamic Operative Velocity
v	[m/s]	Sliding Velocity
v_A	[m/s]	Sliding Velocity Body A
v_B	[m/s]	Sliding Velocity Body B
v_P	[1]	Poisson Ratio
W_l	[mm/h]	Linear Wear Rate
W_s	[mm³/Nm]	Specific Wear rate
w	[mm]	Width of (Line) Contact
x	[1]	General Variable
z	[mm]	Lubrication Film Thickness

Greek Symbols

ν_P	[1]	Poisson Ratio
ε_F	[eV]	Fermi Energy
η_{dyn}	[mPa/s]	Dynamic Viscosity
ρ_{hA}	[mm]	Bend of Contact Surface Body A
ρ_{hB}	[mm]	Bend of Contact Surface Body B
ρ_{el}	[ohm*m]	Specific electrical resistance
ρ_s	[g/cm³]	Specimen Density
α	[1]	Pressure-Viscosity Coefficient
β	[1]	Heat Distribution Correction Factor
λ	[1]	Lubrication Regime Coefficient
μ	[1]	Friction Coefficient
ρ	[g/cm³]	Density

1. Introduction

In the world of tribology, tremendous progress was achieved over the past decades regarding the improvement of polymer compound compositions. Reduced weight, self-lubricating characteristics and good wear resistance in combination with low friction coefficients lead to a substitution of metals by polymer compounds in various applications, e.g. sliding bearings. A key factor in this development is the possibility to produce customized (tailor-made) composites for specific demands by using special filler compositions. Nowadays not only macro-sized fillers like graphite, carbon or glass fibers are commonly used, but also fillers with dimensions in the size of only a few nanometers, e.g. carbon nanotubes (CNT). However, it is difficult to obtain a profound understanding of the sliding mechanisms resulting from different filler combinations for example, and knowledge of system characteristics within a sliding process is often lacking.

While the influence of material compositions and the use of fillers on tribological behavior have been widely investigated on a macroscopic level, in-situ determination of mechanisms and sliding system characteristics on a microscopic scale during a sliding process is complicated. However, for further and groundbreaking improvements of tribologically optimized polymer compounds this information is necessary to understand the effects, which nanofillers for example exert on frictional processes on a microscopic level. In order to obtain a better understanding of these processes and the structure-property relationships within a sliding contact, enabling a further optimization of the tribo-system, it is absolutely necessary to develop new and advanced measurement technologies.

With regard to the sliding of metal on metal, there are already various enhanced measurement techniques which, however, need to be modified and adapted to meet the requirements of polymer tribology. Such a technology could provide access to frictional temperatures, the material transfer of the sliding partners as well as mechanical contact conditions with regard to a possible intermediate layer.

2. State of the Art

A fundamental understanding of the tribological system and its characteristics is necessary in order to identify parameters to elaborate advanced measurement techniques to measure these parameters. The state-of-the-art in respects to tribology of polymer composites and advanced measuring techniques will be reviewed in this chapter.

2.1. Tribology

According to DIN 50 323 “Tribology” is defined as the science and technology of mutual acting surfaces in relative movement [1]. This expression, including friction, wear and lubrication was first introduced in England 1966 [2] in the course of the “Jost report”. The report disclosed the immense waste of resources, which were spent every year in order to maintain and replace tribologically stressed parts [3]. In regard to the surfaces in relative movements, the complexity of interactions and conditions cannot be described by a single natural or applied science. Therefore, it is handled by interdisciplinary work of engineers, physicists, chemists and other scientists [2]. The science of macroscopic tribological problems goes back to ancient times. While our ancestors 3500 BC already had to deal with the reduction of friction when they invented the wheels [4], tribology nowadays reached completely different dimensions regarding scale and depth of possible material modifications and analytics. Especially the progress of materials development and characterization of micro- and nanotribology which developed in recent years must be considered as a milestone and is often described as “the renaissance of friction” [5, 6]. When two objects move in a relative motion to each other under a normal force, which may result from a weight or any other force, an energy conversion takes place as a consequence of the interactions of the contact surfaces. The “energy loss” is defined as friction and appears as the product of antipodal force (F_f) and the sliding distance. Reasons for friction are complex. Adhesion and wear effects, influenced by surface characteristics are causative for friction [7]. Regarding commonly applied tribological investigations, a nondimensional factor called friction coefficient or coefficient of friction (CoF) μ is introduced. It is the ratio of frictional force F_f to normal force F_n [8]. This relationship is also well known as Coulombs frictional law [9].

Eq. 1: $$\mu = \frac{F_f}{F_n}$$ [8]

2.1.1. Area of Real Contact

The real contact area (RCA), which is mainly provided by asperities in contact, is of interest for tribological investigations and was already found by ancient researchers like Coulomb [10]. An illustration is given in Figure 1 A) in case of a cylinder contacting a harder and flat surface. Figure 1 B) shows other contact deformation possibilities in case of similar Young's modulus for both bodies in contact or higher modulus for the cylinder in comparison to the flat surface. Depending on the surface topography and properties the RCA can be much smaller than the nominal contact area which is determined directly by macroscopic geometrical aspects as well as by the contact area calculated according to Hertzian contact theory. When microscopic surface characteristics are taken into account the RCA can also be even larger than the nominal contact area, which is calculated on macroscopic scale (compare Figure 1 C)). In this case, the pressure leads to an elastic (or also plastic) deformation of one contact partner and the surface roughness of the other contact partner is filled up. However this case was not found in literature regarding tribological (sliding) exposure. For such dense contact situations the mechanical interlocking between both contact partners can be too strong for any direct sliding without severe damage.

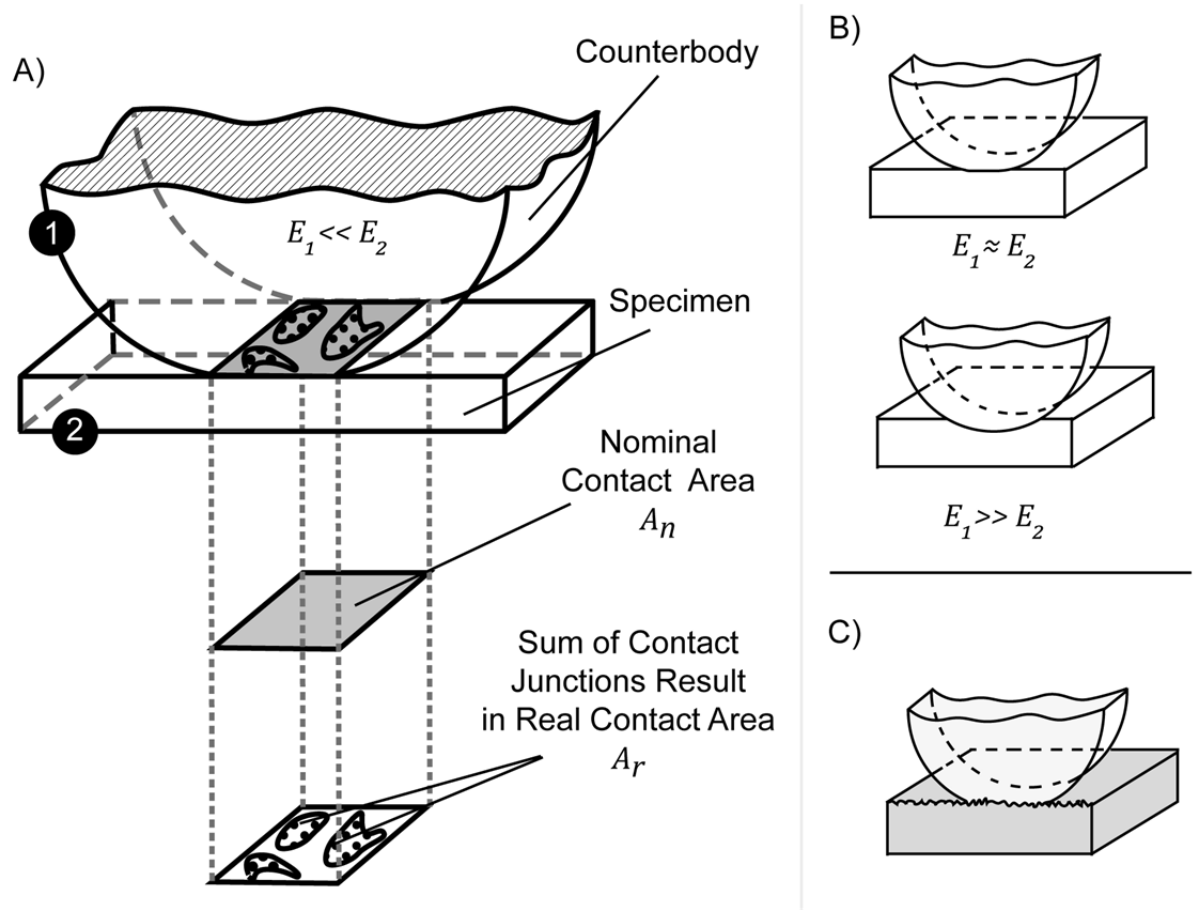

Figure 1: Nominal contact area vs. RCA; Part A) is based on [11]

According to Hertz, the nominal contact area A_n can be calculated for point contacts as well as for line contacts. The following equation exhibits a useful approximation for non-infinite cylinders in contact as well. Convex and concave surfaces can be calculated using a correct prefix while a flat surface for one of both contact partners A and B can be considered, if their bend $\rho_{hA/B}$, which is the reciprocal of the radius r, is set to 0. Other necessary variables are the Young's modulus E and the Poisson ratio v_P as well as F_n and the effective contact length l_{eff} [12].

Eq. 2: $$A_n = l_{eff} * 2 * \sqrt{\frac{8F_n(1-v^2)}{l_{eff} * \pi * E(\rho_{hA} + \rho_{hB})}}$$ [12]

The maximum pressure p_0 within the nominal contact area A_n for a line contact can be calculated using the following equation [12]. For such line contact, normal stress shows elliptical distribution over contact width:

Eq. 3: $$p_0 = \frac{4F}{\pi * A_n}$$ [12]

The RCA A_r is one of the key factors in order to determine friction and wear. It exerts important influences on the adhesion effects and plastic deformations of the sliding pairs [13]. The correlation between RCA, local pressures, elastic and plastic contact in relation to the CoF is illustrated in Figure 2. In contrast to plastic contact, elastic deformations will not remain after a sliding contact on materials surface.

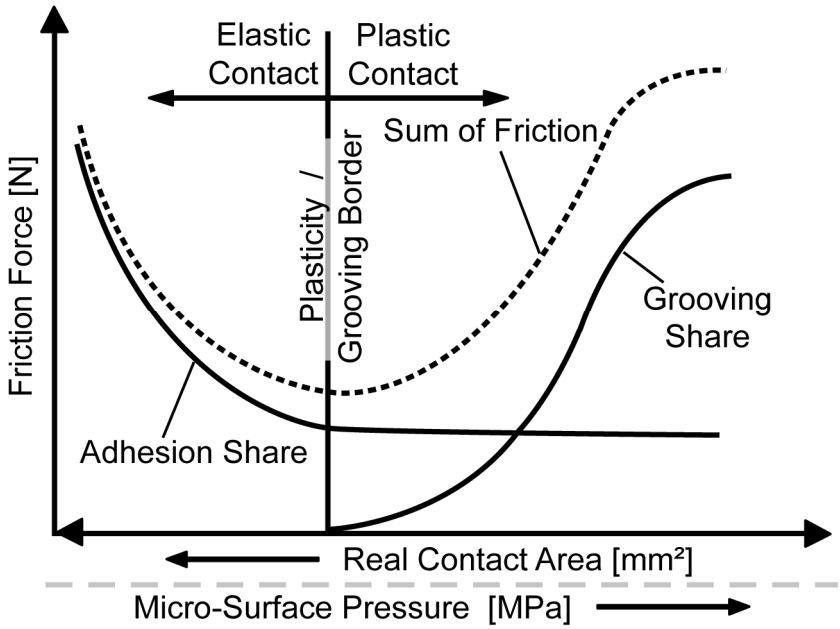

Figure 2: Adhesion and deformation depending on contact area [13]

The importance of the RCA is obvious as seen in Figure 2. It shows the correlation between adhesion and crenation with influence on CoF as a function of lowering

RCA and therefore increasing micro-surface pressure. The lowest CoF can be obtained for the highest local pressures in combination with the smallest real contact area for which no additional plastic grooving takes place. For larger RCA or micro-surface pressure exceeding elastic limit, an increasing CoF is evident due to more adhesion forces or plastic deformations of the contact asperities. According to Bowden and Tabor , the friction force resulting from micro-junctions shear-strengths τ_s is linear to the RCA [14]:

Eq. 4: $$F_f = A_r * \tau_s$$ [14]

Bowden and Tabor, Archard et al. as well as Ashby et al. executed out basic investigations on the RCA versus nominal contact area already back in the early last century [15–17]. New studies in regard to this contact issue are still performed indicating its importance [19, 20, 18]. Especially for anisotropic materials like polymer compounds the determination of the RCA is a challenge but important to e.g. obtain input data for simulations [21]. Bowden and Tabor also performed basic investigations on the behavior and determination of the RCA relating to stationary and moving surfaces in contact using the Hertzian equations and electrical conductivity measurement for their experimental part [16]. They found that the real contact surface is mainly dependent on the pressure and is hardly affected by size, shape and roughness of the surfaces [16]. Sliding surfaces were also investigated using this technique and it was pointed out that the size of the RCA changes rapidly during sliding situation and shows correlations towards friction and temperature changes [16]. Archard's model enhances Bowden and Tabor's claim. Based on the Hertzian theory for single ball-shape asperity contacts, the RCA is proportional to normal force [22]:

Eq. 5: $$A_r = C * F_n^{\,2/3} \quad with\ C = Material\ Constants$$ [22]

It is assumed that a higher normal load F_n leads to deformations of ball-shaped asperity contacts and new, additional contacts A_r occur [22]. There is an approach by Ashby et al., assuming that for a specific normal load, called seizure load F_s, all asperities are leveled and A_r becomes equal to A_n [17]. For the calculation, the material's hardness H_0 is taken into account while nominal load and contact area are set to aspect ratio with their real equivalent [17]:

Eq. 6: $$\frac{A_r}{A_n} = \frac{F}{F_s} \quad while \quad F_s = \frac{H_0 A_n}{\sqrt{1 + 12\mu^2}}$$ [17]

2.1.2. Kinematics

Friction is not only present in translational, one-dimensional sliding of two surfaces in contact. The same applies to other kinematics. The following types of two-body kinematics can be found [23, 24] in single and also combined versions:

a) Sliding: Translational movement towards the contact area with a sliding velocity of v.
b) Rolling and revolving: At least one of both contact partners offers a round shape with a rotation around its axis.
c) Drilling: Rotation of one contact partner vertical to contact area.
d) Banging / Bumping: Vertical translation towards the contact area with an intermittent contact.

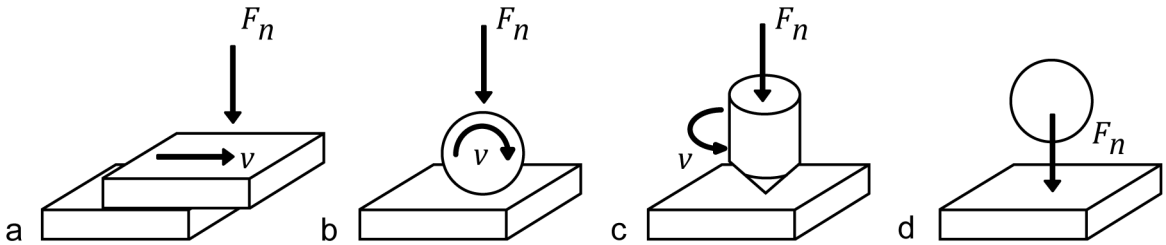

Figure 3: Contact kinematics; based on [23]

If any of these kinematics is applied on two bodies in direct contact, energy dissipation in the contact area will take place due to friction. This is caused by adhesion, hysteresis effects due to elastic deformation and wear mechanisms [25]. Wear is defined as “the progressive material loss from the surface of a solid body caused by mechanical reasons” [26]. According to the mentioned Jost Report (1966) there is a massive waste of resources because of the lacking knowledge regarding surface interaction phenomena. Although this report is not considering the consequences of wear, the waste added up to 515 million pound sterling for the United Kingdom. According to Rabinowicz, the waste could be avoided or reduced to a large extent if wear and the consequences of wear were better understood [27].

2.1.3. Wear Mechanisms

Different types of wear mechanisms lead to material loss in the wear process, depending on the material properties, the environmental conditions and the movement kinematics, which is directly related to the tribological exposure. Usually there is a combination of different wear mechanisms for a single wear process. The different wear mechanisms of different sliding systems are summarized in DIN 50 320 [26]. Wear mechanisms are described as follows [23, 28, 29]:

- Adhesion: Single asperities of both bodies in contact forming junctions on atomic scale. This is caused by the high local pressures on the individual asperities. The applied shear forces must break up the junctions at the adjacent area. At certain locations the adhesion can be stronger than the strength of the materials themselves and a break in the contact partners is possible. An offset of the sliding surface and material transfer happens.

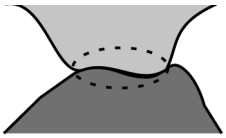

Adhesion
(e.g. Scuffing)

- Abrasion: In this case, the surface asperities of one of the contact bodies are more rigid than the counterbody or rigid particles are within the sliding contact. Abrasion occurs as scratching and chipping.

Abrasion
(e.g. Grooves)

- Surface disruption (fatigue): Micro contacts in the contact area are usually applied with periodic stresses caused by the normal- and shear-forces. Material exhaustion or fatigue around these contacts lead to cracks in the formations and finally to the separation of particles.

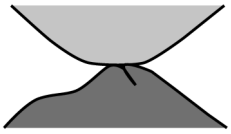

Surface Disruption
(e.g. Cracks)

- Tribochemical reactions: Chemical reactions between two bodies in contact can result in generating possible other substances within the contact area or the ambient medium as a consequence of thermal or mechanical activation due to frictional processes.

Tribochemical
Reactions
(e.g. Particles)

2.1.4. Wear Determination

For the purpose of materials developments and investigation of tribological systems, the occurring wear must be determined. According to DIN 50 321 [30] wear determination can be classified in two categories. As a first option a direct measurement of wear is possible. Usually, a volume loss or height loss is determined. A commonly used unit for wear designation is the specific wear rate W_s. This was first introduced by Archard [15] and is e.g. found in the ASM handbook for ASTM standards [31, 23]. The specific wear rate is defined as:

Eq. 7: $$W_s = \frac{W_V}{F_N * s}$$ [11]

W_V is the volume loss due to wear and s is the sliding distance. W_V can also be expressed using mass loss Δm and materials specific density ρ_s :

Eq. 8: $$W_V = \frac{\Delta m}{\rho_s}$$ [11]

Using this correlation, the specific wear rate W_s can also be expressed as:

Eq. 9: $$W_s = \frac{\Delta m}{F_N * \rho_s * s}$$ [11]

If the size of the wear surface is constant and all other parameters known, the time related linear depth wear rate can be converted to the specific wear rate and vice versa [23, 11]. Also, a time related wear measurement, i.e. online measurement, can be carried out. This means that a time, distance or output related wear rate can be measured. A simple option for time related wear is the linear depth wear rate W_l, which is based on the change of the specimen's length Δh per time t and defined as follows:

Eq. 10: $$W_l = \frac{\Delta h}{t}$$ [30]

2.1.5. Tribotechnical System

Friction and wear are two of the most considered parameters within a sliding contact. A tribological contact must be regarded as a complex system of many parameters and influences. The tribotechnical system consists of abundant input- and output-parameters, which determine the technical function of the system while external disturbance and energy loss are present.

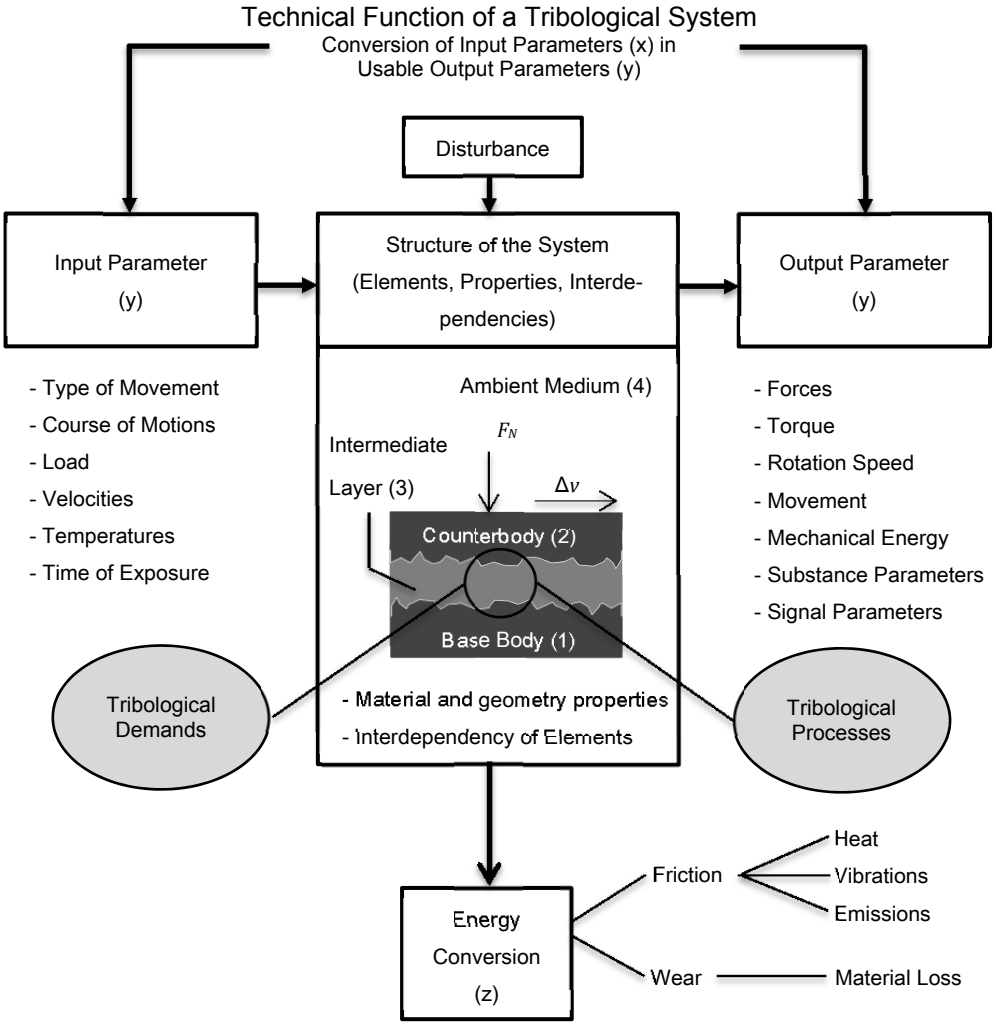

Figure 4: Tribotechnical System [23, 32]

The complexity of the entire tribotechnical system is evident as seen from Figure 4 although it provides a rough estimation of the relations between parameters in the system. Effective characterizations of frictional processes and a profound understanding of the tribology mechanisms are necessary for both, material developments and use in industrial applications.

Three different approaches of understanding and characterizing a tribological system were developed in the past:

- Analytical calculations: Attempts to interpret tribological issues with basic mathematics, sometimes supported by experimental results, were made to a great extent. For contact geometries, e.g. Hertz formulated equations, which are nowadays well known as the Hertzian pressure [33, 34]. Regarding tribology, a first wear model was proposed by Archard [15, 22]. This original model considered a couple of parameters like normal load, sliding velocity and wear volume. More than 100 models were established in follow-up studies leading to analytical approaches to tribology considering the influences of more parameters [34, 35]. It should be noted that the tribological system is complex to an extent in which usually analytical calculations are only possible with simplified models and/or boundary conditions.

- Finite element method (FEM) simulations: State of the art software and hardware allow the simulation of complex systems like tribological sliding contacts. However, the limiting factor for FEM simulations of isotropic materials can often be found in the performance of FEM software or hardware, as immense computing capacity is necessary when more complex systems have to be simulated. Most publications regarding FEM simulation for tribology are from the late 1990s onwards. Many of them cover basic relationships and aspects of sliding contact [36–38]. However, there are also very specific studies to analyze special systems like motion in artificial hip and knee replacements for predicting design requirements [39, 40]. Furthermore influences of nano-scaled layers were studied as well as more complex anisotropic materials like polymer compounds [41, 42].

- Experiments: According to DIN 50 322 [43] wear testing can be classified in six categories:

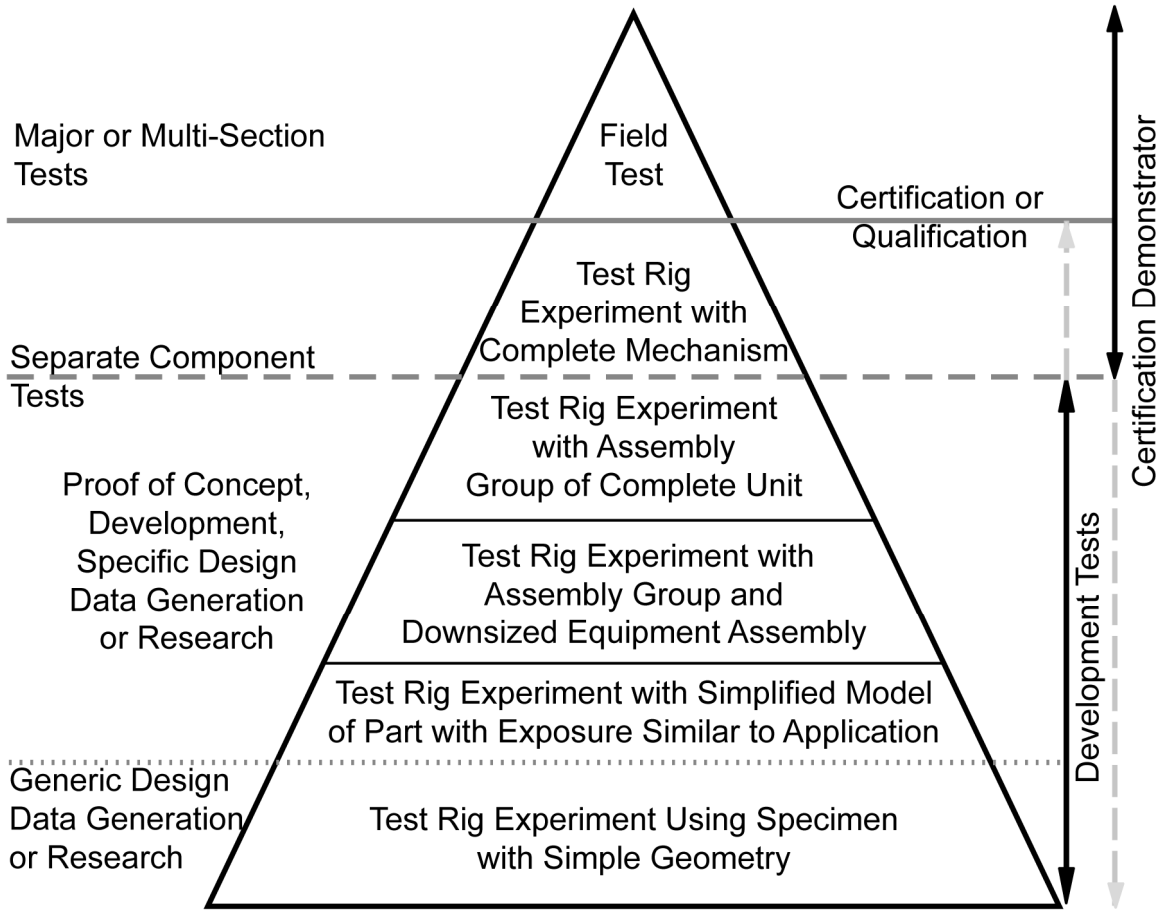

Figure 5: Master pyramid of tests; based on [44]

Investigations of material tribology mechanisms are usually applied on model test rigs, i.e. with a specimen of simple geometry. The simplified geometry is usually applied to a basic kinematic movement. Most used configurations of continuous sliding tests are pin-on disc and block/plate-on-ring configurations. The ASM as well as the DIN handbook are containing ASTM and DIN standards for tribological model testing. Many other test configurations are available from these standards, suitable for different purposes [31, 45].

2.1.6. Polymer Tribology

Polymers were subject of increased interest and profound developments within the recent 50 years, especially regarding their tribological properties [46]. Polymers usually can be divided into three categories; namely thermoplastics, thermosets and elastomers. All belong to the category of synthetically produced materials while their structure as well as their production varies considerably [47].

Polymers contain several intrinsic characteristics which are beneficial for tribological applications. According to Czichos et al. these are primarily low intermolecular bonding forces, high resistance against corrosion and high vibration damping factors [23].

In comparison to metals and ceramics, the lower density of polymers leads to a more weight-efficient, energy saving operation in applications [48, 27]. Another benefit is cost efficient processability [49]. Moreover, owing to their self-lubrication capability, polymeric tribo-materials can operate under lubricant-free conditions, i.e. without the requirement for adding further lubricants such as oil or grease [46]. Especially in challenging environmental conditions such as vacuum or extreme temperatures, this can be an important factor [49]. Polymers also have some disadvantages, which inhibit the usage of pure bulk material for many, mostly unlubricated sliding applications [46]. These disadvantages include the relatively low, strongly temperature dependent Young's-modulus as well as the comparable low stiffness and heat transfer rate [23]. The sliding characteristics of a neat polymer against steel are related to the loading conditions and the surface characteristics of the steel counterbody, such as surface roughness. For sliding combinations of polymer against polymer the friction depends mainly on the adhesion activity which can be determined by the surface energy of the single polymers [50, 23].

Probably the biggest advantage of using polymers for tribological applications is the possibility to apply functional fillers. Such a polymer compound is a combination of the pristine polymer with at least one type of macro, micro or even nano sized particles or fibers. Fillers can exert various influences on the compound and its tribological properties. They enable an improvement of mechanical characteristics, e.g. Young's modulus and/or an increase of impact resistance. An intrinsic electrical conductivity can be realized as well and solid lubricants in order to lower the friction during tribological tests can also be incorporated [51, 47].

Using the advantages of fillers, a customized sliding material can be engineered, meeting the demands of a specific application. Extensive studies on fillers and their influence on tribological properties with reference to nano-sized fillers were carried out by Friedrich et al. [46]. A few examples of possible fillers and their effects, which are related to this work, are given below:

- Short carbon fibers (SCF), for instance, have a history of being effective fillers enhancing mechanical properties of polymers. Therefore they are frequently used as reinforcing fillers. SCF usually improve the modulus of a polymer matrix significantly. Depending on matrix materials, aspect ratio of SCF and matrix/SCF interfacial bonding, SCF often enhance the compression and tensile strength, fracture toughness etc. [52–57]. Another aspect is the thermal and electrical conductivity, which can be obtained by using short or continuous carbon fibers [58, 59]. To increase the electrical conductivity a sufficient

amount of fillers is necessary in order to achieve the percolation threshold [60].There is a number of possible new applications for a CF filled polymer with an intrinsic electrical conductivity, e.g. in electrostatic critical environments or for the use of Electrostatic-Discharge Sensitive Devices (ESD) [61]. A further rise of electrical conductivity or other material characteristics can be achieved by combinations with multiple fillers.

When a CF filled polymer is sliding against a metallic counterbody, the CF take most of the loads applied to the polymer composite. Thereby, it reduces the adhesion between the sliding pairs, resulting from reduced RCA. Many publications reported a great enhancement in the wear resistance of the polymer matrix by incorporating CF. It enhanced the mechanical properties, reduced adhesion and abrasion and transferred a lubricating carbon film (pulverized CF) to the counterface. Additionally, improved thermal conductivity was reported in [62–67]. Special attention to the carbon fiber orientation in the sliding contact, as it influences the friction and wear behavior, was given by Friedrich and Zhang et al. et al. [68, 69].

- Solid lubricants, such as graphite, polytetrafluorethylene (PTFE) and metal dichalcogenide, e.g. molybdene disulfide (MoS_2) and wolfram disulfide (WS_2), usually have an inter-lamellar structure which facilitates the shear when the sliding direction is parallel to the planes of the material. The sheared layers of the solid lubricants can transfer onto the counterface, thereby promoting the formation of a lubricating transfer film. It was demonstrated that solid lubricants can reduce the friction and wear of a polymer composite [70, 71].

- The huge surface area of nanoparticles is one of their most attractive characteristics because it facilitates large area of interphase in a composite and thereby a strong interaction between the fillers and the matrix even at a relatively low nano-filler loading [19]. Besides the significant results in the enhancements of mechanical properties, such as modulus, strength, fracture toughness [72–75], the use of nanoparticles can result in improvements of the tribological behavior of the polymer compound. Wang et al. [76, 77] demonstrated enhanced tribological performance of polyetheretherketone (PEEK) by reinforcing it with nano-sized silicon-carbides (SiC). Wetzel and Zhang et al.[78, 79] revealed that the addition of mechanically dispersed nanoparticles into epoxy resin improves the tribological performance of the polymer compound. Zhang et al. [67, 80] found that nano-sized silicium-dioxide (SiO_2) im-

proved the tribological performance of PEEK. Bahadur and Sunkara [81] reported that low-loading titanium-dioxide (TiO_2) and copper-oxide (CuO) nanoparticles improved the tribological behavior of polyphenylene sulfide. This improved tribological performance of the polymer matrix by adding nanoparticles was ascribed to the enhanced mechanical and fracture properties of the polymer and/or the formation of a homogeneous transfer film. Electrically conductive nanofillers, such as CNT, can lead to a significant electrical conductivity, reaching the percolation threshold at low filler content. Pegel et al. showed, that for multi-walled-carbon-nanotubes (MWCNT) filled polycarbonate the percolation threshold was already achieved at 0.5 wt. % [82]. For bimodal systems containing SCF and MWCNT, Noll et al. revealed synergetic effects between the nano- and micro-sized fillers especially regarding electrical conductivity [83].

The processing procedures of polymer compounds are different for thermosets and thermoplastic materials. This is caused by the differences in their molecular structure. Thermoplastics consist of unconnected molecular chains which can achieve a higher flexibility by applying heat. Thermosets have strongly connected molecular chains, which, if broken up by heat, cause the failure and degradation of the material [84, 47]. The differences in molecular structures of thermoplastic and thermosetting materials also result in significant differences with regard to mechanical, chemical and tribological properties.

During the manufacturing process of a polymer compound at least two steps have to be completed. The matrix materials are usually provided as a resin in combination with a hardening agent for thermosets and as a granulate for thermoplastics [11]. The first step is an incorporation of the fillers. Commonly used mixing and dispersion methods are e.g. the use of a dissolver for thermosets and single- or multiple-screw extruders for thermoplastics. To achieve a good dispersion and distribution for nano-scaled fillers is complex, as many nano-particles are exhibiting strong agglomeration tendencies due to their high surface energy [85]. In regard of dispersion of nanoparticles, commonly used processes are in-situ synthesis, in-situ polymerization and mechanical dispersion.

In a second step, the obtained compounds can be processed in various ways. A convenient way for thermoplastics is a combination of compounding and extrusion. With this method, continuous profiles or foils can be manufactured as well as coated wires. The compounding can take place in the same step as the shaping. Blow molding e.g. for bottles can also be performed with this technology [86]. Other processes,

to name a few, are resin-transfer-molding, laminating, spray-coating, pultrusion, hot-pressing and of course molding for an easy processing [86, 87].

2.1.7. Transfer Film Layer

In a dry sliding contact, a transfer film layer (TFL) can build up between two solid bodies as mentioned before. The build-up process of a TFL is a time-related procedure and does not happen immediately [88]. A more detailed view of the contact between the two solid bodies with the TFL is given in Figure 6 in case of an isotropic counterbody for a polymer compound base body. Although TFL also exist in metal-metal combinations, caused by adhesion and tribochemical effects [23], only transfer films of polymer materials sliding against steel counterbodies will be reviewed here as they are directly related to this work.

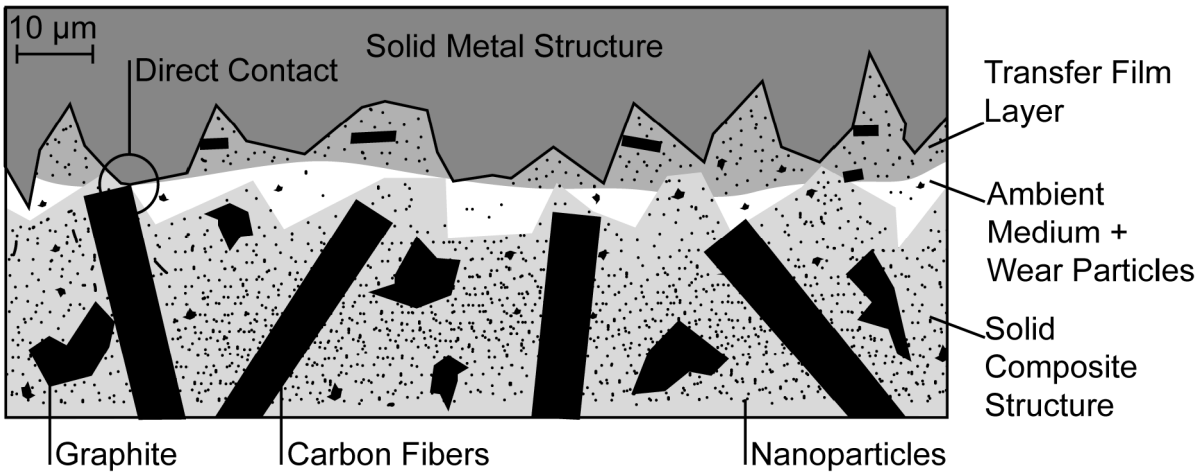

Figure 6: Close-up of tribological contact in dry sliding

A TFL usually lowers the direct RCA between the sliding bodies while covering parts of the steel surface and takes some of the load applied to the sliding contact. The overall contact, combined with TFL, can increase. Numerous researchers demonstrated that TFL exerts a strong influence on friction and wear properties [81, 89, 90]. E.g. recent investigations by Chang et al. [100] showed direct correlations between via nanoindentation measured TFL thickness and frictional characteristics of the system. Based on this data it was possible to propose a “transfer film efficiency factor”, taking into account the average TFL thickness in relation to the surface roughness while giving direct correlations to friction and wear characteristics. It is commonly believed that a TFL is protecting the soft polymer from the abrasions of the steel asperities by filling up the crevices of the steel counterbody. This also decreases the CoF as most polymers have self-lubricating effects, reduces the friction, while polymer bulk-material is sliding on polymeric TFL [91, 46]. The evolving of a TFL is mainly dependent on two mechanisms:

- Mechanical interlocking: Fragments of polymer which were produced e.g. via abrasion during sliding are locked into the crevices of the steel counterbody asperities. They remain in the crevices due to the adhesion to the steel counterbody or cohesion to other polymer fragments [46, 92–94].
- Adhesion of polymer on the steel counterbody: The wear mechanism of adhesion has already been described in 2.1.3. The mechanisms for adhesion contains van der Waals attraction forces, Coulomb electrostatic forces and tribochemical reactions [91, 95]. According to several studies the tribochemical reactions between TFL and steel counterbody can have an important influence on the adhering strength, which itself exerts significant effects on friction and wear properties. It was determined that the bonding strength of the TFL is closely correlated to the wear rate of polyphenylen sulfide [81, 92, 96].

The properties of a TFL and its development process can be influenced by various parameters. The intensive research on influencing parameters carried out in the past, emphasizes the importance of the TFL concerning sliding properties. The thickness and the structure of a TFL are of great interest regarding its characteristics. Concerning polyamide 46, a study was conducted on the molecular formation of the TFL [97]. It was shown that the molecules were aligned on the specimen's surface as well as in the TFL in sliding direction. Furthermore, it is interesting that an applied sliding changes the molecular structure of the polymer surface. The crystal state in the TFL layer decreased while the amorphous state increased. This indicates a change in structure from the original polymer to the TFL-polymer [97]. The thickness of a TFL is related to the sliding-time. The thickness of a "high-performance" TFL is usually reported to be in sub-micro scale, similar to the surface roughness of the steel counterbody [67, 98, 99]. Thick transfer films may even increase wear, as they are sometimes unstable and can be removed again in the frictional process [91, 100, 46]. An example of the morphology of the TFL of polyphenylensulfide (PPS) based materials was obtained from own previous studies [99] and is given in Figure 7. Illustration A) and B) show the optical microscope (OM) image and scanning electron microscopy (SEM) image of PPS filled with 3 wt.% CNT. This material had a high wear rate and exhibited a thick and inhomogeneous transfer film. The images C) and D) show a similar material with additional 10 wt.% SCF. The wear rate was lowered about 2 decades and a thin and homogeneous TFL was developed [99].

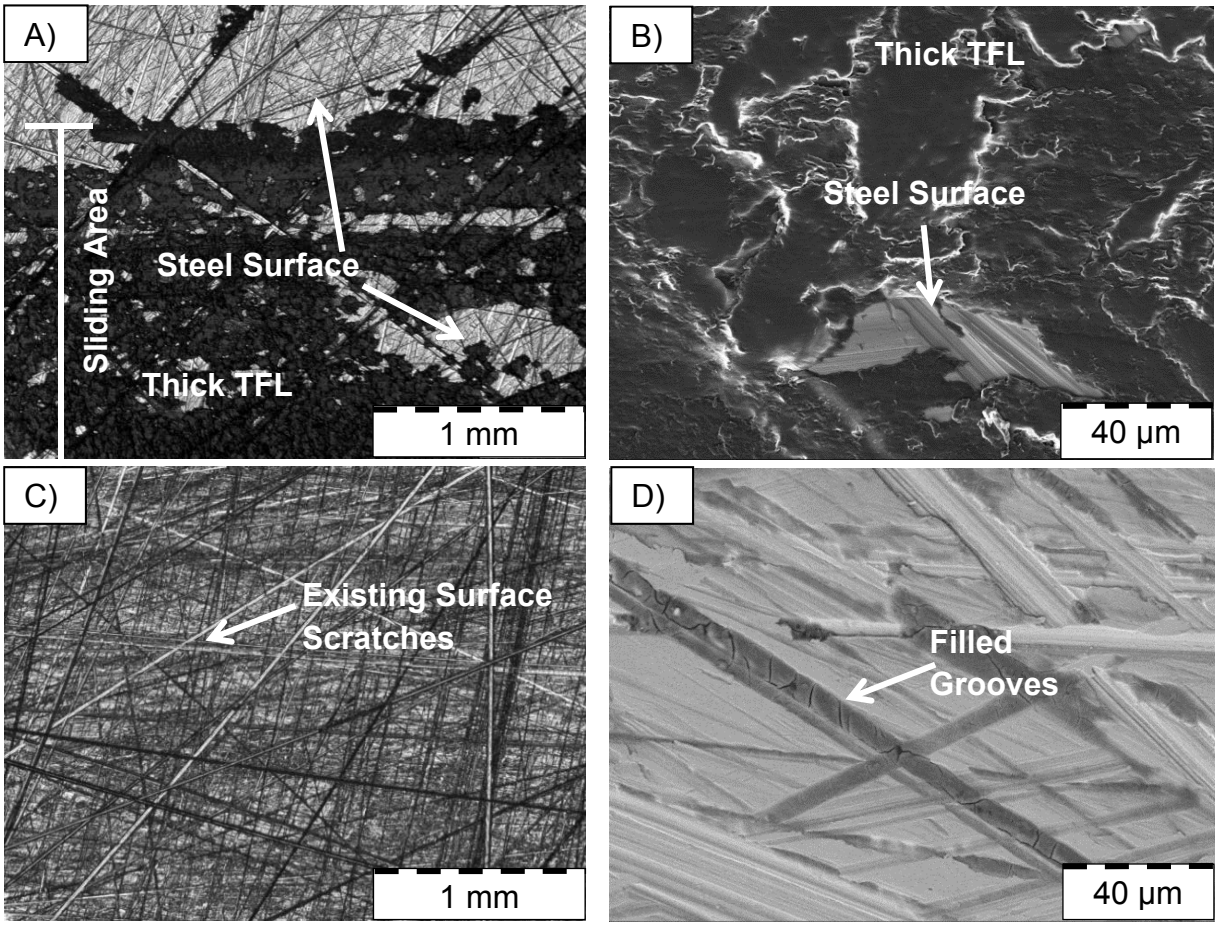

Figure 7: TFL top view OM and SEM observations on counterbody ring [99].

Regarding polymers filled with fibers, e.g. SCF, it was reported that the wear particles of the fibers can remain in the TFL [62]. In case of Kevlar fiber reinforced PPS, Yu and Yang claimed that the TFL, formed by the PPS/Kevlar composite, is thin and uniform while a relatively thick TFL is formed for neat PPS [90]. Similar results were found for combinations with CNT by Noll and in earlier, own studies [83, 99]. Yu and Yang claim that the increased frictional heating due to a smaller contact area, which is caused by reinforcing fibers, leads to a higher decomposition and oxidation of the polymer matrix. This increases the bonding strength of the TFL to the counterface. After the formation of a TFL, the wear rate is lowered by mechanisms mentioned before [90].

For fillers which can act as a solid lubricant, the basic mechanism was already explained. The transferred solid lubricant on the steel counterbody can provide a stabilizing function on the friction and wear and thus lead to a coherent transfer film [70, 71]. Regarding nano-sized fillers, various investigations were accomplished. Many of them were carried out or summarized by Bahadur et al. and Friedrich et al. [69, 91, 92]. The effects, which nanofillers exert on TFL, are based on several mechanisms. The first is the reduced adhesion of TFL on the polymeric specimen which can result

in a lower CoF. Furthermore, the mechanical interlocking is enhanced by the use of nanoparticles. The bonding strength of the TFL on the steel counterbody is improved due to chemical reactions. Another aspect is a possible rolling of nanoparticles within the sliding interface which can also improve tribological performance [46, 101, 92]. It is also possible to combine several types of fillers. Their effects on the TFL vary, what can emerge as positive as well as negative synergetic effects. The study of the related mechanisms becomes more difficult with increasing number of different fillers interacting within one polymer compound. In this regard, it is not surprising that most studies only investigate mono- or bimodal systems.

Concerning the formation of a transfer film, the temperature is a key factor. It was reported by Yang et al. that for PTFE sliding against steel the material transfer rate of PTFE raised with increasing system temperature [102]. Specific investigations of contact temperatures, supported by FEM simulations were done by Váradi et al. [103]. They showed that the contact temperatures of PEEK during sliding are expected to be near to the melting temperature of the matrix material. These temperatures are strongly influenced by the formation of a TFL as it distributes the stress, introduced by the normal load, to a larger area resulting in a lower local pressure.

The structure and material properties of the used counterbody have an influence on the TFL as well. Ramachandra and Ovaert [104] investigated PEEK polymers on a pin-on-disc configuration for sliding against different scribed steel disks. Different morphologies of transfer film occurred on various scribed steel surfaces. Similar observations were made by Marcus et al. for a reciprocating sliding of ultra-high-molecular-weight-polyethylene (UHMWPE) against parallel and perpendicular ground steel counterbodies [105]. Besides fillers, parameters such as system temperatures, counterbody topography and properties, sliding velocity, normal load and sliding distance as well as ambient atmosphere have a significant influence on the formation and structure of a TFL as well [46, 91].

If a lubricant or any other ambient medium is used, the influence of a TFL becomes less important. Regarding carbon fiber reinforced polymer composites, Jia et al. showed that the tribological behavior is dominated by cooling and lubrication effects of the water medium used [106]. However, even under oil lubricated sliding conditions, Scherge et al. proved that material transfer on a comparably small scale happens and a TFL is building up. They also demonstrated that under boundary lubrication conditions the surface roughness of the counterbody influences the formation of TFL and CoF [107].

The description of polymer compound material characteristics is complex due to its often anisotropic characteristics. Concerning a complete description of an object, additional aspects such as surface and shape characteristics must be taken into account. In particular if the material is a composite its characteristics must be considered in micro- or even nano-scales. There are plenty of other factors such as dispersion, filler-matrix coupling etc. which are often difficult to determine. A transfer film, which is built from a polymer compound material may contain transferred fillers, but not in their original shape. Due to the complexity of a sliding contact, numerical and simulative approaches can be difficult. Regarding simulation purposes, micro-scaled investigations were carried out for polymer compound in sliding contacts. Some of the investigations also took into account the existence of a TFL and the temperature of the contact areas [42, 103]. Furthermore, investigations of individual aspects, supported by FEM analyses, can be found in the literature, e.g. for contact properties of a transfer film layer between a composite and steel counterbody [108]. Eiss et al. set up a basic analytical model for a pure polymer. This enabled a prediction of the material transfer of low-density-polyethylene, polyvinylchloride and polychlortrifluorethylene, without the need to obtain experimental data [109]. However, the value of uncertainty quantifying the TFL was within a factor of five. This indicates the complexity of the sliding contact of even the pure polymer. The understanding of the functionality of a TFL is also still lacking in some parts. Further investigations, especially with the possibility of on-line observation of the TFL development, are necessary.

2.1.8. Lubricated Sliding

In order to minimize friction and wear, the application of lubricants is common practice. In this chapter a close look at fluid lubricants will be taken. When fluid lubricants are mentioned, usually mineral lubricants or synthetic lubricants come in mind. They are subdivided in paraffinic, naphthenic and aromatic oils concerning mineral lubricants and concerning synthetic lubricants, they are divided in polyalphaolefins, polyglycols, ester oils and silicones [110]. Many other substances may also act as lubricant. In biological applications such as knee or hip joints, lubrication takes place based on biological substances [111]. Even water or sea water is often used to reduce friction in some applications, e.g. in water pumps. Polymers are used in many tribology studies as they provide a high chemical stability and a high wear resistance as well [106, 112–114]. Friction under lubricated conditions can be divided into three main sections as shown in Figure 8. Various parameters have a strong effect on the behavior of the lubrication-system and the resulting sliding performance.

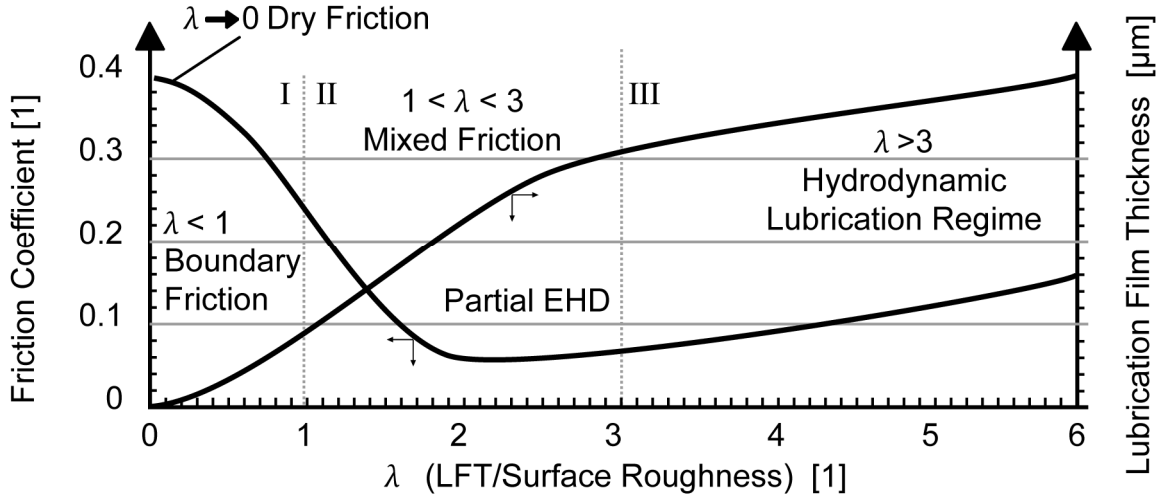

Figure 8: Lubrication regimes according to Stribeck [23, 115]

In Figure 8, the friction in relation to the lubrication regimes, according to Stribeck, is given as a function of the ratio of the LFT and the surface roughness [24, 116]. It is expressed as a lubrication regime coefficient λ. The system behavior of a lubricated sliding is primarily dependent on the contact properties of the ground body and the counterbody as well as the interaction of the lubrication film. Besides the surface roughness of the sliding partners, the LFT is a dominant parameter and is itself influenced by the dynamic viscosity η_{dyn} of the lubricant, the sliding velocity v as well as the normal pressure p [9, 115]. The influence of individual aspects varies depending on the lubrication regime. Nevertheless, different variations of Stribeck curves can be found in literature; some as a function of LFT to surface roughness as shown above, but also as a (logarithmic) function of $\eta_{dyn} * v/p$ [117–119]. This function is basically a description of the influences on the LFT. In this regard, both functions are correlating with each other.

2.1.8.1. Hydrodynamic Lubrication

If a hydrodynamic lubrication takes place, the ground body and counterbody are completely separated and have no direct contact to each other. The friction properties of the system are dominated by pure fluid friction. In most cases frictional forces of a pure fluid friction are much lower than between two solids. Concerning our studies, the relatively thin hydrodynamic films are of interest only, which behave non-turbulent. This simplified model requires some preconditions such as relatively smooth surfaces and a high aspect ratio from the lubrication film thickness (LFT) to the surface dimensions [117]. Besides the contact surface and the velocity, the viscosity is the dominant influence parameter. The following equation is common to describe this viscous friction:

Eq. 11: $$\mu = \eta_{dyn} * A_n * \frac{v}{z}$$ [117]

Regarding an incompressible fluid, the lubrication film thickness z has a direct relationship to the normal force F_n, if the contact area A_n is constant. This leads to the following equation, which describes the behavior of a friction force in a hydrodynamic regime:

Eq. 12: $$F_f \sim \eta_{dyn} * \frac{v}{F_n}$$ [23]

The equations mentioned above are necessary for a basic understanding of the system behavior. Accurate calculations regarding physical conditions and lubrication film behavior can be performed using Navier-Stokes equations combined with the equation of continuity. The Reynolds equation allows further simplification by adding several basic presumptions [23, 120]. The numerical adaption of these equations requires knowledge about geometry of the contact, the external pressures and the conditions. This was accomplished for different sliding configurations and applications in the past [9, 120]. Although the issues of hydrodynamics can already be solved mathematically, simulations on this topic are made with additional focus on e.g. off-centric bearings [121]. Compared to dry sliding, the temperatures have a massive influence on the system. Viscosity of the lubricant depends on the temperature which itself is dependent on the frictional heat in the system [9]. Fluid rheology is an important field of research with regard to this topic, since the requirements of a lubricant within a difficult environment with changing conditions are high. Engine bearings are a good example. The range of possible sliding velocities combined with various load regimes is wide, but a lubrication film, neither too thin nor too thick, is desired. It would result in a possible damage or a waste of energy. In order to customize lubricants additives are commonly used. They are supposed to affect both, the hydrodynamic lubrication regime and the mixed and boundary lubrication which is usually present during start/stop phases, too [120].

2.1.8.2. Boundary Lubrication

The opposite of a hydrodynamic regime can be expected in boundary lubrication. Concerning hydrodynamic sliding, both sliding bodies are completely separated by the lubricant, while in boundary sliding conditions, the partners are in almost direct contact, only separated by a few monolayers of the lubricant, still providing a lubrication effect and considerably lowering frictional forces [9]. A combined sketch of boundary and mixed lubrication is given in Figure 9.

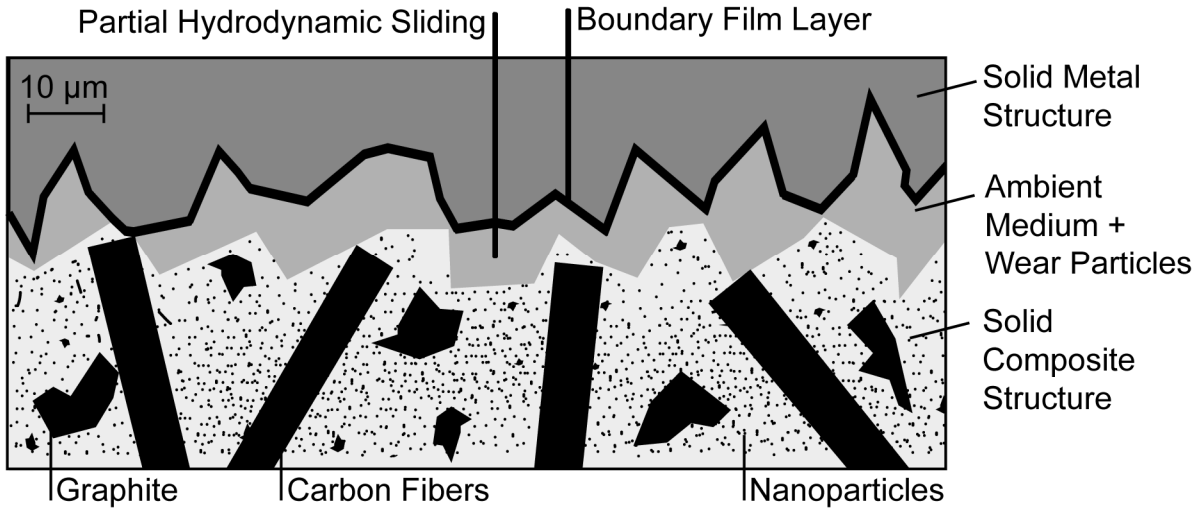

Figure 9: Boundary and mixed lubrication

Although the hydrodynamic sliding properties are well understood, boundary lubrication of polymer materials is very complex and a profound understanding of the frictional processes is still lacking. As this is the wear-dominant regime for applications with a start/stop functionality, there is numerous ongoing research dealing with the complexity of the contact problem, covering many scientific fields such as materials science, chemistry, contact mechanics, etc. [9, 120]. The viscosity of the lubricant, which is one of the dominating influential parameters in hydrodynamic sliding, does not play an important role in boundary sliding friction. The molecular interdependency of the surfaces with the lubricant as well as the surface characteristics of the sliding partners are of much greater importance [9, 23]. Conditions of high local pressures may occur, which can lead to nucleation of the lubricant. This results in a solid-like behavior of the lubricant and must be taken into account when describing single asperity contacts with high local pressures under boundary lubrications [9, 122]. A basic model, which describes the tendencies concerning a variation of a normal load, a velocity or a system temperature for boundary friction could not be found in literature. With regard to Figure 8, mixed lubrication can be prevented by higher normal load, lower sliding speed or lower lubricant viscosity. Besides their influences on the CoF these parameters can also exert an influence on the system temperature. As mentioned before, in many applications the Stribeck curve is given as a function of $\eta_{dyn} * v/p$. In some publications in boundary lubrication regimes the CoF is expected to be on a stable level [9, 117, 120]. Others expect a rise in the CoF within boundary lubrication regime under e.g. increasing sliding speed as the aspect ratio of LFT to surface roughness decreases [23]. It should be noted that these publications were mainly addressing metals rather than polymers as sliding materials. This discrepancy demonstrates the need of a fundamental research on and better understanding of this topic. Regarding boundary sliding conditions, several approaches were taken

using simulation techniques with special regard to the squeeze-out of the lubricant. It was found that for molecular thin films the continuum theory is not valid [9, 123–125].

2.1.8.3. Mixed Lubrication

A mixed lubrication is situated in-between the hydrodynamic and boundary lubrication regimes. As indicated in Figure 9, some regions are in direct contact and only separated by a boundary layer. Other regions are filled up with lubricant, which carries some of the load. The average LFT of a mixed lubrication is the most important parameter as it is essential for the number of asperity contacts and thus for local contact pressures and temperature rises due to frictional heat of the colliding asperities [126]. A change of the LFT, which itself is in correlation with $\eta_{dyn} * v/p$, is accompanied by a rapid change in frictional force as indicated in the Stribeck-curve. Since both hydrodynamic and boundary lubrications are present in a mixed lubrication, an understanding of the system by the means of numerical, simulative or experimental approaches is difficult. The tribology mechanisms related to each lubrication regime and the new, additional aspects arising of their combination must be considered at the same time. Due to its intrinsic complexity, mixed lubrication is still not well understood [127]. Numerical and simulative approaches were done as the importance of this lubrication regime is fundamental for life time enhancement for many applications [127, 128]. Especially the work of Hu and Zhu [129–131] should be considered since their pioneering simulation approaches concerning mixed lubrication was fundamental for other studies [126, 128, 132].

2.1.8.4. Elastohydrodynamic Lubrication

Concerning hydrodynamic lubrication, the sliding partners can mostly be seen as rigid solids. However, for elastohydrodynamic (EHD) lubrication, the elastic material behavior of the materials has to be taken into account as well as the pressure dependent viscosity of the lubricant. The larger surface area which is provided by local elastic deformations together with the pressure related lubricant viscosity separate the surfaces [9]. A typical solution for the LFT and pressure within sliding contact is given in Figure 10. Relating to thermo-EHD lubrication, the additional mechanism is the influence on the viscosity of the lubricant caused by thermo- and piezo-viscous effects resulting from frictional heating and a high local pressures during the contact [9, 133, 134]. The necessary knowledge for analytical description was mostly obtained by the studies of Hertz [33]. Based on this, Ertel coupled the differential equations in relation to energy dissipations, hydrodynamics and elastic deformations [134]. This work was subsequently enhanced by Dowson and Higginson and is still

being used as a basis for various mathematical and simulative investigations [23, 135]. EHD calculations can be found e.g. in standardized lifetime calculations for roller bearings while newer studies also take a closer look at micro-hydrodynamics with respect to the real surface topographies. This research field still has much room for improvement in order to obtain a higher sliding performance by e.g. surface modifications [23, 132, 136].

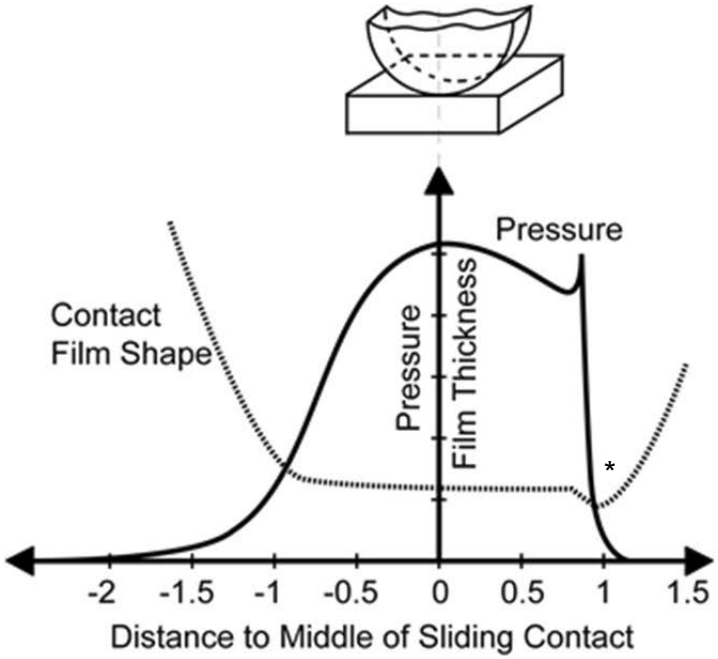

Figure 10:Typical solution for pressure and film thickness in an EHL line contact [137, 138]

As seen from Figure 10 the distribution of pressure within a deformed line contact of e.g. a cylinder on a plate behaves contrary to the contact lubrication film shape. While contact film shape does not deform in middle of contact area anymore, because elastic deformation limit of the contact partner is reached, pressure still increases up to middle of contact area. The calculation of the LFT for line contacts in EHD on their smallest height H_{min} near the exit area ("*" in Figure 10) is possible according to the equation of Mohrenstein-Ertel which was modified by Dowson and Higginson [139–141]. Their equation was again revised by Dawson himself in 1968 [141, 142]. The equation is ruled by three dimensionless parameters, namely the material characteristics G, velocity U and load parameter W.

Eq. 13: $$H_{min} = 2{,}65 \times \frac{G^{0,54} \times U^{0,7}}{W^{0,13}}$$ [142, 143]

with: $$U = \frac{\eta_{dyn} \times (\frac{u_h}{2})}{E \times r} \qquad W = \frac{a}{E \times r} \qquad G = \alpha \times E$$ [141, 142]

The normal load F_n on the contact with w is described by the variable a. Also, the Young's modulus E and radius of counterbody r are taken into account. Additionally, the pressure-viscosity coefficient α of the fluid is used as well as its dynamic viscosity η_{dyn}. The hydrodynamic operative velocity is given by u_h.

2.1.9. Temperatures

Some influences of the temperature on the tribological sliding behaviors were mentioned before. As a majority of the energy, which is transferred by friction, is converted to heat, a profound knowledge of its influence on the sliding characteristic is necessary [144]. In this section, different types of temperatures and their origins within a sliding contact are analyzed more closely.

According to Kennedy, the temperatures can be divided into three categories [145]. Besides the so-called flash temperatures T_f, an average surface temperature $T_a$and the materials bulk (volume) temperate T_b can be defined. The highest temperatures are the flash temperatures, which occur on very small surface asperities in micro-scale dimensions. Such asperities are dependent on the surface roughness and relevant for the RCA [145]. Those flash temperatures can occur parallel on several asperities at the same time and sequentially on the same asperity as well. Although the asperity radius is in micro-scale and the lapses of time for heating are microseconds, temperatures can reach high levels exceeding 1000 °C. The integration of the temperature distribution over the whole sliding surface is defined as average contact temperature T_a. This surface temperature exerts a surface heat flux on the bulk material [145]. Usually the material must be fixed in e.g. a holder, which itself has a certain temperature and heat transfer capability. In most cases, the sliding contact is embedded in a surrounding medium. Regarding these external influences, the bulk temperature is location dependent and not constant throughout the whole specimen.

Especially due to the complexity, which is present in various applications such as gears, wheel to rail contacts or even "simple" sliding, FEM simulations with special regard to temperatures are performed [36, 146–149]. Regarding anisotropic materials as a continuous fiber reinforced PEEK composite, extensive temperature related research was carried out by Varadi and Flöck [42, 103]. Multiple analytical approaches were carried out by Blok, Archard and Ashby [17, 150, 151]. Their mathematical models are different in some aspects, but these models were a prerequisite for many follow-up studies. Blok investigated the line contact between two solid bodies, as it exists e.g. in gears or camshafts [150]. To calculate the flash temperature T_f, the following equation is used:

Eq. 14: $$T_f = A * \frac{q_{av}}{b} * \sqrt{\frac{w}{v}}$$ [150]

w is defined as the width of the line contact and q_{av} the average heat flux. The square root of the thermal conductivity k, the density ρ and the specific thermal capacity c_p of the tested material is defined as the thermal contact coefficient b. The aspect ratio A is dependent on the shape of the heat flux distribution in the specimen. For a homogenous distribution A is set to 1.13 and for a semi-elliptical distribution to 1.11. In applications none of these cases occur, but the deviation is negligible.

According to Blok, the heat flux can be described as:

Eq. 15: $$q_{av} = \mu * F_f * v$$ [150]

While for both bodies in relative movement v is defined as:

Eq. 16: $$v = |v_A - v_B|$$ [150]

The final flash temperature calculation for these contacts is given as:

Eq. 17: $$T_f = 1.11 * \frac{\mu * F_N * v}{b_1\sqrt{v_1} + b_2\sqrt{v_2}} * \frac{1}{l\sqrt{w}}$$ [150]

Blok [150] simplified the contact geometry as a pure line contact, which is as such only valid for higher velocities in order to minimize the error due to a over-estimated RCA, which is dependent on sliding velocity.

In contrast Archard [151] considered the RCA in his calculations regarding flash temperatures. The assumed asperities have a contacting surface A_c of round shape which is described for single contact by:

Eq. 18: $$A_c = \pi {r_a}^2$$ [151]

The ground body is assumed to be a stationary heat source while the counterbody is a moving heat source. Sliding velocity is expressed by the parameters L and N:

Eq. 19 & 20: $$L = v * r\left(\frac{\rho * c_p}{2 * \lambda}\right) \qquad N = \frac{\pi * q}{\rho * c_p * v}$$ [151]

The calculation of the flash temperature, according to Archard is separated, corresponding to their sliding velocities. Small sliding velocities (L <0.1) are considered as a stationary heat source and the heat distributes uniformly into both bodies in contact. Concerning moderate velocities (0.1< L < 5), less than half of the generated heat is taken by the ground body. For higher speeds (5 < L < 100), all heat is taken by the counterbody.

(L <0.1): $T_f = 0.5 * N * L$ [151]

(0.1< L < 5): $T_f = 0.5 * \beta * N * L$ [151]

(5 < L < 100): $T_f = 0.435 * N * \sqrt{L}$ [151]

Factor β is dependent on L and varies between 0.85 for $L = 0.1$ and 0.35 for $L = 5$.

The proportion of heat, which is distributed in both bodies, must be considered. First a calculation of the flash temperatures of each participation body is required. Doing so, it is assumed that each body obtains the whole heat flux of the system. In the calculation, the correct parameters L and N for stationary or dynamic heat source must be used for each body. Subsequently, the division of the heat flux between both bodies is considered in the true temperature T_t.

Eq. 21: $$\frac{1}{T_t} = \frac{1}{T_f^A} + \frac{1}{T_f^B}$$ [151]

The RCA is considered for this model. Due to elastic and plastic deformation states separate equations were presented, for both contact partners being of the same material:

Plastic deformation: $$r_a = \sqrt{\frac{F_N}{\pi * HV}}$$ [151]

Elastic deformation: $$r_a = 1.1 \sqrt{\frac{F_N r_{a0}}{E}}$$ [151]

To obtain the highest possible flash temperature it is assumed that the full load is carried by a single plastic deformed asperity. Hereby HV is the Vickers hardness of the material and r_{a0} the radius of an undeformed, spherical asperity.

Ashby et al. [17] are also considering the average surface temperature, namely the bulk temperature T_b of the nominal contact surface A_n, in addition to the flash temperatures depending on the RCA. Their equations are suitable for different contact geometries but were directly applied to a pin-on-disc test setup. The bulk temperature of the nominal contact surface can be calculated for various geometries according to:

Eq. 22: $$T_a - T_0 = \frac{\mu F_N v}{A_n} \left[\frac{k_1}{l_{Aa}} + \frac{k_2}{l_{Ba}}\right]^{-1}$$ [17]

T_0 is the temperature of the heat sink which can be the holder of the specimen. k_1 and k_2 are the thermal conductivities while l_{Aa} und l_{Ba} are the thermal diffusion distances. This is actually the distance of the heat flux from their origin to the heat sink.

The flash temperatures are calculated accordingly. While for bulk temperatures the nominal contact areas were used, the RCA must be determined for flash temperatures.

Eq. 23: $$T_f - T_a' = \frac{\mu F_N v}{A_r}\left[\frac{k_1}{l_{Af}} + \frac{k_2}{l_{Bf}}\right]^{-1}$$ [17]

l_{Af} and l_{Bf} are the thermal diffusion distances from the asperity tops to the bulk material. Our heat sink in this case has the bulk material temperature T_a'. In contrast to T_a, it is modified as a result of the theory, that if the seizure load is achieved, the flash temperature should be equal to bulk temperature because of complete contact.

Eq. 24: $$T_a' = T_a - \frac{A_r}{A_n}(T_a - T_0)$$ [17]

The RCA calculation according to Ashby was presented earlier in section 2.1.1.

2.2. Characterization Techniques and Measurements in Tribology

It is evident from the previous chapters that tribological systems are complex. In order to characterize tribological systems, their performance as well as the mechanisms, many approaches exist. To complete the state-of-the-art regarding measurement and characterization techniques, tribology test rigs and analysis equipment for ordinary material development processes are reviewed in this section. In addition, special measurement techniques developed and mentioned in the literature are described. A determination, whether measurements were performed during tribological test in-situ or as a subsequent analysis (ex-situ) is given as well. Investigating the changing behavior of the sliding contact, e.g. during the start-up phase of a tribological test, is only possible by in-situ measurements. Special attention is given to the temperatures and the possible intermediate layers, e.g. transfer film and lubricant film with respect to RCA. The important influences of temperatures on the sliding process of polymers were demonstrated by numerous investigations. The RCA has strong influence on the heat transport and is in direct correlation to the temperatures in the sliding contact. The same applies to the transfer film, which can be seen as a dominant influence factor and a good indicator for a proper dry sliding. According to Stribeck, concerning lubricated sliding, the different sliding regimes are a function of the LFT, which affects the sliding characteristics strongly and deserves a closer look concerning the investigation methods.

2.2.1. Tribometers

There is a wide range of possible test rigs for tribological investigations. This is caused by the various kinematics and the different possible scale-up steps from simplified specimen geometry on test rigs up to field tests in combination with special parameter requirements such as e.g. high temperatures, vacuum, aggressive ambient media, etc. Regarding model tests with simplified sample geometries, there are many commercial test rigs available on the market. Due to very specific needs, customized solutions or own designs can be found in many studies. If a simplified geometry test is used, attention should be given to the kinematics. The kind of sliding contact exerts many influences on the sliding process. For example, the counterbody diameter may exert a strong influence on the TFL building process. Also other aspects such as the highest achieved Hertzian pressure or a pressure distribution at the interface between specimen and counterbody should be considered.

Concerning continuous or oscillating sliding under dry or lubricated conditions, the following configurations are commonly used:

- Four-ball tester: In similar configurations also known as ball/pyramid configuration [152–155]. Usually the center ball is driven and the pyramid-plates or other balls remain in position.

- Timken apparatus: Commonly named as plate-on-ring and in a slightly different shape of the specimen called block-on-ring [153, 156, 157]. The test specimen is usually stationary while the counterbody exhibits the movement.

- Pin-on-disc: Probably the mostly used configuration in many studies. The specimen or the counterbody may rotate while the other part is stationary [153, 154, 158].

- Pin-on-slab apparatus: Also used with others specimen shapes like e.g. ball or cylinder. This configuration can be used for single sliding or reciprocating sliding with large, or also high-frequency short throw [153, 159–162].

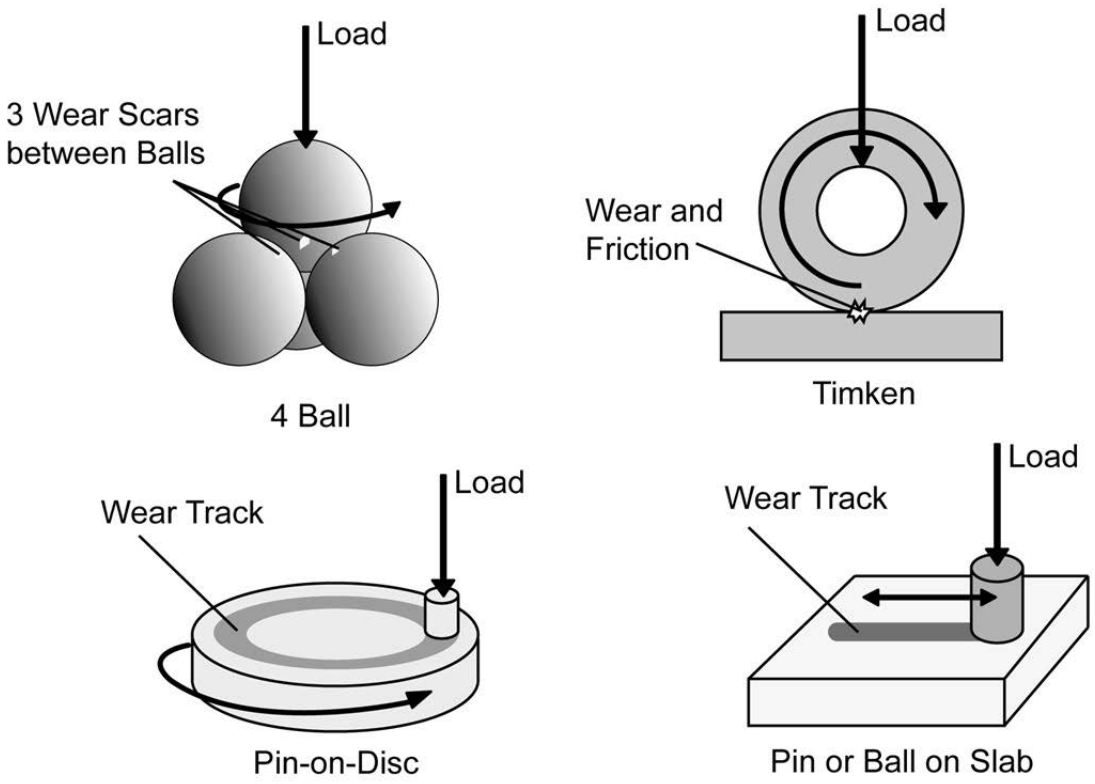

Figure 11: Sample configurations [154]

Tribo-tests with many other contact configurations were developed in the past in order to fulfill the requirements originating from an immense variety of tribological exposures. The basic principle of all test configurations remains the same as two or more bodies are brought into a relative movement using more or less complex mechanical solutions. This basic set-up can be combined with several measurement methods and is dependent on the environmental exposures such as lubrication, third bodies as well as ambient conditions like temperature or pressure. How these conditions are realized and measured will not be described in detail. The measurement techniques for ambient parameters are also well known.

2.2.2. Forces

The measurement of forces during a sliding process is commonly done and found in basically any tribometer as it delivers one of the most interesting parameters, the CoF μ. To obtain μ the normal force as well as the frictional force must be determined. Some of the common measurement methods for basic investigations are:

- Inclined table method [154]
- Hanging weight method [154]
- Mechanical force gauge [31]
- Pendulum method [154]

These methods are based on simple mechanics and therefore quite restricted in their applicability for a time-related tribological exposure. In many investigations, the exposure of a normal force by the means of a weight is sufficient, as it is kept constant throughout the test. In general, we talk about “sensors” of systems which convert a physical parameter to electronic signals [163]. It is obvious that a possible recording of the physical data of a sliding contact is prerequisite for a fundamental analysis. Nowadays electronic transducers are available at low cost and allow measurements of forces recorded over time or distance as well, if desired. The most common principles of electronic transducers are:

- Piezoelectric Transducers: Movement results in strain of a piezo-element, often made of piezo-ceramics, and causes a measurable electrical charge on its surface [164]. This charge can be converted by a measurement amplifier. The main advantage is a very high measurement frequency and bandwidth together with a comparable low deflection of the sensor itself [165]. Movements at a high frequency of several kHz can be determined by piezoelectric transducers. Movements at a very low frequency, especially a nearly steady behavior, cannot be analyzed [154, 166]. The piezoelectric effect is caused by displacement. If the displacement frequency is too low, a drift of the output voltage towards 0 happens due to unavoidable leakage in the electric circuit.

- Resistance Strain Gauge: If an electrical conductor, e.g. a wire, is stretched, the geometrical proportion changes as is the function of Young’s modulus E and the Poisson ratio v. The electrical resistance of the wire is dependent on the geometrical shape. It changes accordingly, if external stress is applied and hence strain evolves [167]. This change of the electrical resistance is very small and therefore usually a measurement amplifier is used. Also, they are usually less expensive than piezoelectric transducers and provide stable measurements in steady-state conditions [154]. High frequencies above the resonant frequency of the transducer are not measurable and therefore, dependent on size and eigen frequency of specimen, often not suitable for determination of e.g. stick-slip behavior [154].

Both types of transducers are widely available in different shapes and also multi-axial combinations [168–170]. Besides normal orientated translational forces, torque and shear forces can be measured depending on the design as well. While the mechanical solutions presented earlier are nowadays mostly used for simple tests, the electronic force transducers are commonly used in most tribometers and studies. The

disadvantages of the introduced electric transducers could be reduced by a combination of e.g. both principles. Because the force measurement is always an indirect measurement over strain, many other methods can also be applied. For example, capacitive sensors [171], laser distance sensors [172], inductive sensors [173] and others [167] can be used to determine the deformations caused by stress.

Standard transducers based on piezoelectric or resistance strain principles in combination with state-of-the-art measurement amplifiers and data acquisition interfaces usually provide a sufficient solution for most sliding tests. A demand, for a more sophisticated measurement is rare and can only be found in very specific challenges, e.g. the determination of stick-slip occurring at high frequencies with very detailed local resolution [154].

2.2.3. Wear

The choice of a wear measurement technique is strongly dependent on the scale of wear occurring during the tests and the necessity of an on-line measurement to observe the wear progress. A high-performing sliding material, e.g. a PEEK/CF coating on a metallic substrate, can provide a specific wear rate of less than $4*10^{-7}$ mm³/Nm [174]. An epoxy based material with nano-fillers shows a wear rate higher than $35*10^{-6}$ mm³/Nm [175]. Material wear rates under abrasive conditions may be much higher. This wide range of possible wear rates limits the multi-purpose use of a single measurement system, as the wear can be too small or too large for the measurement system. Wear happens when two contact bodies move relatively to each other. Wear can happen on both or on one surface only, which is usually the softer one. Also “negative wear” could occur for one surface, if the material is transferred to the surface as a TFL. For an accurate measurement, the distribution of wear on the contacting surfaces has to be considered. Also the geometrical and kinematic conditions are important regarding wear analysis.

2.2.3.1. Ex-situ Measurements

Using ex-situ wear determination methods, the total wear can be determined. If a change of the geometry of the specimen happens during the running-in phase of the test, the determination of wear rate for steady state behavior must be made for an extended test period in order to minimize the error. Observations of different states of e.g. the running-in phase can be made by aborting several tests at the points of interest. Regarding investigations of wear after a tribological exposure, several possibilities are common practice:

- Weighing of the specimen: The mass loss of a specimen can be determined by weighing it before and after the test. Using the material density ρ, the volumetric loss can be calculated. It is an easy and simple to use method, but accuracy is limited for very small wear [30, 154].

- Size measurement: Measuring the specimen's size before and after the test can directly give the volumetric loss but exhibits similar disadvantages as the weighing method. In the past, optical projectors were also used to magnify the specimen for a more precise measurement [30, 154]. A more modern approach is the use of a computer-supported microscope or other optics-related measurement systems.

- Profilometry: Especially for wear which is in the dimension of changes in surface roughness, the use of profilometry systems should be considered. Many surface profilometers or microscopes such as laser- or confocal-based systems as well as tactile stylus gears or atomic-force-microscope (AFM) are used. They provide depth-related data [154, 176]. The resolution of such systems can reach several nanometers in distance measurement [177].

2.2.3.2. In-situ Measurements

In contrary to an ex-situ measurement, start-up phases as well as changes during the tribological exposure can be determined. This approach is particularly useful to monitor an inconsistent or dynamic wear behavior, for example changes of the wear rate, if a TFL is building up and/or breaking down. Due to the integration in the tribometer, several aspects from a physical and a mechanical point of view, such as temperature elongation of mechanical parts should be considered, as well as possible disturbances of the sensor techniques by e.g. wear particles. Several measurement techniques are introduced in the following. Measurement frequency is not especially considered since these techniques are intended for the use of wear monitoring over longer periods of time whereas all the systems offer a sufficient data acquisition rate.

- Distance measurement: In a tribometer usually one of the bodies in contact must be kept able to move in order to compensate for the worn volume. The travel of this movement can be measured [30, 154]. Depending on the specimen's size, the wear rate and also the cost, a wide range of usable distance sensors can be selected. Besides laser-, capacity-, inductive- and Eddy-current based systems, more exotic distance measurements would be possible but are not necessary. The mentioned systems provide a sufficient perfor-

mance, since resolutions and the linearity of some high-performance sensors usually exceed the mechanical stiffness of the test rig. Distance measurement is commonly used as on-line measurement method, especially for polymer tribology model tests [83, 99, 178].

- Radionuclide surface activation: An especially developed measurement method, relating to small amounts of wear and the use in closed systems. Wear is determined by measuring the amount of radioactive marked particles, which were worn from the surface of the specimen and carried away to e.g. a catchment basin. A combined wear rate measurement of several parts is possible but reported as inaccurate. Due to the radioactive marking the measurement technique is a latent hazard [30, 154, 179, 180].

- Ultrasonic interference: If ultrasonic sound is emitted in a body, every surface causes interferences and reflections. By measuring the time delays, respectively the phasing of the signal, precise measurements within the accuracy of 0.75 µm can be achieved. Although this method seems to be an interesting approach, it was reported that the use is mainly limited to simplified laboratory tests as otherwise disturbances rise severely [181, 182].

Besides the introduced measurement techniques, several other approaches can be found for specific investigations or for testing under special conditions as e.g. the interpretation of acoustic “tribo-emissions” [183] or using an optical charge coupled device (CCD) camera [184]. Element-analysis via X-ray fluorescence spectroscopy, atomic absorption spectrometry or similar methods can also be used to determine very small wear [30].

2.2.4. Temperatures

The determination of temperatures during a tribological test is a widely investigated topic. Excellent and extensive reviews about the state of the art regarding temperature measurement methods in the field of tribology can be found in [120, 154, 185].

2.2.4.1. Thermocouples

Thermocouples are commonly used for temperature measurements. This method is based on the Seebeck-effect, which describes an electrical voltage gradient on an electrical conductive material if a thermal gradient is present. The mechanisms behind this method are thermal diffusion processes by electrons which are not leveled out within the material. The accuracy depends on the material combination as well as

the calibration. Regarding all methods introduced, the accuracy is within a few degrees and therefore in an acceptable and sufficient range for tribological investigations. The differences in measurement quality are mostly related to heat flow disturbances and the type of the measured temperature as well as the time-related resolution. To obtain the bulk material temperature, which is position related, thermocouples were attached and embedded in specimens in various studies although they are rarely mentioned in the report [186, 187]. An approach to determine the average surface temperature is difficult with embedded thermocouples. Obtaining the flash temperatures is not possible at all due to mass and response time [120, 185]. Additionally, the embedding of several thermocouples for a temperature mapping of the surface is a difficult task, and the heat flow disturbance of the thermocouples itself cannot be neglected [185]. Thermocouples are often chosen for test rigs to monitor ambient conditions, lubricant temperature, etc. Another technique is the physical-vapor-deposition (PVD) of thin film thermocouples with a thickness of ~2 µm on the surface as used by Tian et al. [188]. They provide the average surface temperature or, resulting from a small mass and a high time resolution of less than 1 µs, even flash temperature data [188]. This technique is limited by wear, as it can damage the thermocouple or its calibration [154]. Furthermore, the contact between the sliding partners is not directly measured, but the contact between thermocouple-film and one of the sliding partners. Temperature mapping using an array of PVD thermocouples is also possible as demonstrated by Kennedy et al. [189].

A third method is the use of electrically conductive sliding partners in order to build a dynamic thermocouple, also called Shore-Gottwein-Herbert technique [185]. In this measurement the sliding partners themselves build the thermocouples. Extensive studies were done by Bowden and Ridler using a modified pin-on-disc tribometer in order to measure the average surface temperature using dynamic thermocouples [190]. Chang et al. evaluated the effects of speed and load on the interfacial temperature using a reciprocating pin-on-slab test rig with a dynamic thermocouple setup [191, 192]. Concerning electrically conductive and isotropic materials, the measured voltage is a function of the average temperature over the contact surface. Depending on measurement equipment and post-processing, flash temperatures are likely to be measured [193]. Usually, a static calibration is used. Its validity for dynamic situations is questionable and must be executed separately for every new specimen [185]. When applying this technique, effects of the tribo-electrification must be considered. A Tribo-electrification occurs if wear debris transfers from one material to the other and causes a charge transfer, resulting in measurable voltage [194].

2.2.4.2. Radiation

Depending on their temperature, surfaces exert certain radiation as determined by the Stefan-Boltzmann law. It claims that the radiation increases with higher temperatures, while according to Planck's law most emissive power is provided for wavelength between 1 µm and 10 µm [120]. These wavelengths belong to the infrared (IR) light spectrum, which is the reason why usually IR-temperature measurements are executed. It is comparatively straight forward to access surfaces from specimen or counterbody which are not in contact as e.g. done by Thevenet et al. [195]. An approach to determine the temperature on the sliding surface demands more complex solutions. Several attempts were made by choosing glass or sapphire glass as one of the sliding partners. Glass exhibits some material characteristics comparable to steel and is transparent for specific radiation wavelengths [120, 196]. Also optical fibers, embedded in one of the sliding partners were used since they provide a smaller disturbance on material and sliding characteristics [197]. Radiation measurements were done in the past using photography, pyrometry, thermal imaging, and photon detection [120]. Photography with an IR-sensitive film or regular color film is, depending on the method, reported to be restricted by exposure time and measurable temperature range regarding flash temperature imaging [120]. Pyrometers which are based on IR-detection show other limitations. Line-scanning thermal imaging methods require a certain time for a complete scan and can therefore miss certain flash temperature spots, even if scanning time is in millisecond range. The use of a single spot is determined by the correlation from spot diameter to the fact that the average temperature in the spot is measured [120]. This means that a small measurement spot can miss the location of the maximum flash temperatures while a spot too large measures an average of flash and surface temperature. Also the change of emissivity can have a strong influence on the results gained by IR-methods. Specialized techniques, namely two-color thermometry, can overcome this difficulty as Thevenet et al. have shown for brake disc investigations [195]. Using a photomultiplier to collect photons emitted from contact spots, Suzuki and Kennedy found flash temperatures within the time frame of less than 2 µs using a time resolution smaller than 30 ns [198]. However, there is a limitation, that a certain minimum temperature of approximately 500 °C must be achieved for using this measurement technique. Additionally, the spot area emitting the photons must be accurately determined.

2.2.4.3. Structural/Chemical Observations

In addition to the mentioned in-situ applicable measurement techniques, several investigations were carried out using ex-situ analysis for the average surface tempera-

ture determination. Concerning metals, a metallographic investigation of the worn surfaces regarding micro-hardness and microstructural changes can give information about the temperatures which occurred during sliding. Therefore, worn metal surfaces are compared with temperature-treated reference-specimen [199]. Other approaches used thermal-sensitive paints or powders as they show a temperature-related color change or have a constant melting point, respectively [185]. However, even with sophisticated applique methods for powders using PVD, a surface modification takes place. This could disturb tribological investigations and might be the reason why all methods based on chemical effects were only used to investigate cutting tools. High accuracy was not reported for any of the ex-situ temperature determination methods.

2.2.5. Transfer Film

Transfer film analysis contains imaging, surface topography determination as well as element investigations. The measurement methods are investigated according to their ability to trace the development of a TFL during the test or only afterwards. It is surprising that only a few investigations were conducted using in-situ measurement techniques. Relating to surface imaging, topography and element analysis, plenty of analysis methods can be applied. Below, a summary of the mostly used methods is given.

2.2.5.1. Optical Microscopy

Although the resolution is limited, an optical microscope is a commonly applied analysis method, found in many publications with a closer look at TFL [71, 81, 94, 99]. Mostly, it is found as a reflecting-light or a transmitted-light type and its resolution is around 500 nm. Special gear goes up to 50 nm [200] with a magnification of around 1000 [201]. Even if the implementation of an optical microscope into a test rig appears relatively easy, in-situ microscopy of TFL were not reported in literature. Enhanced, confocal microscopes were applied from time to time for transfer film investigations [202]. Due to the elimination of out-of-focus light by illuminating only a small area at the time, they offer a high resolution, depth of field and surface topography information, but are much more expensive [203]. Another technique, the holographic microscopy, uses the interference patterns of reflected coherent, monochromatic light [204]. Both, the confocal as well as the holographic microscopes, provide 3-dimensional data. Holographic microscopes have already been used for in-situ characterizations by Korres et al. [205].

2.2.5.2. Scanning Electron Microscopy

A resolution smaller than 1 nm can be obtained by the use of scanning electron microscopy due to the much shorter wavelength (e.g. 0.017 nm for 5 kV acceleration voltage) of the emitted electron beam compared to normal light. In contrast to the optical microscope, it is a line-scanning based method and reaches very large depths of field. As it provides excellent possibilities and is often available for researches, many publications contain SEM results regarding TFL investigations [90, 93, 94, 97, 99, 106, 107, 206]. An even higher resolution is obtainable using transmission electron microscopes (TEM). Due to high cost and time-consuming sample preparation effort, it is rarely used for TFL investigations [207]. REM or TEM analysis is commonly used ex-situ. Due to the mentioned disadvantages and the additional, large effort needed , only one publication was found investigating the single asperity sliding for fundamental contact research in-situ via TEM [208]. However, an up-scaling of this method seems not to be possible.

2.2.5.3. Atomic/Friction Force Microscope

In an atomic force microscope (AFM) or friction force microscope (FFM), a lever with a diamond tip is driven across the specimen as a line-scanner. The tip is exposed to atomic forces, exerted by the surface. Several methods exist which differ in their course of action. Depending on the applied method, the lever is oscillating or static. Height differences are compensated and measured by changing the specimen's position (active feedback loop) or by a deflection of the lever [209]. A novel technology, namely peak-force-tapping, considers energy-related changes due to tip-specimen interaction and prevents lateral forces while providing additional data [210, 211]. As it is a line-scanning based method, the exposure time is considerable. Already the first attempts by Binnig et al. achieved resolutions of less than 1 Å vertical and 30 Å lateral [212]. The use of these methods for surface characterization offers a wide range of characterization possibilities. Besides imaging the surface topographies, the surface roughness can be determined using AFM as well [202]. The use of nano-indentation or FFM enables the measurement of adhesion, micro/nano-friction and scratching as well as hardness and Young's modulus of surfaces [100, 213–216]. Since the possibility of micro-sliding, nano-indentation, etc. can be seen as a test instead of a pure analysis method, a clear separation of ex-situ measurement and combined in-situ testing and measuring is difficult to do.

2.2.5.4. Profilometry

Besides commonly known stylus profilometers, there are laser and confocal based systems. In comparison to SEM and AFM/FFM, this is a line-scanning method where a lever or optical beam is collecting depth-related data. Depending on the used principle, a high resolution of several nanometers is possible [177, 217]. While a stylus profilometry is tactile, the optics based systems are non-contacting. Depending on the system, surface's roughness, topographies and wear volumes can be determined. The systems are available at reasonable cost and can be found in many publications regarding tribology [218–224]. Only ex-situ characterizations were found during the literature research.

2.2.5.5. Chemical Analysis

Several approaches to determine the chemical structure of a surface were taken, mainly depending on infrared-, nuclear-magnetic-resonance-, x-ray-, auger-electron- and raman-spectroscopy. Infrared- and raman-spectroscopy are based on the investigation of monochromatic or infrared-wavelength light, reflected by the surface [225]. Auger-electron-spectroscopy is based on the investigation of emitted auger-electrons, activated by an inserted electron beam while the x-ray spectroscopy uses emitted photoelectrons activated by an x-ray beam [226, 227]. The nuclear-magnetic-resonance detects changes in an emitted electromagnetic field caused by isotopes featuring a magnetic spin [228]. In contrast to the other spectroscopy methods, the nuclear-magnetic-resonance spectroscopy is able to analyze the sub-surface. These techniques are common methods and can be found in several publications regarding tribology, mainly using ex-situ raman-, x-ray- and infrared-spectroscopy [90, 94, 102, 229–231]. Auger-electron-spectroscopy was also applied in-situ by Brainard and Buckley [232].

2.2.6. Lubrication Film and RCA

LFT was measured extensively in the past and several good working methods are known. The dimension of the measured thickness requires special attention, as for boundary lubrication, the average thickness is below the surface roughness. In regard of hydrodynamic lubrication, several micrometers can be achieved [233]. A specification on whether LFT is measured from a surface roughness median or from the highest asperities is usually not found. As most of the measurement techniques are limited to hydrodynamic or EHD measurements, a median to median distance can be expected as result since all techniques, except AFM/FFM, are using average

values over a certain area. In contrast to e.g. TFL investigations, most of the measurement techniques are applied for in-situ measurement. Separation of the contact partners by the lubrication film exerts strong changes to RCA in lubricated sliding conditions. During the research for the state of the art measurement techniques, it was found that similar methods were used for RCA and LFT determination, even if RCA analysis was partly only conducted for dry sliding. Therefore the summary of measurement techniques for both is combined. The measurement techniques can be classified into optical, electrical and mechanical methods with some additional specific technologies, in our case a magnetic field analysis, AFM/FFM, thermal and ultrasonic sound analysis.

2.2.6.1. Mechanical Methods

In 1978, Schrader used a stylus pen embedded in the specimen to measure the distance between both sliding surfaces. Further attempts using this technology could not be found due to its disadvantages, namely the lubrication film disturbance by the stylus, the additional mechanical load by the stylus and the slow response time of the system [234].

2.2.6.2. Electrical Methods

Two approaches were made using electrical properties and effects to determine the LFT. It is distinguished between resistive and capacitive methods. Both require electrically conductive sliding partners for the measurement. These can be substituted by the addition of conductive fillers in case of polymer compounds, a conductive coating or the use of evaporated or otherwise attached electrodes [234]. Relating to a resistive measurement, the electrical resistance is measured through the usually very low conductive lubrication film for EHD or pure hydrodynamic lubrication regime. Qualitative results related to the RCA, indicating contact, minor contact or complete separation can be achieved. Concerning embedded electrodes, serious disturbance of capacitance influence of the oil, especially at higher speeds, were reported in case of reciprocating elastomeric seals, limiting the usability of this method [235]. Capacitive measurement is only possible in EHD and hydrodynamic lubrication regimes as both conductive surfaces form a plate capacitor, which would not work if direct charge-balancing would take place. It is used in several studies while setting the capacitance in relationship to the LFT [236, 237]. Both methodologies can be applied by calculating the relationship between the measured resistance or the capacitance to LFT, or by an experimental calibration. In none of the cases a high accuracy was achieved regarding thin film measurements [235, 237]. With reference to RCA determination, a

resistive measurement method was executed by Bowden and Tabor concerning stationary and moving surfaces in dry contact [16]. Bhushan applied the measurement method on magnetic rigid discs [238]. Also, Archard did basic investigations using resistive measurement methods to describe the contact and the rubbing of flat surfaces back in early 1950, perpetuating some basic ideas of Bowden and Tabor. Recent attempts with an enhanced measurement setup using thin film coating with high electrical resistance were conducted by Sick and Ostermeyer [239]. The electrical resistance for metallic contacts is usually very low. This causes some difficulties in an experimental examination. To overcome this issue, thin film coatings are used as they provide higher electrical resistance and offer a more precise analysis. In summary, the resistive electrical measurement method gave good indications and correlations regarding junction sizes and number of contacts. This leads to a better understanding of contact characteristics in several publications. Regarding dry sliding results, a resistive measurement method can be expected to be in direct correlation to the RCA. Publications offering more detailed information about this connection and usability could not be found. Electrical measurement methods are suitable for in-situ measurements of static and dynamic contact.

2.2.6.3. Optical Methods

Prerequisite for optical methods is that one of both sliding partners must offer an (at least partly) optical transparent characteristic. The transparency must match the wavelengths applied in the experiments and may block others. The usage of a transparent material already determines the usability of mixed and boundary frictions as material properties are fundamental for these lubrication regimes. Concerning EHD, different material parameters must be taken into account. Average LFT is generally measured in-situ. Several measurement set-ups based on various physical concepts were used. The interferometry offers resolutions up to 0.02 µm and is based on the phase-difference of the reflected, initially coherent light beams which interfere with each other and evolve constructive or destructive interferences [234]. It is a common method and was applied in several studies [240–242]. Using ellipsometry, polarized light is emitted to the counterbody and the changes in polarization are detected. The maximum measureable film thickness is around 500 nm and the complexity of data evaluation can be a limiting factor. Only few studies were made based on this technique considering mixed and boundary lubrication regimes [243, 244]. Reflection-absorption infrared spectroscopy is based on increasing absorption of specific wavelengths from emitted infrared light with growing LFT. It provides a good vertical resolution and is suitable for measurements in mixed and hydrodynamic lubrication re-

gimes and can give additional information about chemical changes in the interface and lubricant [245]. Another possibility is given by Visscher, using a focus-error detection system [234]. Distances can be measured if the focus-error of the reflected light is determined by using e.g. photo-electrodes [234]. Other techniques such as moiré pattern method or fluorescence-spectroscopy exist but are rarely used and therefore are not introduced in more detail due to their bad usability or inadequate resolution [234, 246]. Concerning RCA determination, optical methods are the commonly used approaches. Interferometry was used by Bhushan and Dugger on magnetic discs, using a glass counterbody [238, 247]. Profilometry, based on optical distance measurement using laser or confocal techniques, was conducted by Down et al. [248] as well as by Hendriks and Visscher [249]. Methods of optical microscopy with an image analysis software offer access to static RCA contact conditions as well, as shown by Váradi et al. [21] and Flöck [42]. Optical methods regarding the RCA determination using a glass counterbody are usually limited to static or quasi-static conditions during pre-sliding, as shown by Ovcharenko et al. [250].

2.2.6.4. Magnetic Induction

Regarding this technique, a magnetic field is produced by a coil in one of both sliding partners. The coil should be almost uncovered by electrically conductive and magnetic material as otherwise the magnetic field is damped. The other sliding partner should provide an electrically conductive characteristic, which can be ferromagnetic as well as non-ferromagnetic. The influences of the counterbody on the emitted magnetic field of the coil and its inductance can be determined by measuring the electrical impedance of the coil which is in direct relation to the distance [234, 251]. Concerning primary non-conductive counterbody materials, there were also approaches of filling e.g. elastomers with magnetic particles or using a magnetic lubricant [246]. Such sensors with resolution of up to 20 nm are commercially available and are also used for piston ring LFT measurement [252, 253].

2.2.6.5. Ultrasonic Method

Using an ultrasonic method, the surface-reflections of focused ultrasound, which is sent through the specimen to the counterbody or vice-versa, are analyzed regarding phasing and changes in amplitude in order to obtain distance information. This technique was used in publications for EHD and pure hydrodynamic contacts for application-near investigations such as bearing and piston ring tests [254, 255]. According to the results of Gasni and Dwyer-Joyce, depending on the used frequency, the resolution can be expected in the range of 50 nm for thin LFT [255, 256]. Such measure-

ment systems are also commercially available [257]. Investigations of RCA using ultrasonic methods were done by Baltazar et al. [258]. Taking into account material properties such as elastic and plastic deformation behavior under changing load conditions, correlations were established giving the RCA as a result. As this method provides a static RCA only, it is also not suitable for in-situ measurement.

2.2.6.6. Atomic/Friction Force Microscope

All the measurement techniques described above allow a measurement of EHD and hydrodynamic lubrication regimes but are limited to a great extent regarding mixed friction. Two approaches were taken by Koinkar and Bhushan [259], to determine LFT on a single spot or the distribution of LFT over a certain surface area for boundary friction conditions using AFM/FFM microscopes. To determine a precise one-point thickness, the distance between the changes in normal force of the tip, when lubricant is contacted up to solid substrate contact, can be measured [215]. For surface LFT distribution, friction force maps can be produced. The friction force can be directly correlated with the LFT for each specific micro-sized point, also considering single asperities [215, 259]. Similar to the transfer film characterization, AFM and FFM are not analysis tools exclusively as they also enable sliding tests. Special attention should be given to the very high resolution of this technique. It reaches a sub-nanometer resolution for the vertical axis and a resolution in nanometer scale on the lateral axis [259, 260].

2.2.6.7. Thermal Measurements

Another interesting in-situ approach regarding the determination of the RCA is executed by Vick and Schneck [261, 262], by correlating the temperature near the sliding contact with the CoF and the RCA. The frictional heat is dependent on the CoF while the heat dissipation is related to the temperature and the RCA. Although the basic idea is correct in terms of physics, many uncertainties and disturbing influences have an effect on this measurement method. Especially the difficulties to measure the flash temperatures, which are directly related to RCA, can limit the usability of this method. The importance of total energy input and frictional heat together with RCA is mirrored in this study.

3. Objectives and Methodology

The purpose of this thesis is the advancement of tribological research possibilities by creating a new insight into the tribological system using highly sophisticated measurement techniques. Applying such techniques successfully will enable the determination and better understanding of micro-sized sliding and contact characteristics. The data obtained will facilitate the establishment of essential structure-property relationships, leading to a profound knowledge of processes within the sliding contact. These measurement techniques will influence future material development of tribologically optimized polymer compounds significantly. Because of the better understanding of the system behavior, materials development will be more efficient and less time consuming since for example less filler compositions have to be investigated. Prior to the implementation of additional, high sophisticated measurement techniques in a model test rig, existing measurement techniques used in metal tribology research were reviewed as a reference. The methods selected were adapted and modified accordingly, in order to match the special characteristics of polymer tribology. After validation, the measurements were applied within a study of failure mechanisms under increasing load conditions. The results demonstrated the immense support provided for a description of the sliding characteristics by employment of these additional measurement techniques.

The literature research and overview in section 2 demonstrates the importance of **real contact area** together with **lubrication film thickness**, **transfer film layer thickness** and **interface temperature** as well as the demand for new measurement techniques. In order to properly select possible superior measurement techniques, selection criteria had to defined. The most important point is the fluctuating and evolving characteristic of a tribological system. Since a detailed behavior had to be analyzed, it was highly desirable to apply an on-line measurement which provides sufficient data over time. Also, the disturbance exerted on the tribological system by the measurement equipment itself should be as small as possible while providing a robust, efficient and reliable measurement.

Prior to selecting the measurement techniques, the tribological system had to be defined more precisely. For the current investigation it was anticipated that the configuration of interest is positioned in macroscopic sliding dimensions with continuous or reciprocating sliding kinematics when polymer composites are applied against a steel counterbody. The focus hereby is on dry sliding, as polymers exert their advantages over metal-metal combinations especially under these environmental conditions. Nevertheless, applied solutions shall, if possible, also be adapted to lubricated sliding

conditions. Possible solutions, obtained through earlier literature research, were evaluated in the value analysis, given in Table 1.

Rating: 0 = Worst Fit 10 = Best Fit Criteria	Quantifier	Interface Temperature					Transfer Film Layer					Real Contact Area			
		Embedded Thermocouples	Surface Thermocouples	Dynamic Thermocouple	Infrared Radiation	Photomultiplier	Optical	SEM	AFM/FFM	Profilometry	Chemical Analysis	Electrical Resistance	Electrical Inductivity	Optical Methods	Thermal Measurement
Expected Robustness of Measurement	6	8	2	6	8	6	6	4	4	8	8	6	4	8	3
Non-Disturbance on Sliding System	8	8	1	9	2	2	10	8	3	10	10	9	9	2	9
Low Cost and Effort	4	7	2	8	2	0	3	1	2	8	3	9	9	2	2
On-Line Measurement Capability	9	10	10	10	10	8	2	1	1	7	7	8	7	1	4
Accessibility to Real Interface Temperature	7	1	6	8	6	8									
Level of Detail of Surface Topography	3						6	9	9	7	4				
Resolution of Contact Condition	2											1	1	8	1
Σ (Quantifier x Rating)		237	160	**286**	204	180	164	128	92	**244**	215	**218**	197	97	136
Standardized Results [%]		83	55	**100**	71	63	67	53	38	**100**	88	**100**	90	44	62

Table 1: Selection of measurement techniques

The only possible solution to measure the real interface temperature without exerting severe disturbance to the sliding system was found in the dynamic thermocouple measurement technique. For TFL investigations, no technique is known to obtain the overall depth-related topography for medium to high sliding speeds, while changes in average thickness can be determined by using a “simple” optical distance measurement. So good results are obtained regarding the progress of a TFL during the test. A convenient available solution was found in high-resolution confocal sensors which could monitor the development in thickness of a TFL outside the sliding contact. Former researches proved the measurement of electrical resistance to be suitable for RCA determination in dry static conditions using metals. Furthermore, it appeared to

be a promising approach for lubricated sliding as well. So in combination with the other selection criteria it was the preferred solution.

Figure 12 shows the flow chart of this work. The first step describes an analysis of the state-of-the-art for common measurement techniques and development of methodologies. Additionally, modern sensor and measurement systems were investigated. As a result of this preliminary step the most promising measureable parameters and measurement approaches were selected.

The second step describes the implementation of different measurement techniques in a state-of-the-art tribology test rig. Not only the mechanical integration of the sensors was required, but also an electronic and software implementation. Additional testing sequences and measurement algorithms were also investigated in this step.

The results of the measurement tests were discussed afterwards in the validation stage (stage 3). Prior to this, a proof of principle had to be completed. Depending on the measurement techniques there were several options for proof. One approach was the simulation of single aspects of the sliding process using modern multiphysics finite element software (FEM) or analytical calculations. Ex-situ analysis techniques, applied after sliding tests, were also used to prove measurement results.

After the proof of principle, an evaluation of the results was conducted in step 4. Correlations of the results provided by various sliding tests with ordinary, but well known parameters like CoF μ or wear rate $W_{l/s,}$ were most interesting. Different load cases regarding sliding velocity, normal pressure and counterbody temperature had been applied to understand the system and correlations behavior.

In order to gain an idea of the complete system and interdependencies of the measured characteristics, a final test procedure was conducted. Besides combined measurements, failure conditions were investigated to correlate them with additionally obtained data and to establish important design issues for sliding applications.

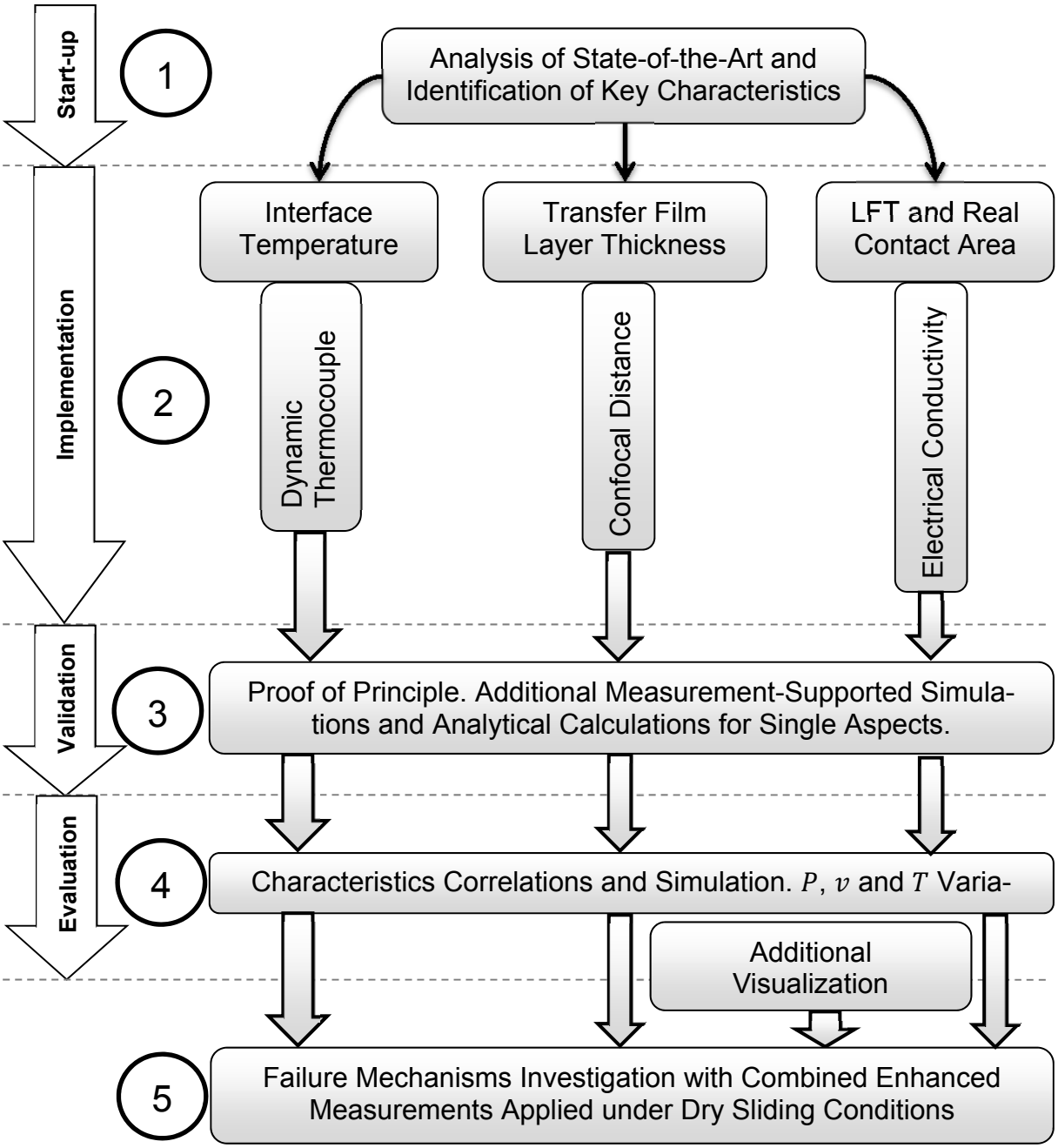

Figure 12: Methodology

4. Enhanced Theory of Measurements, Models and Implementation

4.1. Intermediate Layer and Contact Characterization

4.1.1. Confocal Measurements

4.1.1.1. Principle of Measurement

The confocal sensor, selected for intermediate layer thickness measurement, provides a distance measurement. A lens array splits up the polychromatic white light into several monochromatic beams as shown in Figure 13. Every beam has its own calibrated focus point on a specific distance in front of the sensor [263]. The reflected monochromatic light beams are imaged through other optical arrays on a spectrometer, nowadays often found as charge-coupled-device (CCD). The monochromatic light wavelength, focused on the reflecting object, is taken into account for the evaluation and it's relating distance is correlated. The focused wavelength is obtained as it provides the highest intensity per area on the spectrometer [263].

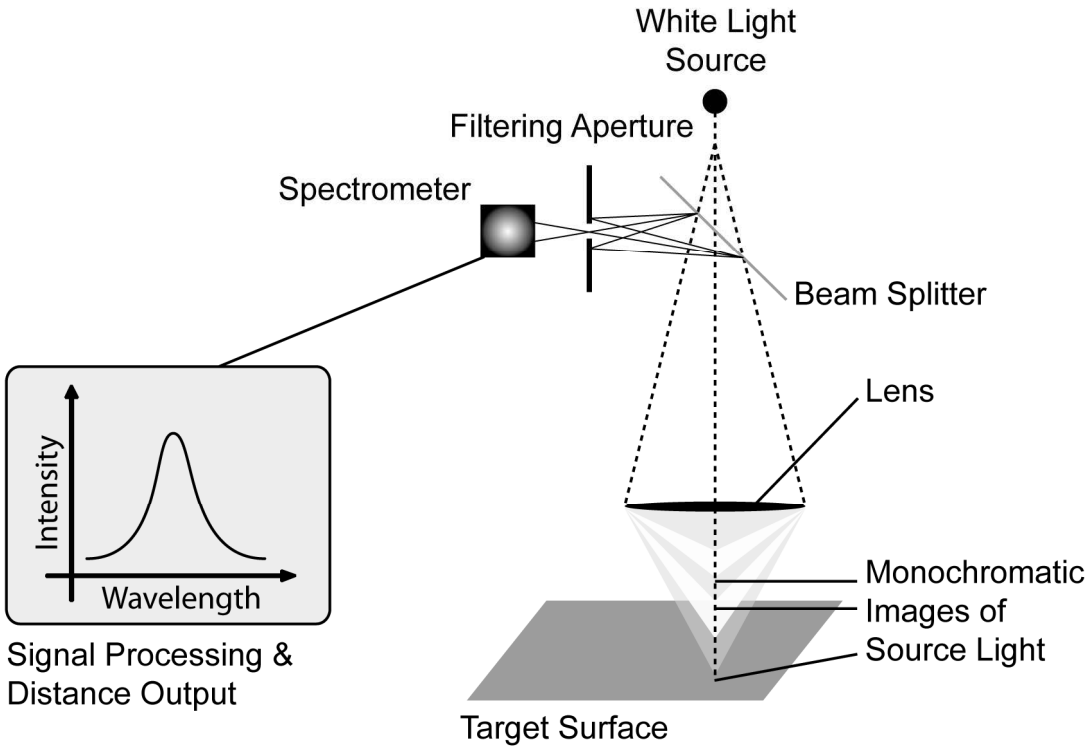

Figure 13: Confocal measurement principle [263]

For the layer thickness measurement, the time dependent change in distance must be recorded starting from the initial state without any surface layer to have reference data. Using this measurement, the resulting data instantly supply an average of the surface thickness information.

4.1.1.2. Implementation

The chosen confocal sensor system was a ConfocalDT IFC2451 controller combined with a 2401-0.12 sensor (MICRO-EPSILON MESSTECHNIK GmbH & Co. KG; Germany). The provided resolution was 0.005 µm within a measurement range of 120 µm. The light spot diameter of the focused wavelength was 7 µm and a measurement rate of 10 kHz was possible.

Regarding the pure average layer film thickness measurement on one line across the counterbody, several problems had to be solved. First of all, the temperature related change in the diameter of the shaft was considered. Using the coefficient of linear thermal expansion of iron ($11.8*10^{-6}$ K^{-1} [264]) for 30 mm radius just for an approximate calculation, a change of 10 K already results in 3.54 µm change in the measured distance. During the tribological test the temperature varies in much larger scales, resulting from frictional heating or purposed heating of the shaft in order to set environmental conditions. Those temperature differences could even result in exceeding the provided measurement range of the sensor. For example, a temperature difference of 170 K is already half of the possible measurement range. The desired thickness to be measured was in scale of only a few µm or in case of thin transfer film even in the range of sub-µm. A temperature compensation was therefore absolutely necessary.

One possible route was to obtain a calibration curve in a reference test using the counterbody's bulk-temperature T_{CbB} for use in later tests as compensation. A very careful setting of the sensor distance was required in order not to exceed its measurement range. Additional to temperature effects, the shaft itself has an unbalance of approximately +- 10 µm, which can hardly be improved within these testing dimensions. With continuous recording, the unbalance of the shaft was leveled out by several turns because of the high logging frequency of 10 kHz and average building for 1/s.

Another possible solution to compensate thermal expansion was the implementation of a reference-algorithm. Here a continuous scan of several turns on the layer film was performed first. Afterwards, the sensor moved in x-direction to a pristine surface area and several turns were scanned. The difference of the mean values achieved from both measurement positions can provide the thickness as absolute values, compared to the initial reference value. This procedure had to be obtained prior to every test while both surface sections were still in their original condition. In pre-tests, an average of over 25 turns at speeds above 1 m/s (time period of ~4.7 s for 1 m/s)

with a measurement rate of 10 kHz was found to be a good compromise between unbalance-compensation and acceptable temperature influence. For 1 m/s 94000 single measurements had to be applied to obtain one thickness information. It took about 40 s to complete one measurement, which underlines the disadvantage of this attempt as rapidly changing conditions cannot be monitored. Both of the possibilities presented for temperature compensation were pursued and evaluated. The perfect solution to this temperature problem would be a second confocal sensor for temperature compensation only, which could not be used due to the high cost involved.

Setting up the initial distance of the sensor manually was a difficult task. Due to this fact and the need of another axis for the reference-algorithm, a complete X-Y motion table was implemented. Originating from a discarded laser-profilometer, it provided an excellent theoretical resolution of 0.25 µm. It was piloted by two EPOS2 24/2 controllers (Maxon Motor GmbH; Germany) linked by a CAN-Bus interface, connected to the control system via USB for implementation into the LabView (National Instruments Germany GmbH; Germany) environment. The LabView environment created was supervised by programmatic scheduling, enabling the selection of continuous measurement or reference-algorithm mode.

A schematic of the basic setup is given in Figure 14, showing the confocal sensor, the X-Y table and the surface traces which were evaluated.

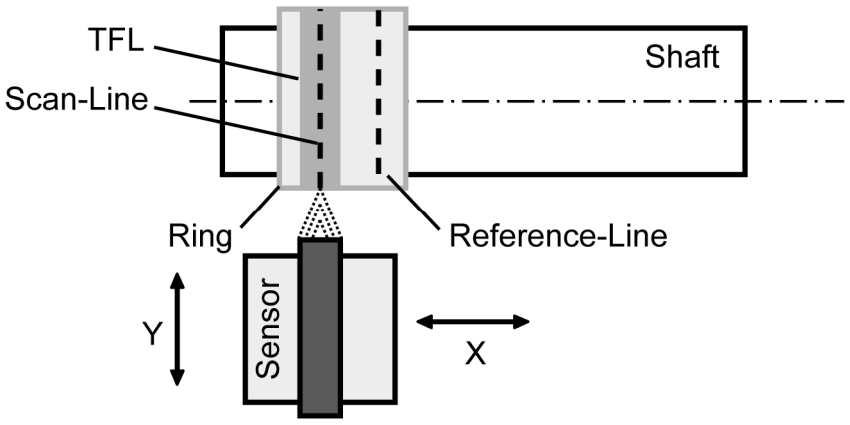

Figure 14: Top view of the implementation of confocal measurement

If the confocal measurement was initialized, the sensor was driven in Y-direction and stopped at a distance of approximately 0.25 mm near of its measurement range limit. Subsequently it was driven at low speed of 20 µm/s and stopped in a measured distance of 50 µm towards the rotating counterbody surface, what marks approximately the center of the measurement range. For a continuous measurement, this was done initially every time the measurement was activated. It can be helpful to stop and reactivate the measurement, if e.g. much higher temperatures were selected and the

range has to be re-adjusted. In this case a new reference has to be obtained first. For reference-algorithm, the automatic adjustment of the measurement distance was also conducted. If the measured average distance value exceeded the range of 30-80 µm, the adjustment of the measurement range was repeated for the reference-algorithm. As only relative differences between both measurement areas were of interest, this ensures that temperature effects do not violate limits of the measurement range. Measurements at changing temperatures were possible with this method without obtaining a new reference. In summary, a resolution in sub-µm range was expected using this implementations.

4.1.2. Electrical Conductivity

4.1.2.1. Principle of Measurement

The electrical resistance R of materials can be measured easily. If the geometric aspects of a measured body are taken into account, the resistance may be expressed as a specific electrical resistance ρ_{el}. For the determination of R or ρ_{el} respectively, the following equations are valid:

Eq. 25 & 26: $$R = \frac{\Delta U}{I} \qquad \rho_{el} = R\frac{A_0}{L_0}$$ [265]

Using these equations within a closed electrical circuit, ΔU is the drop of voltage between both contact surfaces of the specimen while an electrical current I is applied. For a specific resistance, A_0 determines the contact surface area and L_0 the length of the specimen. The electrical conductivity of materials is inversely proportional to the electrical resistance. The relationship of conductivity S to the specific resistance ρ_{el} is given by:

Eq. 27: $$S = \frac{1}{\rho_{el}}$$ [265]

During the sliding test, R was measured using a state-of-the-art multimeter. In a tribological test using this measurement technique, the polymer specimen has the strongest impact on the measurement result, since it usually provides a much higher resistance than the metal counterbody and the specimen holder. The measured resistance R is in direct correlation to ρ_{el}, L_0 and A_0. ρ_{el} is a material dependent parameter and does usually not change significantly during a sliding test as long as temperature and pressure are not severely altered. For experiments, L_0 should provide a minor change in relation to its initial length due to wear. Otherwise the difference has to be taken into account. As the equations show, the only variable left is A_0.

It is known that the real contact area A_r is often smaller than the nominal contact area A_n, except for very high pressures. While for static investigations of electrical resistance A_0 equals more or less A_n, due to the conductive paint argent finish G3692 Acheson Silver DAG 1415 (Plano GmbH; Germany), A_0 is similar to A_r for sliding contact conditions. According to the RCA theory of Ashby et al. [17], A_r depends on the contact geometry aspects and A_n, H_0, μ and F. In addition to these variables, the intermediate layer must be considered as well. Former results indicated a high electrical resistance and isolation behavior of the TFL [99], which is also provided by oil, depending on type and content. For the engine oil applied, type CS-M1 (FUCHS EUROPE SCHMIERSTOFFE GMBH; Germany), an electrical conductivity could not be determined with the Keithley 2601A nor the Fluke 8846a multimeter, indicating a resistance above $1*10^{-9}$ ohm. Therefore the oil can be declared as an isolating component in the tribological system. If load-carrying asperities, which are parts of A_r, are separated by the intermediate layer, they will not contribute to the electrical conductivity of the sliding contact. Additionally, the formation of an intermediate layer can lead to a separation of both conductive sliding partner surfaces, which leads to fewer asperities in contact in non-covered areas. Some uncertainty remains for very thin intermediate layers, where e.g. electron tunneling effects in boundary friction may take place, too. However they are expected to exert a negligible error.

It was shown that the measurement was dependent on many influencing factors. The measured value was an indicator of the conductive part of A_r in direct contact to the steel counterbody's surface. While contact geometries, A_n, H_0, ρ_{el} and L_0 were expected to be sufficiently stable, the changes of μ and F_n can easily be obtained. The measured R in that case is only in relation to the direct, real contact area change due to a coverage and a separation caused by the intermediate layer or by changes of the specimen surface.

It must be noted that for all measurement techniques using electrical conductivity or dynamic thermocouple methods, a sufficient amount of conductive fillers must be used in order to reach the percolation threshold. Own, previous investigations showed that the applicability of the measurements was limited by a resistance starting at approximately 350 kΩ for a specimen placed in the test rig and measured by implemented multimeter.

4.1.2.2. Implementation

The implementation of the conductivity measurement technique was quite simple. R was measured in the resistance mode with an automatic range selection by a multimeter, type Fluke 8846a (Fluke Deutschland GmbH; Germany), using the internal "Average"-filter. The source voltage depends on the measurement range and varies between 6 and 13 V [266]. It was high enough to avoid possible disturbances by e.g. tribo-electrification and thermal effects. The measured signals were sent to the LabView-based data acquisition (DAQ) with a sample rate of approx. 1 sample/s and recorded in the test file together with other selected parameters. The data were only recorded in a specific channel if the resistance mode was active. The measurement was controlled by a programmable schedule. Therefore, it was active in desired test sections only. The basic setup of the test rig, regarding integration of conductivity measurement, is given in Figure 15.

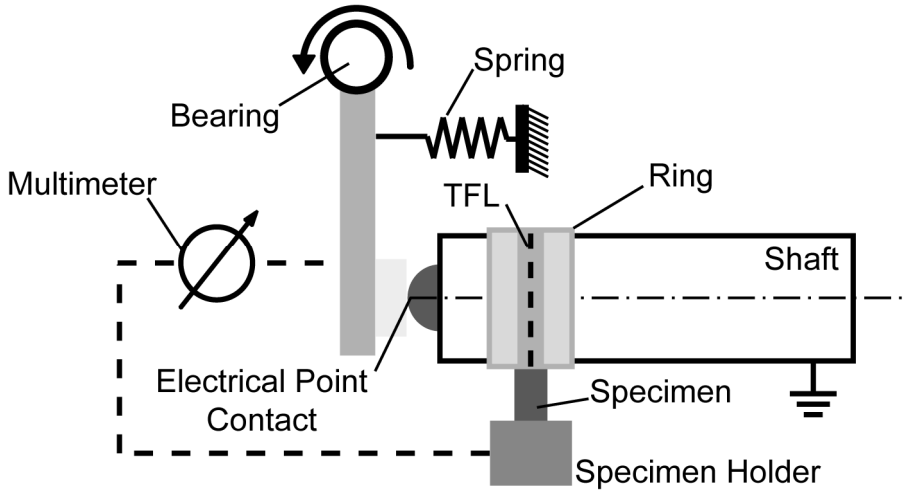

Figure 15: Implementation of conductivity measurement

The specimen holder consisted of stainless steel and was connected to the multimeter. It was electrically isolated from the rest of the test rig. In order to obtain a proper contact between specimen and holder, the specimens were polished on 3 sides to remove a possible injection molding skin and painted with argent finish G 3692 in the specimen holder contact area. The counterbody ring was from highly electrically conductive steel (100Cr6) and connected to a ball at the tip of the shaft. A stationary carbon brush was pressed against the rotating ball using a tension spring. The carbon brush itself was connected to the multimeter. The shaft obtained proper ground connections through the bearings and an additional slider.

4.2. Temperatures

4.2.1. Dynamic Thermocouple

4.2.1.1. Principle of Measurement

Several studies were found regarding the application of dynamic thermocouple measurement method on metals [190–194] but no publications were found for the use in combination with polymer compounds. The basic principle is based on the Seebeck-effect. This effect can be explained by a simple conductor as shown in Figure 16.

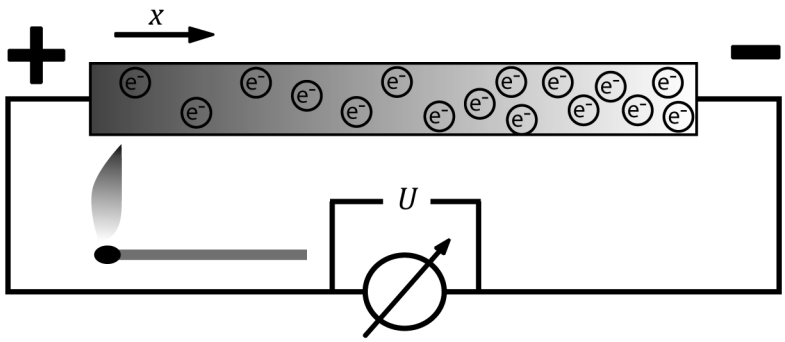

Figure 16: Seebeck-effect principle

If a thermal gradient is introduced to this conductor, electrons of a high energy level will move to the cold end of the conductor. This unbalanced distribution of electrons results in a measurable electrical potential [267]. This electrical field G is described by the thermal gradient $\frac{dT}{dx}$ and the Seebeck-coefficient S_c of the material:

Eq. 28: $$G = S_c \frac{dT}{dx}$$ [268]

The electrical potential U rises with increasing distance x across the conductor. Therefore it can be said:

Eq. 29: $$G = \frac{dU}{dx}$$ [268]

Eq. 30: $$\frac{dU}{dx} = S_c \frac{dT}{dx}$$ [268]

Eq. 31: $$dU = S_c dT$$ [268]

The following equation can be used for the calculation of the electrical potential of one conductor, which is dependent on the temperature difference within but not related to distance across the conductor:

Eq. 32: $$U = \int_{T_R}^{T_C} S_c dT$$ [268]

The Seebeck-coefficient is not a constant material characteristic, but it is more or less a function of temperature. The measurement of this potential cannot be performed as shown in Figure 16. This theoretical simplification neglects the fact that the connected wires for a measurement will obtain the temperatures at the contact areas. In doing so, they also influence the measurement through their own thermal gradients and Seebeck-effects. In view of this, Seebeck-coefficients are always measured in relation to another material with a known coefficient. To obtain the absolute Seebeck-coefficient values the Seebeck-coefficient of platinum, which is declared as reference, must be subtracted. The basic setup to determine the Seebeck-coefficient of a material is identical to the principle of a thermocouple measuring a temperature. For the determination of the Seebeck-coefficient of a material, all temperatures must be known, as well as the Seebeck-coefficient of the reference material. For the determination of the temperature of the junction T_C between the two materials all Seebeck-coefficients must be available and the reference temperature T_R. This reference temperature is the temperature at the other ends of the materials. A schematic principle of the measurement setup is given later in the first part of Figure 17.

For the calculation of T_C, a converted version of the following equation is commonly applied. It assumes the same T_C and T_R for both materials A and B and describes the relationship between overall measured voltage, thermal gradients and Seebeck-coefficients:

Eq. 33: $$U = (S_C^B - S_C^A) * (T_R - T_C)$$ [267]

To use this measurement technique in the field of tribology, the effects of tribo-electrification must be considered. Tribo-electrification is known from e.g. a balloon rubbed against hair. Doing so, an electrical charge is transferred due to contact potentials which cannot be leveled out after contacting since at least one of both materials is electrically isolating. However, if the contacting bodies show an electrical conductivity such effects do not take place. Only for the very specific case of large material transfer from the specimen to the counterbody or vice versa, resulting in a transfer of charge, this effect was reported in literature. Chiou et al. as well as Chang et al. carried out extensive tribo-electrification investigations under severe wear conditions for metals, with respect to the Seebeck-effect, using reciprocating sliding kinematics [191, 192, 194, 269]. They varied speed and load and found an appropriate solution to exclude tribo-electrification effects from Seebeck-voltages. They established that

tribo-electrification processes are not related to sliding speed. By extrapolation of the measured voltage at different sliding speed, which was gradually reduced to a complete stop, the voltage generated only by the tribo-electrification could be obtained [191]. For the effects of different loads an equation was proposed taking the RCA and wear rate into account. It was assumed that tribo-electrification has a linear correlation to normal load [192]. As a result of both approaches regarding the variation of sliding speed or load, the values of the tribo-electrification were obtained, allowing the separation of the voltages related to the Seebeck-effect. There are in general some uncertainties regarding the kind of temperature measured using dynamic thermocouple technique. Depending on the publication, this varies between average surface temperature [185], contact (flash) temperature [190] and a combination of both [193]. This is an important issue regarding the adaption of the measurement technique to the area of polymer tribology.

4.2.1.2. Experimental Phenomena and Physical Approach

The results of the pre-tests to this work were not usable since much higher voltages were measured in comparison to publications from Bowden and Ridler [190], Furey [193] or Chang et al. [191, 192, 194], although similar measurement method was applied. The resulting temperatures were unrealistically high, several tens of thousands degrees. They resulted of measured voltages of ~3 up to ~15 mV. Possible disturbances within the test rig, e.g. parasitic voltage, electrostatic charge or current leakage were eliminated, but comparably “high” voltages still remained. After excluding many possible origins of these measurement results, several physical aspects remained to be clarified. The influences of contact potentials in the measurement circuit, tribo-electrification and Seebeck-effect had to be clarified in regard to the sliding kinematics. Additionally, the inherent differences between metal-metal to polymer compound-metal contacts had to be taken into account as well as the anisotropic and inhomogeneous material characteristics of the polymer compound. The significant differences of electrical and thermal conductivity of polymer compounds in contrast to metals could also be of influence. According to Pelster [267] contact potentials can be neglected for temperature measurements based on the Seebeck-effect as they level out in a closed electrical circuit. Additionally the influence of temperature on contact potentials is small. Therefore they were excluded as a possible disturbance. Tribo-electrification due to material transfer was reported by Chang et al. to be in direct correlation towards wear and material transition [194]. In their studies the testing time is not clearly mentioned. According to their sliding speed of 40 mm/s and sliding distance of 0.6 m a testing time of about 15 s can be calculated [192]. In their publi-

cation, the effect of speed on Seebeck related voltage is obvious [191]. While their specimen, used on a reciprocating pin-on-slap experiment, has a similar dimension as the preliminary tests of this work, they report severe wear and material transition of at least 0.1 mg up to 14 mg depending on the material combination. According to their results a specific wear rate would be around $1.6*10^{-4}$ mm³/Nm. This wear rate is very high as they wanted to study severe wear. With such high wear rates they obtained a maximum peak of approximately 25 µV caused by tribo-electrification. Compared to a tribologically optimized polymer, with wear rates of e.g. $4*10^{-7}$ mm³/Nm [174], polymer wear rates are several decades smaller resulting in much lower possible charge transfer caused by wear and particle transition. Coulomb elementary charge per volume of polymer and metals is in comparable regions. Even if wear rate would show such high values, the resulting voltages would still be two decades smaller than actually measured voltages in experiments. It can therefore be concluded that a possible tribo-electrification can be neglected for the current investigations.

Since neither tribo-electrification nor contact potentials could deliver a reasonable explanation for the values measured and possible measurement disturbances were excluded, the question remained why such high voltages were present. Especially, as in other studies the basic equation was applied in comparably simple ways using static calibration for the dynamic thermocouple. A possible explanation of this was found during the mentioned pre-tests. The volumetric temperatures on the specimen and on the counterbody surfaces measured with an IR-camera varied extremely from each other. While the specimen was in a continuous sliding contact and a volume increment of the counterbody was only for milliseconds in sliding contact, this difference seems reasonable. Together with the distinctively different thermal conductivities of the polymer compound specimen and of the steel counterbody, this indicated the need for a closer analysis of the heat flux distribution, as it could have an important impact on the measurements. Resulting from these issues and physical conditions regarding the surface heating, the thermal gradients could have varied within specimen and counterbody, also. A theoretical model had to be established in dependence on the literature regarding theoretical and experimental studies of metal sliding pairs in combination with our own theoretical, experimental and simulative results in order to obtain a proper description of the thermal processes within the sliding contact. For the contact theory it could be assumed, that an ideal contact plane has the same temperature for both bodies in contact.

The Seebeck-effect is a volumetric effect and the temperature of a volumetric increment is not only dependent on the contact-side towards a counterbody. A couple of considerations lead to the following solution:

- According to own experiments a volumetric increment of the counterbody is in a sliding contact only for very short time fragment. Assuming a specimen surface size of 4 mm x 4 mm and the typical circumference of 188.4 mm for the counterbody, the aspect ratio of time inside and outside of the sliding contact is approximately 1:47.

- The contact time of a volumetric increment of the counterbody for 1 m/s sliding speed is 0.004 s. For an exemplarily CoF of 0.3 combined with a normal pressure of 1 MPa (=16 N for above mentioned specimen size), the total energy dissipated by friction during this contact time is 0.0192 J or $5.3*10^{-6}$ W/h. This energy is mostly dissipated by heat, resulting from adhesion, elastic and plastic deformations and fractures.

- The thermal conductivities of polymeric specimen and steel counterbody are extremely different. For the used PEEK-based tribo-compound (PEEK-TC) a thermal conductivity of 0.86 W/mK was determined. The thermal conductivity of 100Cr6 steel was taken from the literature with 42.6 W/mK [270]. The aspect ratio is approximately 1:50. While thermal conductivity is more uniformly distributed in the metal counterbody and the counterbody's heat sink, particles and fibers in the polymer-compound which have relatively high thermal conductivities are almost adiabatically isolated by polymer. The temperature distribution in the composite can be assumed to be less uniformly.

Summarizing, a volumetric element of the counterbody receives only a very small amount of energy during one complete turn. Most of this energy dissipates in the highly thermal conductive bulk material or to the environment by radiation. The polymeric specimen, however, is always in contact and has poor thermal conductivity. Different thermal gradients within the specimen and the counterbody, as they were observed within the pre-tests, seem therefore reasonable.

4.2.1.3. Theoretical Model and Course of Action

A model is proposed including the presence of separate thermal gradients of the contacting partners, Figure 17.

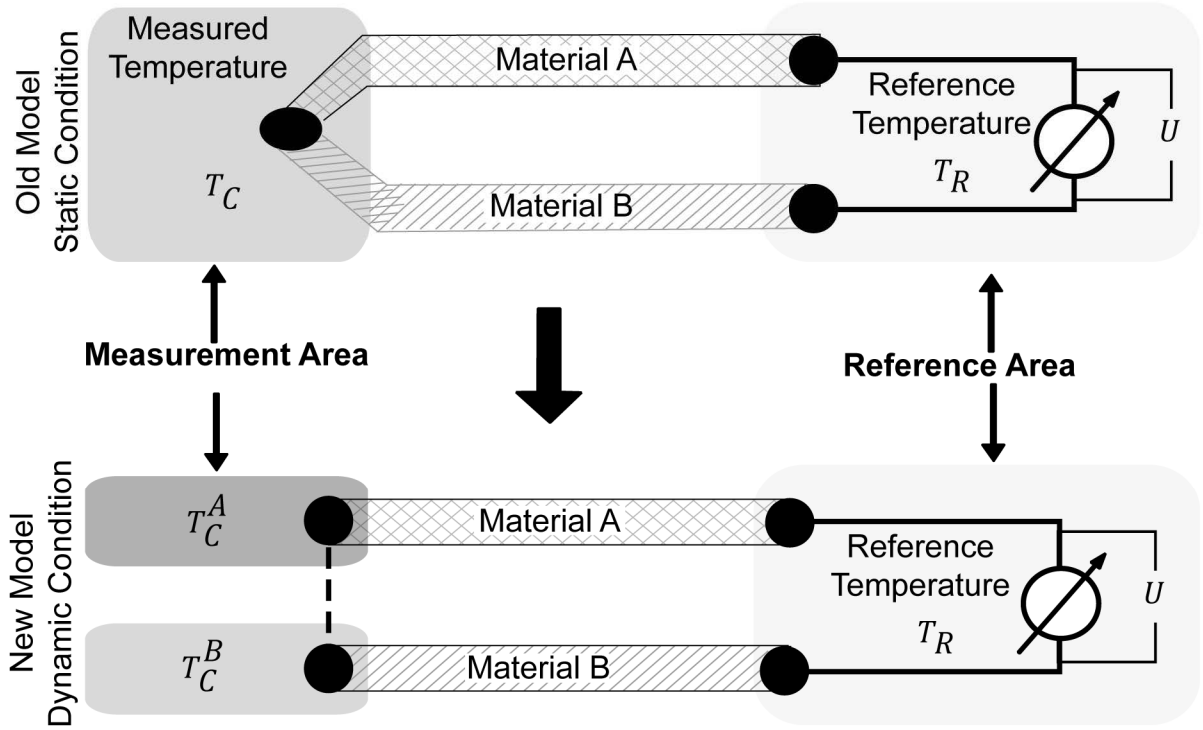

Figure 17: Modified calculation model

The equation introduced in section 4.2.1.1 for thermocouple temperature calculation was used in a modified manner. As indicated in Figure 17 it was extended by a separate T_C^A for the contact (= volume) temperature of the counterbody and T_C^B for the desired specimen volumetric contact temperature. T_R is the heat sink reference temperature of the specimen holder and the electrical connection at the cold end of the shaft. The calculation based on the proposed equation 34 requires the absolute Seebeck-coefficients of the used materials as a function of temperature. For static conditions this is not necessary and relative Seebeck coefficients can be used since total temperature differences between T_C and T_R are equal for both contacting materials. If different temperatures are expected according to the proposed model in Figure 17, the absolute coefficients must be used for each material. Seebeck-coefficients are dependent on the volumetric contact temperature of the materials. Therefore as lower integration border T_R = 0 K must be used because complete thermoelectricity of each material has to be considered. The modified equation uses the Seebeck-coefficient as a function of separate volumetric contact temperatures for each contact partner. For Material A, it is set to $S_C^A(T_C^A)$.

The complete equation is expressed as:

Eq. 34: $$U = \int_0^{T_C^A} S_C^A(T_C^A)dT - \int_0^{T_C^B} S_C^B(T_C^B)dT$$

The solved integral is written as:

Eq. 35: $$U = S_C^A(T_C^A) * T_C^A - S_C^B(T_C^B) * T_C^B$$

The Seebeck-coefficients are not always linear and may rapidly change if for example material structures change due to melting. For the used materials and the counterbody a relevant change in structure of the electrically conductive share was not expected within the achieved temperature range. The temperature related Seebeck-coefficients were approximated as linear functions $a * T_C^A + b$ for the material A and $c * T_C^B + d$ for the material B respectively. Therefore the equation may be written as:

Eq. 36: $$U = (a * T_C^A + b) * T_C^A - (c * T_C^B + d) * T_C^B$$

To obtain T_C^A some transpositions had to be done and a quadratic equation needed to be solved. The correct result of the quadratic equation is obvious as the incorrect result shows a negative absolute temperature. Finally T_C^A is obtained using:

Eq. 37: $$T_C^A = \frac{P - b}{2a}$$

$$P = \pm\sqrt{4a{T_C^B}^2 c + 4aT_C^B d + 4aU + b^2}$$

Both Seebeck-coefficients as a function of temperature from the polymer specimen S_C^P and also the counterbody S_C^C had to be determined in advance of the tests. This was done under static conditions and is described in the upcoming experimental section 5.1.2.7. For the counterbody this value had to be determined only once while it had to be established in detail for each polymer material. The Seebeck-coefficients are temperature related. Therefore a curve of the Seebeck-coefficient as a function of the ambient absolute temperature had to be measured and extrapolated. Copper was chosen as a reference material.

The modified theoretical model which depends on the thermal characteristics of polymer-steel sliding contacts was then introduced. Since the former assumption varies strongly from known literature and theories, a consistent course of action in order to obtain a proof of the model had to be conducted, Figure 18.

Pre-tests showed that **existing theoretical models in literature** do not match the present study, and experimental phenomena were not explainable by these models. Therefore the **theory of different thermal gradients** was established based on experimental observations and theoretical considerations. Furthermore, the equation introduced requires the volumetric contact temperature from the counterbody ring T_C^C. Experimental observations were necessary to show that within the relevant boundaries this temperature is similar to the bulk temperature of the counterbody ring. A **simulation** of the sliding contact had to give information about the heat distribution and the characteristics in sliding contacts in order to support that the use of the bulk temperature as volumetric contact temperature T_C^C of the counterbody ring is valid. For this matter, experimental data were required as input parameters and additional information obtained by e.g. DSC, DMTA etc. was necessary. An additional investigation, called "**contact experiment**" focused on the behavior of the Seebeck-effect based phenomena of suddenly contacting surfaces as function of heat fluxes between both solids. This was expected to lead to a better understanding as well as to demonstrate that the Seebeck-effect is dependent on volumetric temperatures, which are not fully evolved for infinitesimally small volumes and short time periods of occurrence.

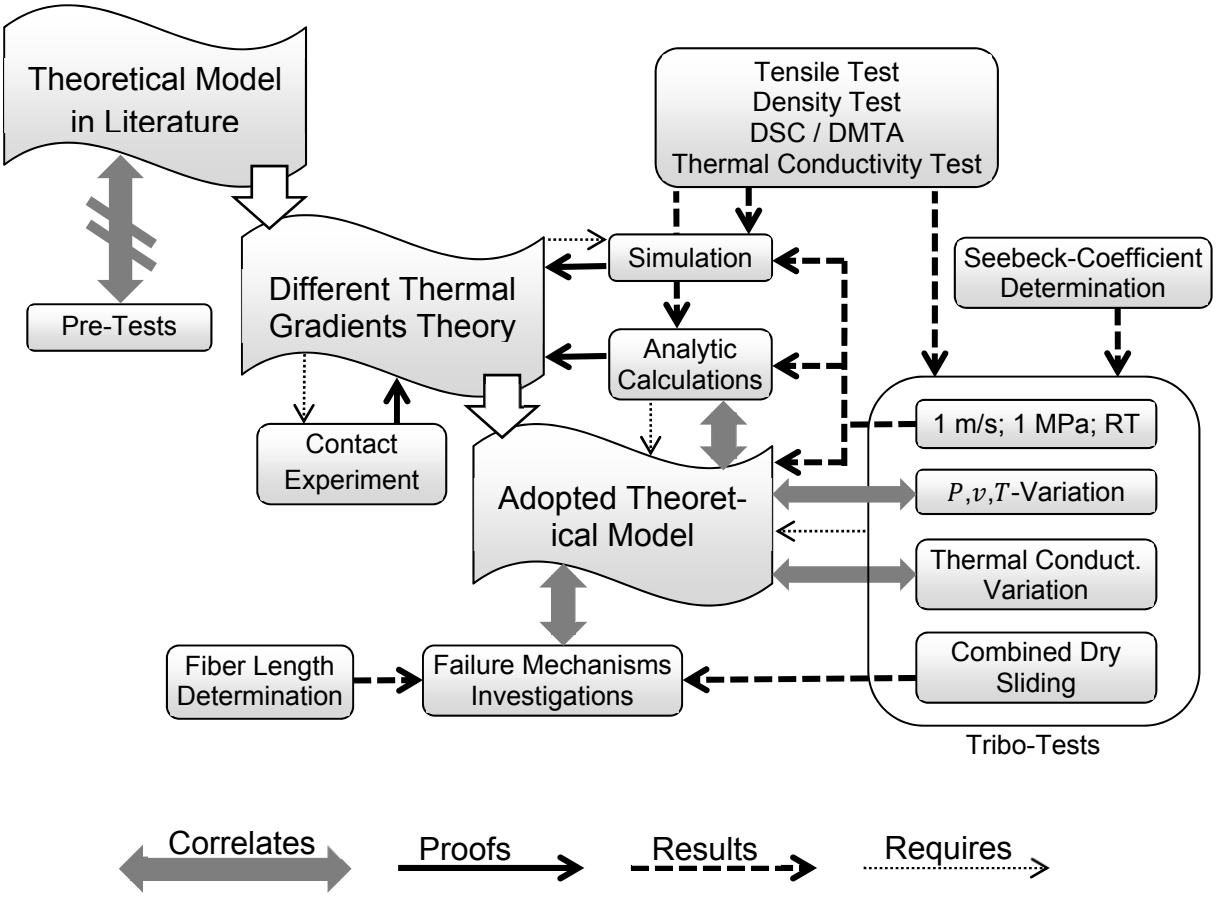

Figure 18: Course of action for validation of the modified theory

The **adopted theoretical model** delivered first results together with **tribology tests** using basic parameters, set to a sliding velocity of 1 m/s and a normal pressure of 1 MPa at room temperature (RT), and earlier **determined Seebeck-coefficients**. These results were to correlate with **analytic calculations** of the contact temperatures in order to prove the adopted model. Subsequently the proven model was used to analyze the tribo test series with variations in normal **p**ressure, sliding **v**elocity and counterbody **t**emperature. Additionally, the effect of **thermal conductivity variation** of the sliding materials was compared and correlated. Finally, **failure mechanisms investigations** were conducted. For these investigations **combined dry sliding** tests were required, applying all newly developed measurements in parallel. For theoretical considerations a **fiber length determination** was conducted in order to discuss heat distributions within the specimen.

4.2.1.4. Implementation

The hardware implementation of this measurement technique was identical to the in-situ electrical conductivity measurement of the sliding contact which is described in section 4.1.2.2. The only difference was that the Fluke 8846a multimeter was set to the V-metering mode instead of the Ohm-metering for the temperature measurement. In order to keep T_R constant, the specimen holder was temperature controlled using a water cooling system combined with an IR temperature sensor CT-CF22 (MICRO-EPSILON MESSTECHNIK GmbH & Co. KG; Germany), implemented with a PID control loop. The temperature control of the electrical connection of the shaft was realized in a similar way by using compressed air and a PT100 temperature sensor. For the purpose of a convenient post-processing of the measured voltages an additional measurement channel was created in the LabView environment. This additional channel records data exclusively if the Fluke multimeter was in the voltage measurement mode, allowing the alternating measurements, e.g. electrical conductivity, to be monitored during a combined test sequence as well.

4.2.2. IR-Camera

4.2.2.1. Principle of Measurement

The principle of temperature measurement using an IR camera was described in detail in [271]. It is based on Planck's radiation law which describes the correlation of surface temperature and emitted wavelength by illustrating the spectral energy density for a perfect full radiator. This allows the determination of a surface temperature if the spectral energy is known for a specific range of wavelengths. Usually sections

located in the longwave infrared radiation spectrum are used as they provide good accessibility with highest differences in spectral density. Using Stefan-Boltzmann law the total energy of a signal and thus the surface temperature can be obtained by integration [271, 272]. The emissivity of the measured surface must be taken into account for the measurement as it exerts a strong influence on the emitted and measured energy density. In Figure 19 total energy for 310 K is marked as grey area below the 310 K curve.

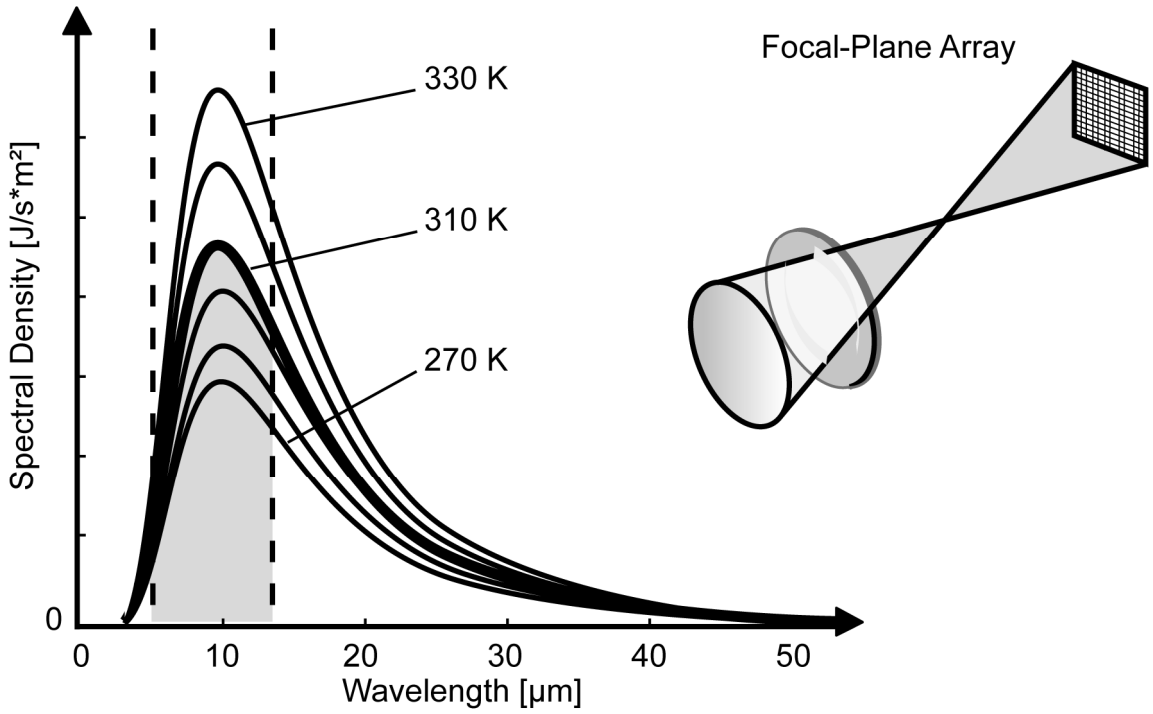

Figure 19: Spectral density over wavelength for IR-measurement [271]

In recent years focal plane arrays were established for wavelength and energy measurement [271]. Figure 19 shows the schematic of such an array consisting of multiple single infrared photo detectors. Although the optical focus has to be adjusted for such systems, even less expensive systems provide many advantages such as a high measurement rate of e.g. 120 Hz or reasonable resolutions like 382 x 288 pixels [272].

4.2.2.2. Implementation

The IR-camera thermoIMAGER TIM 160 (MICRO-EPSILON MESSTECHNIK GmbH & Co. KG; Germany) was implemented with special attention on minimum distance towards the specimen for highest local resolution. With the chosen optics and distance a resolution of ~0.1 mm/pixel was achieved while the camera was placed in a 45 ° angle towards the specimen. This way it was possible to watch two sides of a pin specimen, namely the side orthogonally towards the shaft's axis and the exit sur-

face where the counterbody leaves the contact area. This latter side was chosen as it was generally expected to obtain higher temperatures due to heating of the counterbody just after passing the sliding contact. The thermo-imager camera was connected to the LabView environment via USB using the necessary additional control software OPTRIS PI Connect (Optris GmbH; Germany). Refresh rate for data acquisition was 1 sample/s. The control software offers a setting of different measurement areas in specific measurement modes within these areas. Not only the average temperature within one measurement area but also the highest obtained value was given to the LabView DAQ. For the following tests two different modes were used. For the maximum temperature of the specimen only a large measurement area was set with highest temperature mode. When recording a whole temperature gradient of the specimen, 7 measurement areas in total were set. The initial specimen heights were approximately 3 mm. Therefore the height of one IR-measurement area was ~0.4 mm. If noticeable wear occurs, it could happen that the first measurement area was no longer on the specimen. This was clearly visible in the results and had to be considered in post-processing.

5. Experimental

5.1. Materials and Lubrication

5.1.1. Material Compositions and Production

PEEK-TC is a tribological optimized material, developed at IVW and meanwhile industrially adopted. For the purpose of this experiment, compounded PEEK-TC granulate was supplied by KS-Gleitlager GmbH. A detailed study on tribological performance for the PEEK-TC is given in the work of Oster et al. [273]. It is known that the polymer matrix material PEEK™ 450G (Victrex® Europa GmbH; Germany) is used. The exact type of the other fillers and manufacturers are still under non-disclosure intellectual property, similar to the extrusion parameters. The formulation as provided in the published patent is presented in Table 2.

Declaration	PEEK [wt.%]	TiO_2 [wt.%]	ZnS [wt.%]	Graphite [wt.%]	SCF [wt.%]
PEEK-TC	60	10	10	10	10

Table 2: PEEK TC composition

The granulate was injection molded to DIN EN ISO 527-2 type 1A dumbbell-shaped specimens, using an Allrounder 320 S (ARBURG GmbH + Co KG; Germany) injection molding machine. The injection molding speed was set to 45 mm/s with 1750 bar at a melting temperature of 420 °C while the tool temperature was 200 °C. Injection was followed by a cooling time of 30 s. Afterwards the specimen were dried at 130 °C for 4 h. As necessary, specimens were cut by using a circular saw Diadisc 5200 (MUTRONIC Präzisionsgerätebau GmbH & Co. KG; Germany).

Additionally to the compounded and injection molded polymer compounds, a PEEK based material with continuous fibers was used in the experiments. The continuous fibers provide large anisotropic differences regarding their thermal conductivity, which allows conclusions regarding thermal effects in sliding contact. The material is referenced as “XC-2”, it was produced by ICI Fiberite (USA) and has a total fiber volume content of 60% high tension PAN fibers, type AS-4 from Hercules Fibers® (USA) [42]. This material was also discussed by Flöck concerning experimental and simulative studies of sliding mechanisms [42]. The production parameters were not communicated. Concerning the specimen preparation, a solid 4 mm thick plate was used. Due to the strong anisotropic characteristics, the material declaration was set to XC-2-N, -P or -A for normal, parallel or axial fiber orientation in reference to sliding test direction or the shaft axis, respectively.

5.1.2. Material Properties and Physical Characteristics

5.1.2.1. Tensile Test

A tensile test regarding the reference-material PEEK-TC was performed in dependence to the DIN EN ISO 527-1 to -5, using a Zwick 1485 (Zwick Roell AG; Germany) universal testing machine equipped with a 250 kN load cell and a hydraulic clamp. DIN EN ISO 527-2 type 1A dumbbell-shaped specimens were used. The displacement was measured using a macro-displacement-transducer. The crosshead speed was set to 1 mm/min. The environmental temperature was set to RT, 100 °C and 200 °C while at every temperature at least 3 tests were conducted for confidence level. The E-modulus was calculated between 0.05 and 0.25 % strain.

5.1.2.2. Differential Scanning Calorimetry (DSC)

Glass-transition and melting temperatures were obtained according to the DIN EN ISO 11357 using a DSC 1 (Mettler-Toledo GmbH; Germany). The temperature ranges were set from RT to 400 °C for the PEEK based materials while the heating rate was 10 K/min. Concerning the specific thermal capacity c_p, the sapphire-method was executed by comparing the heat fluxes of the specimen and the reference material. The heat flux is direct proportional to specific thermal capacity c_p. Therefore, with a known c_p of the reference material, one obtains the specimen's c_p. Tests were conducted between -30 °C and 70 °C with a heating rate of 10 K/min.

5.1.2.3. Dynamic Mechanical Thermal Analysis (DMTA)

The influence of fiber orientation of the XC-2 material on the temperature related dynamic E-Modulus was investigated using a DMTA analysis. A temperature-sweep testing route was chosen in tensile test configuration. The testing machine was an EPLEXOR® 100 N (GABO QUALIMETER Testanlagen GmbH; Germany), modified with a 150 N load cell. A static pre-load was set to 20 N with dynamic load of 10 N within a temperature range from 23 up to 320 °C. The specimen's sizes were 2.4 mm x 50 mm x 9.8 mm. One specimen was prepared with the fiber orientation in direction of the load and for comparison another one with the fiber orientation orthogonal to the load direction. The distance between clamping fixtures was 30 mm and the heating rate was set to 2 K/min.

5.1.2.4. Thermal Conductivity

Concerning the thermal conductivity tests, PEEK-TC granulate was hot pressed (PM 300; Dr. Collin GmbH; Germany) and afterwards tested on a self-built test rig at Fachhochschule Kaiserslautern, Prof. Schuster. The following parameter sequences were applied in order to obtain good densities without void enclosures:

Step	Time [min]	Total Time [min]	Temperature [°C]	Pressure [MPa]
1	3	3	100	0
2	19	22	450	2
3	10	32	450	12
4	15	47	100	12
2 s ventilation after 22 and 32 min				

Table 3: Hot press parameters

Regarding XC-2 material in A and P fiber direction, a specimen was cut from the solid plate using the whole circle saw. Concerning N-orientation, several stripes were cut from the plate and glued together using Endfest 300 (UHU GmbH & Co KG; Germany). The thereby obtained plate was grounded in excessive work until desired round shape of the specimen with a 50 mm diameter at 5 mm thickness was obtained with polished tops and bottom sides. Less thickness in case of A and P fiber orientation was still acceptable for the test. Thermal conductivities of the materials were determined according to ASTM E1225-04, using a self-constructed measuring cell [274]. Specimens were tested with an inducted heat flux of approximately 1720 W/m² while setting a maximum heating temperature to 60 °C. Results were analyzed using a LabView based DAQ. Thermal conductivity was directly provided in W/mK. As for the confidence level, the tests were repeated three times and the averages as well as the standard deviations were calculated.

5.1.2.5. Static Electrical Conductivity

The determination of the electrical resistance R of PEEK-TC was conducted based on a 4-point measurement method described in DIN EN ISO 3915. A 2601A electrometer (Keithley Instruments GmbH; Germany) was used for this measurement. The samples were obtained from DIN EN ISO 527-2 type 1A dumbbell-shaped specimen from the middle section to avoid uncertainties of fiber orientation due to injection molding. All specimens were cut and tested comparable to the following tribological tests regarding electrical flow and orientation. To avoid a disturbing influence by the injection molding's skin, all contacting surfaces were polished using grade 800 abrasive papers and painted with argent finish G3692 subsequently, to contact all possibly conductive fillers on the specific surface when using two measurement tips

on each side. According to DIN EN ISO 3915 [275] a maximum of 0.1 W should be applied to the specimen, which limits the possible current to 0.02 A for a 5 V measurement voltage. The resistance was measured in ohm [Ω] and the exact dimensions of the specimen were measured using a digital caliber. Concerning the confidence level, 10 specimens were investigated for each dimension and subsequently the average as well as the standard deviation calculated.

It was intended to give the average resistance R to several specimen surface dimensions while keeping specimens length constant in order to proof the theoretical dependencies. In section 4.1.2.1, the theoretical relationships between geometrical aspects and electrical resistance are explained in detail. The desired dimension in reference to the length of the specimen was 9.7 mm and regarding the thickness was 4 mm. The width of PEEK-TC varied between 5, 10, 15 and 25 mm. XC-2 was tested with 5 mm width only.

5.1.2.6. Density

Densities of the materials were measured according to the Archimedes principle. At least three specimens of approximately 4 mm x 4 mm x 10 mm size were measured for each material. Size determination was conducted using a digital caliber and weight determination using a DV-214C scale (ItinScale Co., Inc.; USA).

5.1.2.7. Seebeck-Coefficients

For the dynamic thermocouple measurement method, the Seebeck-coefficients of the materials must be known and a static reference measurement for the tribology test rig must be conducted as well. The separate determination with external measurement equipment to determine the material's Seebeck-coefficient was proofed by some pretests to be more stable. The measurement setup was based on a multimeter to measure the voltage, a cartridge heater, large heat capacity metal blocks and a reference material. As a reference material copper wire was found to be suitable as Seebeck-coefficient is well known from the literature [276] and the material was readily available in a pristine way. The schematic of the test setup was identical to the former introduced thermocouple principle in section 4.2.1.1. The multimeter was a type 8808A (Fluke Deutschland GmbH; Germany). The cartridge heating system Z124/1/16/W (HASCO Hasenclever GmbH + Co KG; Germany) provides a control loop for temperature controls using a PT100 thermocouple. To determine PEEK-TC as well as XC-2 Seebeck coefficients, both materials were tested and the voltage at several temperatures was measured. Temperatures were chosen between RT and

glass transition temperature of the materials. The Seebeck-coefficient was calculated according to following equation [267]:

Eq. 38: $$S_C^P = \frac{U - S_C^{AL} * (T_R - T_C)}{(T_R - T_C)}$$ Based on:[267]

U is the overall measured voltage while S_C^P and S_C^{AL} are Seebeck-coefficients of the polymer or copper wire, respectively. T_C is the temperature of the junction between both materials while T_R is the reference sink temperature at the other end of both materials (compare section 4.2.1.3). The equation is based on the thermocouple-equation from [267]. More information about the Seebeck-theory and basic principle is described in section 4.2.1.1. According to the Seebeck-theory the specimen size is not relevant. Therefore, a middle section of the PEEK-TC referring to the DIN EN ISO 527-2 type 1A dumbbell-shaped specimen was cut out with a size of 10 mm x 3.7 mm x 80 mm while samples with approximately 4.3 mm x 4 mm x 52 mm were prepared from XC-2 material. Regarding all contacting areas, the injection molding's skin and surface resin were removed using grade 800 abrasive papers. Additionally, in case of PEEK-TC, an argent finish G3692 was applied due to the poor electrical surface connectivity to the metal. Since the film thickness of the paint was thin, no influence on the measurement occurred. Aluminum blocks were used as heat sinks for a constant T_R. The thermal conductivity of the copper wire and all tested specimens were proofed to be low enough and did not result in any notable disturbance regarding T_R.

The Seebeck coefficient of the tribology test rig was determined in a similar way, using the inductive heating system to heat the shaft from RT up to 200 °C. The specimen was exchanged by a copper wire for this determination. In this setup T_C is seen at the connection of the counterbody ring with the copper wire while the specimen holder was connected to the other end of the copper wire and provides the temperature T_R.

Seebeck coefficients are temperature related. A curve of Seebeck coefficient as a function of absolute temperature was determined for each material and the test rig. In order to obtain the absolute Seebeck coefficient values, the Seebeck coefficient of platinum had to be subtracted. The absolute Seebeck coefficients of copper are available in [276].

5.1.2.8. Determination of Fiber Length

For theoretical considerations and analysis, a mean fiber length for PEEK-TC material was needed. In order to separate fibers from the matrix material, some PEEK-TC was combusted using an oven, Microwave Furnace (PHOENIX INTERNATIONAL, INC; USA), at 600 °C over a period of 45 min. Once it was cooled down to RT, the sample was investigated using an OM. Seven overview pictures were evaluated with more than 500 measurable fibers in total.

5.1.3. Lubrication

Concerning lubrication, a standard engine-oil for the use in combustions engines CS-M1 (FUCHS EUROPE SCHMIERSTOFFE GMBH; Germany) was selected. The density of the oil was 0.882 g/cm³ at 15 °C according to DIN 51757 and the burning point was 225 °C according to DIN ISO 2592. The viscosity of the oil was measured according to DIN 51398 and DIN 51562 and is given in the following:

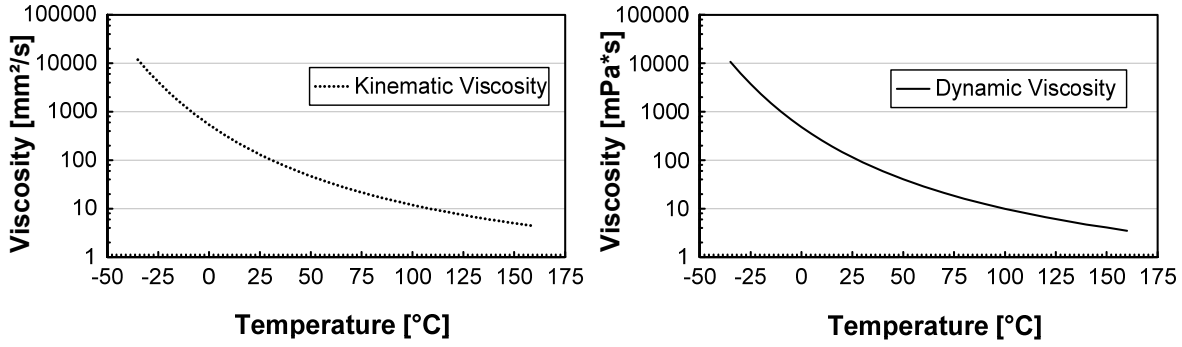

Figure 20: Viscosities of CS-M1 as a function of temperature

5.1.4. Counterbody for Tribological Tests

The counterbody rings used for tribological tests were the inner cylinders of roller bearings, made from 100Cr6 steel. They obtain by factory a surface roughness R_a of ~0.3 µm and R_z of ~1.7 µm and a surface hardness of 60-64 HRC. Their dimensions are 60 mm in diameter and 25 mm width with a wall thickness of 5 mm.

5.2. Morphological Analysis

5.2.1. Optical Microscopy

An optical microscope, type ARISTOMET (Esselte Leitz GmbH & Co KG; Germany), was used to investigate worn pin surfaces and surface cuts after tribological exposure and for the fiber length determination of the combusted material as well. This microscope supports magnifications from 25 to 500. Image capturing as well as data analysis were conducted using the analSYS Docu 5 software (Olympus Deutschland GmbH; Germany).

5.2.2. Scanning Electron Microscopy

Investigations of the TFL development on steel counterbody rings during a tribological exposure were also conducted using a Supra^{TM} 40VP SEM (Carl Zeiss SMT AG, Germany). Thanks to the high quality imaging possibilities provided by the SEM, qualitative correlations towards the TFL in-situ measurement could be conducted.

5.2.3. White-Light Profilometry

A white light profilometer MicroProf® 100 (FRT, Fries Research & Technology GmbH; Germany) was used for TFL investigations. In contrast to an OM and a SEM, it provides accurate quantitative results regarding surface topography. A sensor of 300 µm measurement range , a CWL 300, with a resolution of 3 nm [277] was applied. Inconsistent declarations were perceived regarding measurement technology of the sensor. Several manufacturers seem to report different descriptions of the same physical principle. The CWL 300 datasheet explanation indicates the same principle as the one in use by the confocal distance sensors. A detailed description of this physical principle is introduced in section 4.1.1.1 as it was one of the selected in-situ measurement techniques. This is especially interesting as in-situ and ex-situ measurements were provided with the same physical principle in order to be comparable in further stages of the experiments. The lateral resolution of the white light profilometer (WLP) was available with up to 1 µm [177]. Scans were conducted with a sufficient resolution of 3 µm in an area of 6 mm x 0.5 mm. Concerning post-processing data analysis software FRT Mark III, version 3.9.13.4 was used.

5.3. Simulations

In order to analyze and understand the temperatures within the sliding contact, a simulation model must be set up. FEM simulations are suitable. The simulation was conducted implicit on Abaqus CAE 6.12 (Dassault Systèmes; France) and addressed

the heat dissipation ratio towards sliding specimen and counterbody. From experiments, using the IR-camera, it was already obvious that the volume temperatures of the specimen and the counterbody ring must be distinctly different. The simulation setup consisted of a rotating disc, which was in contact with a specimen. Regarding a simplified simulation, a flat disc was chosen instead of a ring. The simulation was conducted with elements allowing coupled temperature and displacement. The E-modulus of the PEEK-TC compound specimen, its density, thermal conductivity and capacity were obtained from experiments (results given in 6.1.1) while material properties of the 100Cr6 counterbody are average values from literature [270, 278]. The Poisson ratio of PEEK-TC is given in the work of Oster [279]. Input parameters obtained from tribology tests regarding the friction coefficient, the normal load (1 MPa), the sliding velocity (1 m/s) and (for reference) the volume temperature of the specimen as well as the volume temperature of the counterbody were implemented, too. Table 4 contains all input data.

Parameter	Counterbody	Specimen	Unit
Size	Inner dia.: 32 Outer dia.: 82 Thickness: 5	Width: 4 Length: 4 Height: 15	[mm]
Density	7710	1650	[kg/m³]
Thermal Conductivity	44.6	0.86	[W/(m*K)]
Thermal Capacity	472.5	964	[J/(kg*K)]
E-Modulus	210	14.1	[GPa]
Poisson Ratio	0.3	0.35	[1]

Table 4: Simulation input parameters

The main focus of this simulation was on thermal effects for one mesh-increment of the counterbody ring's rotation trough the sliding contact area. A heating of this increment was expected during contact, while afterwards, a cooling process takes place due to the lower counterbody volume temperature and its high thermal conductivity. With increasing number of contacts for this increment over a given period of time, a rise of the average surface temperature of the sliding trace and nearby areas should take place. The specimen will show a different behavior since it is in a permanent sliding contact. The aspect ratio of contact surfaces as well as the difference of thermal conductivities is actually large. Irrelevant heat-related effects such as surface convection were neglected. Furthermore, the thermal capacities and heat fluxes of specimen holder and counterbody were disregarded. Both bodies in sliding contact were modeled as half-infinite. With regard to the computational time, the sliding time observed was limited to several turns, starting from room temperature to observe

evolving temperature gradients. A total of 4000 time increments of 0.00047 s length were set, resulting in a total sliding time of ~1.89 s. Specimen's mesh sizes were set with an increasing density towards sliding contact manually. For the counterbody ring they were set with sufficient density using an automatic meshing tool. The simulation did not consider the real contact area and used the nominal contact area with regard to the hertzian pressure. Regarding this, small peaks in the heating process are not obtainable and the rise of the maximum temperature during one contact phase can be under-estimated. The heat distribution of the frictional generated thermal energy was set to a ratio proportional to the thermal conductivities of both contacting partners. Additionally a variation in size of contact area was investigated. The specimen contact area was sized down to only 1/100 of its original contact size. The specific mass was adapted accordingly to provide more realistic heat flux conditions within the down-sized specimen. Focus of this additional simulation was on the effect that a much smaller contact area exerts on the heating of the counterbody ring.

5.4. Tribology Test Rig

A totally new test rig was developed at the IVW for sophisticated test requirements and enhanced measurement techniques. The basic principle follows the Block-on-Ring (BoR) and Plate-on-Ring (PoR) principles. The test rig was based on a stable granite plate with a weight of approximately 550 kg for vibration isolation. The increased mass results in a very low, non-disturbing resonance frequency. It was covered with a housing made of acrylic glass. The data acquisition unit ILC 150 ETH (PHOENIX CONTACT Deutschland GmbH; Germany) and test rig regulation, which contains servo controllers IndraDrive C (Bosch Rexroth AG; Germany), were placed in an electrical control cabinet. Due to size limitation, it was placed outside the test rig. A servo motor kit, MSS102F-0300 (Bosch Rexroth AG; Germany), was implemented without any gear. It allowed a wide range of sliding velocities with a torque which was strong enough even for larger specimens. This choice allowed the positioning and the reciprocating movement of the shaft. The use of a counterbody ring with 60 mm diameter allowed a setup achieving a maximum sliding speed of 25 m/s with a 12 Nm torque. Also, a very low speed in continuous movement, down to 0.0001 m/s, was possible with this configuration. For low sliding velocities up to 5 m/s the torque can be up to 36 Nm. The test rig appeared to be sufficiently powered for any realistic polymer compound test condition, even with high normal load up to the maximum possible 5 kN.

Regarding a stick-slip free behavior, a normal load was applied by a pneumatic air bag, lifting the linear axis which supports the specimen holder. The linear axis itself

was fixed using completely stick-slip free torque springs. That allows an easy substitution of specimens as well as the synchronization with the main axis. Doing so, a combination of sliding and rolling for reciprocating behavior can be set. In order to heat the counterbody to desired temperatures, an inductive heating system, Power Cube 32/400 (LTB Bachofer GmbH & Co. KG; Germany), with maximum power of 5 kW was applied, allowing fast changes in the counterbody temperature. A control loop of the temperature regulation was realized by using a spot-pyrometer CT-22 (MICRO-EPSILON MESSTECHNIK GmbH & Co. KG; Germany), which observes a blackened surface near the counterbody ring. The additional temperature control loops, necessary for specimen holder and electrical connection at the shaft, were realized using a similar spot-pyrometer concerning the specimen holder and a PT100 thermocouple concerning the electrical connection. The specimen holder was cooled by water, connected to the same circular flow like the inductive heater and the servo motor. The electrical connection at the shaft could be sufficiently cooled by inserting an air flow with approximately 6 bar. The compressed air was also used to apply the normal load and internal cooling of the main shaft. This was realized using co-axial air flow inserted at the back end, flowing to the front and exhausting at the back end again. Small amounts of lubricant, starting with several µl/h, were realized using a syringe pump station Legato 210 (KD Scientific Inc.; USA). The maximum capacity was limited to two 60 ml syringes, which can also be drained within several minutes. In order to use larger amounts of the lubricants, a circulation system using a hydraulic pump was implemented. The specimen holders for the plate or the block specimen were placed on a 3-axis strain gauge load cell, a K3D120 (ME-Meßsysteme GmbH; Germany), with custom made load ranges. Depending on the load, the measuring system could be exchanged to obtain high resolution at small forces or to cover a wide range of higher forces up to 5 kN. Wear was determined using an Eddy-current sensor ECL202 with probe U12 (IBS Precision Engineering Deutschland GmbH; Germany), attached to the specimen holder facing an aluminium ring on the shaft. Since ferromagnetic materials would interfere the inductive field at higher velocities, only non-ferromagnetic material can be used here. For observation of the temperature, an IR-camera, type thermoIMAGER TIM 160 (MICRO-EPSILON MESSTECHNIK GmbH & Co. KG; Germany), was integrated. Together with the enhanced measurements, a total amount of more than 40 measurement channels was provided. The control and data acquisition were executed with a custom LabView environment. The data input rate varied depending on the devices but the storage rate was typically set to 1/s. An overview of the whole test rig is displayed in Figure 21.

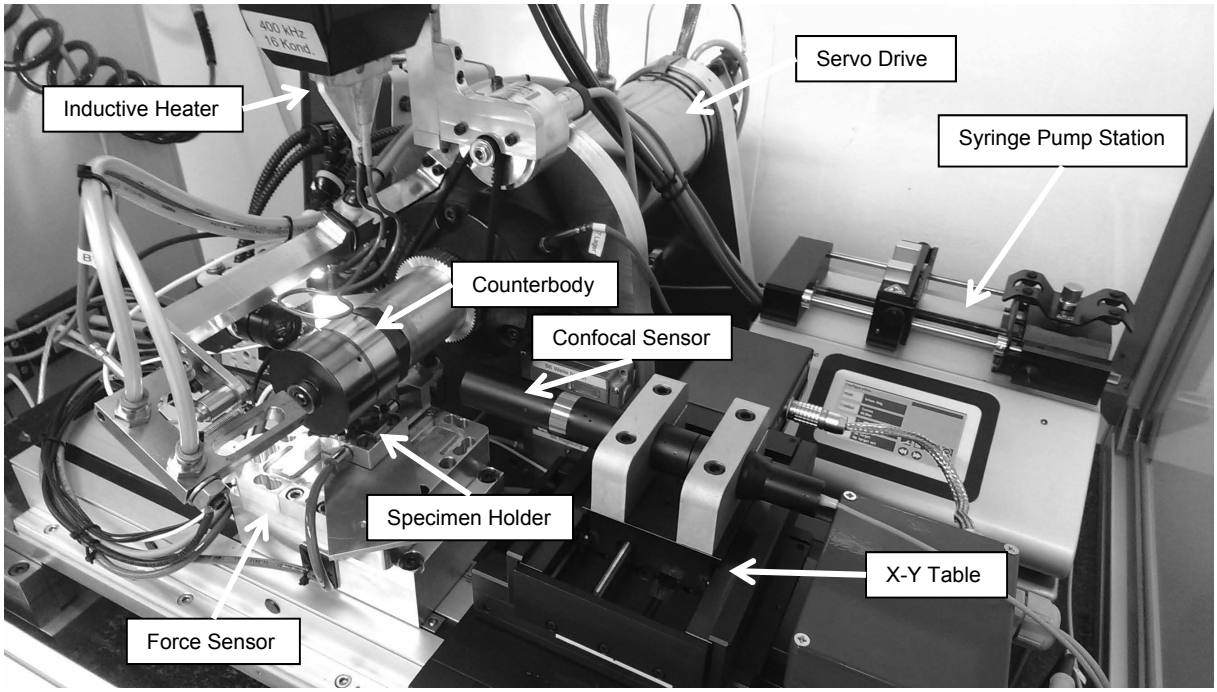

Figure 21: Test rig overview

A programmable scheduling of the tests had to be conducted, especially as many special functionalities were integrated. A simple example for a programmable scheduling is a pure combination of different load cases, where a normal load shall be changed every hour to another value. Nevertheless, the enhanced measurements as well as the longer and combined tests required additional possibilities. As a switch condition or as another criterion, a total time, a stable CoF or a limit of wear could be selected. Movement-, load- and lubrication conditions could be set individually for each step. The behavior of the Fluke 8846a regarding measurement mode could be set too, while another drop-down menu for special actions contained calibration and enhanced measurement related possibilities. It must be noted that depending on the applied measurements, necessary calibration actions had to be considered before activating the measurements themselves. Even for a simple CoF and a wear rate determination, for each load case force sensors and the Eddy-current sensor had to be calibrated to eliminate temperature and long-time drifts. In order to eliminate unnecessary data acquisition, only scheduled steps with selected measurement channels were recorded. Recording was executed continuously in a .tdms file, which was post-processed for a report using DIADEM 2013 (National Instruments Germany GmbH; Germany) software. Additionally, a section for each scheduled step was created in the .tdms file containing average values of all active measurement channels over the last 10 minutes (adjustable), applied for a fast and convenient reporting process. In the methodology overview (Figure 12) “additional visualization” was mentioned. This refers to an optical USB-camera which was implemented to use it within

dry sliding tests. The UI-1490LE-C-HQ camera (Imaging Development Systems GmbH IDS; Germany) was focused on the counterbody ring to observe the evolving TFL. After each load case, three pictures from different positions of the counterbody ring could be taken. The whole process was implemented in the main LabView test environment and conducts automatically when activated. With this feature, besides the TFL thickness measurement, an optical impression of the evolving and changing TFL could be obtained.

5.5. Validation of Measurement Techniques

The measurement methods, which were implemented in the tribology test rig had to be validated concerning their accuracy and functionality. The experimental routes varied depending on the measured parameters. Additional analytical investigations, basic theoretical correlations and FEM simulations, are possible. For all in common, a subsequent investigation of the measured sliding characteristics regarding changes caused by variation in load conditions was conducted. The measured changes should be in accordance to theory and therefore offer another verification of the measurements themselves. The combination of the described measurement techniques should offer a deeper knowledge of correlations within the tribological system.

5.5.1. Validation of Dry Sliding RCA and TFL-Thickness Measurement

The contacting surface area is an important influential factor concerning the electrical conductivity between two solids. In order to figure out the effect of normal pressure, when a polymer is pressed against a steel counterbody, an additional conductivity test was created and conducted. This test was prerequisite concerning the upcoming measurement validation techniques regarding the usage of resistive electrical conductivity measurements in order to determine the RCA. The investigation was conducted within the tribology test rig, using an identical setup to dry sliding tests in reference with the measurement theory described in 4.1.2. It should be mentioned that the polymer specimen was ground in shape within the test rig using a sand blasted counterbody ring. For the test itself, a standard counterbody ring was used. This procedure was also applied for all specimens for the upcoming BoR sliding tests. Surface characteristics of these standard rings were also determined using a WLP, and the results are given in section 6.2.1.3. During the tests, the specimen was driven towards to the counterbody ring with an increasing pressure until a normal force of 200 N was reached. This corresponds to a normal pressure of ~12 MPa for the specimens used. The force and electrical resistance through the specimen-counterbody contact were recorded. The counterbody was fixed in this scenario and the tempera-

ture was kept at RT. The test was repeated for four times, the average values were calculated. The parameters for tribological TFL/RCA experiments are given in Table 5. An obvious temperature influence on the TFL measurement using the confocal sensor was expected. Therefore, two reference tests without specimens were conducted with changing temperatures of the counterbody, using the inductive heating system. First, the test was conducted applying a permanent scan. A second test uses temperature-compensation with reference-algorithm as described in 4.1.1.1. The post processing of this data provides a standard deviation of the measurement method and a hint regarding possible resolution.

Specimen Material	Counterb. Roughness R_a [µm]	Normal Pressure [MPa]	Sliding Speed [m/s]	Counterb. Temp. [°C]	Step Time [hh:mm]	SEM / WLP	Confocal Mode
None	Normal	-	1	RT/50/100	00:55		Con.
None	Normal	-	1	RT/50/100	00:55		Ref.
PEEK-TC	Normal	1	1	RT	07:00	X	Ref.
PEEK-TC	Glass	1	1	RT	07:00	X	Ref.
PEEK-TC	Sand	1	1	RT	07:00	X	Ref.
PEEK-TC	Normal	1/5/10	1	RT	04:00 02:00 02:00		Ref.
PEEK-TC	Normal	1	1/3/5	RT	04:00 02:00 02:00		Ref.
PEEK-TC	Normal	1	1	50/100/150	04:00 02:00 02:00		Ref.

Table 5: TFL validation tests

As a TFL remains on the counterbody after tribological tests, subsequently SEM and WLP analysis can be conducted providing a direct comparison to the in-situ measurements. In order to enforce different TFL thicknesses without changing the used PEEK-TC reference-material, different sand- and glass-blasted counterbody rings were applied to provide different surface roughnesses. The surface roughnesses of the rings were determined using a WLP. Regarding the test schedules, room temperature (RT) describes a non-controlled state in which frictional heating itself determines the counterbody temperature. In order to add a static conductivity reference, each specimen was pressed against the counterbody for 30 s with 100 N. A reference scan sequence for the confocal measurement was added, because it was needed concerning the absolute TFL height determination. To determine this refer-

ence, the test rig was driven with 1 m/s sliding speed for 30 min at RT, applying only alternating confocal measurement. Additionally, forces were calibrated prior to the tests. All references were obtained automatically using the test rig's programmable scheduling capabilities. These references were collected prior to each test except for the non-specimen tests. Testing time was set sufficiently to reach a steady state behavior with stable transfer films depending on the counterbody surface roughness. In combined load cases, the relative change of measured parameters was interesting. Therefore, the testing time was shortened if reasonable. Specimens were prepared in block shape with an approximate size of 4 mm x 4 mm x 12 mm. The sizes varied in a range of ±0.2 mm, which were measured and considered for calculation of normal pressures. The orientation of the specimens regarding their fibers was declared as parallel in case their fibers were orientated in sliding direction. Normally orientated fibers were facing the counterbody. Axial was declared for specimen with fibers parallel to the shaft axis of the counterbody. Specimen holder contacting surfaces were painted with argent finish G3692 for proper electrical contact.

5.5.2. Validation of Lubricated Sliding RCA and LFT Measurement

In contrast to the TFL, the measurement of LFT cannot be validated by subsequent measurements. While a confocal sensor provides absolute values, it can give inaccurate results due to the oil film thickness outside of the sliding contact. A more promising approach could be the electrical conductivity measurement for RCA determination, but it comes with some limitations. It only yields relative changes and it is related to both, thickness of LFT and coverage of the counterbody by the lubricant. In order to confirm the relative or absolute values or changes, provided by both measurement techniques, a comparison to the CoF under aspects of Stribeck curve shall be performed. LFT has, according to Stribeck, a direct relation to the friction coefficient. This can give a correlation towards the following measurements. A special point of interest was the onset point of EHD sliding. This onset point was analytically determined and compared with results of CoF and new measurement methods.

Specimen Material	Normal Force [N]	Sliding Speed [m/s]	Counterb. Temp. [°C]	Oil Flow Rate [ml/h]	Step Time [hh:mm]
PEEK-TC	200	0.1	RT	50	01:00
PEEK-TC	200/400/ 600	0.1	RT	50	00:20
PEEK-TC	200	0.001/0.002/ 0.003/0.004/ 0.005/0.006/ 0.007/0.008/ 0.009/0.01/0.02/ 0.03/0.04/0.05/ 0.06/0.07/0.08/ 0.09/0.1/0.2/0.3/ 0.4/0.5/0.6/0.7/ 0.8/0.9/1/2	RT	v<0.06 [m/s]: 25 [ml/h] v<0.1 [m/s]: 50 [ml/h] v≥0.1 [m/s]: 150 [ml/h]	00:01
PEEK-TC	200	0.05/0.06/0.07/ 0.08/0.09/0.1/ 0.2/0.3/0.4/0.5/ 0.6/0.7/0.8/0.9/ 1/2	50/75/100	v<0.1 [m/s]: 50 [ml/h] v≥0.1 [m/s]: 150 [ml/h]	00:01

Table 6: LFT validation tests

In order to correlate results with the Stribeck curve, a logarithmic velocity-variation was conducted. For temperature variation, a velocity variation was pursued multiple times, once for each temperature condition but all within a single test. The velocity can be changed easily on a logarithmic scale and temperature variation exerts on oil viscosity shows logarithmic changes as well. The pressure cannot be changed in such high scale easily. In order to observe the influence of normal pressure, a simple variation of pressure at stable conditions was conducted. The oil flow rate was adapted to sliding speeds in a way, that consistent lubrication was surrounding the sliding contact. To keep the oil-pollution of the test rig as small as possible, the syringe pump station was used with a needle near the sliding contact, injecting the oil. A test with identical conditions was also conducted to investigate the stability of the measurement over a longer period of time. A reference of the electrical conductivity was obtained by applying 200 N normal force for approximately 60 s. Confocal reference algorithm was not not feasible due to lubrication pollution. A calibration of force sensors was done prior to the tests, too. Concerning lubricated sliding experiments, plates cut from the dumbbell-shaped specimens were used for tribological investigations. This shape provides more stable lubrication conditions in contrast to BoR tests. All injection molding skins of the specimens were removed using grade 800 abrasive papers. The area of contact between specimen towards specimen holder was painted with argent finish G3692.

5.5.3. Validation of Dry Sliding Temperature Measurement

In order to clarify the influence of the transient heat flux of suddenly contacting bodies, a simplified experiment was carried out first. This experiment was intended to clarify the behavior of heat fluxes on Seebeck voltage as a function of time. On a Zwick 1474 (Zwick Roell AG; Germany) universal testing machine, a massive block made from 100Cr6 steel was positioned on the lower traverse. This block with dimensions of 50 mm diameter and 70 mm height was large enough to provide a thermal capacity widely exceeding the ones from the specimens used. Test specimens were cut from type 1A dumbbell shaped specimen or block material, providing a contact surface to the 100Cr6 block of approximately 4 mm x 10 mm. The temperature of the 100Cr6 block was controlled using a heating plate and connected to the data acquisition system HBM MX840 (Hottinger Baldwin Messtechnik GmbH; Germany), via enameled copper wire. The copper wire was chosen as it provides known and constant influence on Seebeck-effect related voltages. The other multimeter connector was attached to the specimen, which itself was placed in the pneumatic clamps on the upper traverse. In order to isolate one of both contacting partners, the 100Cr6 steel block together with the heating plate was placed on an electrically non-conductive polymer plate. The test itself was monitored by the DAQ system, which records both, the voltage generated by the Seebeck-effect from the two contact partners and the force signal given by an analog output of the universal testing machine. Additionally, an IR-camera thermoIMAGER TIM 160 (MICRO-EPSILON MESSTECHNIK GmbH & Co. KG; Germany) was attached to record the specimen's maximum temperature. The different specimen materials and conditions were chosen under following objectives:

- PEEK-TC: This material was used as reference for all measurement technologies and for the contact simulations as well. Of great interest was the behavior at initial contact towards a contact partner with largely different temperature and thermal conductivity. The analysis was conducted with a 100Cr6 block temperature of 100 °C. Concerning PEEK-TC, the influence of another temperature was additionally investigated using 160 °C on the 100Cr6 block.

- 100Cr6: Concerning identical materials, no Seebeck-effect related voltage should occur after the temperature in the contact area was leveled. This combination clarifies initial contact phenomena without the influence of different material characteristics.

- Copper: Copper obtains a very high thermal conductivity. Therefore results should be in contrast to materials with worse thermal conductivity, e.g. PEEK-TC.

- XC-2: It was used with normal orientated fibers against a 100Cr6 block. XC-2 provides huge differences in thermal conductivity for normal or parallel/axial fiber orientations. So it was a good candidate material for investigating the influence of thermal conductivities for later tribological experiments. Regarding the dynamic contact experiment, it provides a very high axial thermal conductivity among the fibers, which are of a small mass and embedded in bulk material with a much lower thermal conductivity.

For the test, the 100Cr6 block was heated until its entire temperature reached either 100 °C or 160 °C. When the desired temperature was reached, the lower traverse of the universal testing machine was lifted upwards, and the both bodies were brought into a direct contact until a force of 100 N was reached. Usually, more force was applied due to the lag in control loop. After ~15 s of both bodies in contact, the tests were terminated. All tests were repeated at least three times for confidence level. In the case of sliding contact temperature determination for polymers, subsequent analyses were not available. The implementation and usage of the thermo-camera does provide a reliable result concerning outside-surfaces maximum temperature and temperature gradients of the specimen. Therefore, it can be applied for correlations to the interfacial temperature. The measured temperatures of reference material PEEK-TC at sliding conditions of 1 m/s at 1 MPa and RT were compared to numerical calculation regarding flash temperatures. As another approach, the strongly anisotropic XC-2 material was used with different fiber orientations. The fiber orientation has a strong influence on the CoF and thermal conditions within the sliding contact as shown by Flöck [42]. These should be in accordance with the measurements.

Specimen Material	Normal Pressure [MPa]	Sliding Speed [m/s]	Counterb. Temp. [°C]	Step Time [hh:mm]
PEEK-TC	1/5/10	1	RT	00:10
PEEK-TC	1	1/3/5	RT	00:10
PEEK-TC	1	1	RT/100/150	00:10
XC-2-N	1/5/10	1	RT	00:10
XC-2-N	2	1/2/3	RT	00:10
XC-2-N	2	1	RT/100/150	00:10
XC-2-P	1/5/10	1	RT	00:10
XC-2-P	2	1/2/3	RT	00:10
XC-2-P	2	1	RT/100/150	00:10
XC-2-A	1/5/10	1	RT	00:10
XC-2-A	2	1/2/3	RT	00:10
XC-2-A	2	1	RT/100/150	00:10

Table 7: Temperature measurement validation tests

The test schedule is given in Table 7 and gives an impression of the large amount of conditions studied for later correlations. Tests with normal ("–N"), parallel ("-P") and axial ("–A") fiber orientation towards the counterbody were executed. A calibration of the force sensors prior tests was necessary. Also the Fluke 8846a multimeter voltage measurement had to be calibrated because of environmental disturbances prior tests. Only the evolving thermal conditions were of interest, while changes until the steady-state behavior was reached were not the focus of these tests. Accordingly, the testing time could be strongly shortened. Specimen preparation was similar to the RCA/TFL measurement validation tests (compare section 5.5.1).

5.6. Investigation of Failure Mechanisms with Combined Measurements

While in lubricated sliding tests all measurements were already applied together within the validation stage, concerning dry sliding this must be done separately. Otherwise, possible disturbances between RCA determination and dynamic thermocouple measurement method may occur as they were both based on the evaluation of electrical characteristics of the sliding contact. Regarding the following experiments, both measurements were applied alternating in time periods of 10 s. This leads to results with worse time related resolutions, but provides combined information. The test schedule was organized taking into account possible interdependencies of the RCA, temperatures and TFL in combination with CoF and wear rate. In order to find corre-

lations, the main focus was on constant rising frictional energy. Therefore, the sliding speed and the pressure were raised alternatingly, until a severe wear condition was reached and the PEEK-TC specimen was worn down rapidly. In order to demonstrate the influence of the shaft temperature on failure behavior, a second test was conducted. Approximately 80 % of the former failure load was applied and the counterbody temperature was increased stepwise. Specimen preparation was again similar to the RCA/TFL measurement validation tests (compare section 5.5.1).

Specimen Material	Normal Pressure [MPa]	Sliding Speed [m/s]	Counterb. Temp. [°C]	Step Time [hh:mm]
PEEK-TC	2 4 4 6 6 etc.	1 1 2 2 3 etc.	RT	00:30 00:30 00:30 00:30 00:30 etc.
PEEK-TC	~80% of max.	~80% of max.	50 60 70 etc.	00:10 00:10 00:10 etc.

Table 8: Test schedule for combined measurements

Some measurements required a reference and sensors must be calibrated. For longer tests with combined load cases such actions were repeated (compare section 4). The combined measurements, as presented in the test schedule (Table 8), display the maximum amount of channels of possible measurements. The complete program sequence consisted of three initial steps and two pre-steps for each main load case, followed by one post-step. Additional heating added another pre-step before each main load case. For instance, 10 different load cases resulted in a total amount of 53 steps, indicating the overall complexity which was achieved and had to be understood in detail.

6. Results and Discussion

6.1. Materials and System Characterization

6.1.1. Mechanical, Thermal and Electrical Properties

The material properties regarding mechanical, electrical and thermal characteristics of the materials used are shown in Table 9. Underlined values for tensile strength of the XC-2 material are measured values from Flöck [42].

Material	Density [g/cm³]	E-Modulus [GPa]	Tensile Strength [MPa]	Elongation at Break [%]	Glass Transition Temperature [°C]	Melting Temp. [°C]	Thermal Conductivity [W/mK]	Thermal Capacity [J/gK] @ 25 °C	Specific Electrical Resistance [Ohm*mm²/m]
PEEK-TC	1.65	14.1 (@ RT) 13.6 (@ 100 °C) 0.34 (@ 200 °C)	141	1.5	141.4	342.8	0.86	1.2	$2.72*10^9$
XC-2 N	1.55	Compare Figure 22	~1850		141	343.6	6.1	1.2	$3.36*10^2$
XC-2 A/P			~80				0.72		$2.7*10^5$

Table 9: Material properties.

In order to determine the influence of fiber orientation on sliding characteristics, the dependence of XC-2 material's mechanical and thermal properties on fiber orientation was investigated by DMTA. The influence of the fiber orientation on interface temperature and RCA was assumed to be detectable by the use of enhanced measurements techniques. The fiber orientation's strong influence on the E-modulus is clearly shown in Figure 22, i.e. the composite shows a much higher complex E-modulus along the fiber orientation direction. When the temperature reaches regions close to the glass transition temperature of the PEEK matrix, both specimens' E-modulus dropped more than half compared with E-modulus at RT.

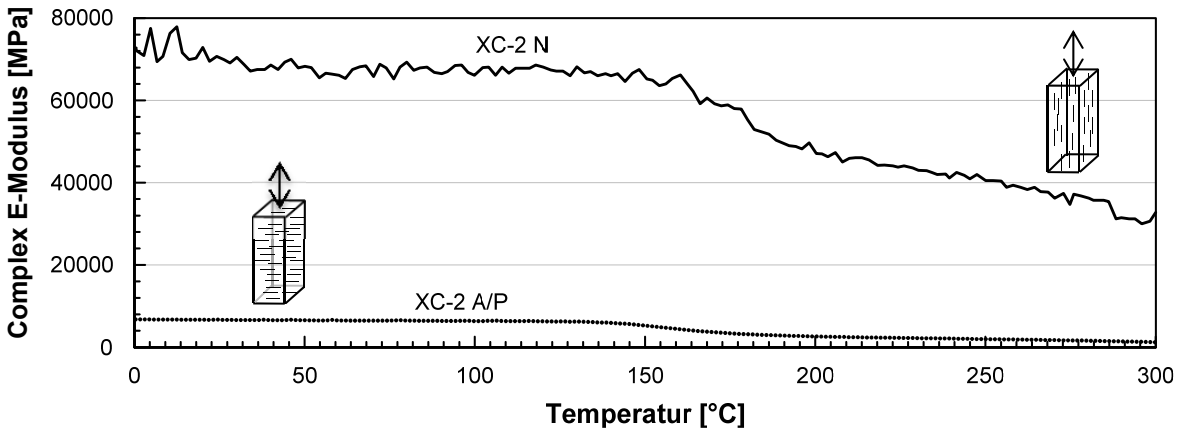

Figure 22: Temperature related E-modulus for XC-2

Summary:

- Materials are characterized regarding mechanical, thermal and electrical properties.
- Strong anisotropic effects are visible for XC-2 in electrical conductivity and mechanical properties; depending on fiber orientation.

6.1.2. Seebeck-Coefficients

The results of the absolute Seebeck-coefficient determination are given in Figure 23. Fiber orientation shows only a minor influence on the Seebeck-coefficient for XC-2 material, resulting in only a slight offset. The Seebeck-coefficient of PEEK-TC is smaller in comparison to XC-2. Whether the length of fibers, different electrical conductivity of the compound or the addition of graphite in PEEK-TC is responsible, cannot be clarified at this point. For the test rig's Seebeck-coefficient, extrapolation was only done up to 500 K since no higher temperatures were expected for the counterbody surface. All Seebeck-coefficients for polymer material showed a stronger incline of Seebeck-coefficients over temperature than the tested metals.

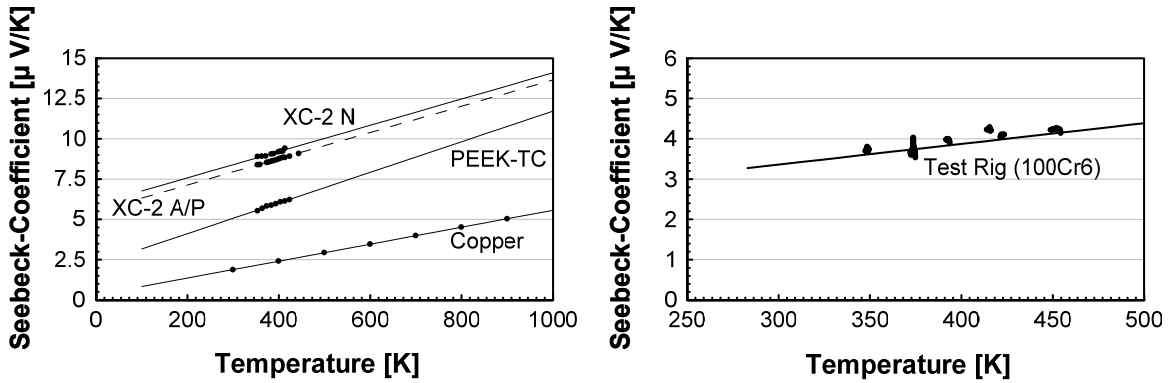

Figure 23: Seebeck-coefficients for tested materials and reference and test rig

The Seebeck-coefficients as a function of temperature for use in the modified thermocouple equation are given in Table 10. The Seebeck-coefficients at higher contact temperatures were extrapolated from the equations obtained from measurements.

Material	Function of Seebeck-Coefficient [µV/K]
Copper	$S_C(T[K]) = 0.0052 * T_C + 0.3077$
PEEK-TC	$S_C(T[K]) = 0.0095 * T_C + 2.2208$
XC-2 N	$S_C(T[K]) = 0.0081 * T_C + 5.9524$
XC-2 A/P	$S_C(T[K]) = 0.0081 * T_C + 5.5048$
Test Rig (100Cr6)	$S_C(T[K]) = 0.0051 * T_C + 3.2569$

Table 10: Functions of Seebeck-coefficients

Although such coefficient determination is quite time-consuming, it is necessary in order to obtain correct results with the Seebeck-effect related temperature measurement.

Summary:

- Seebeck-coefficients were determined and extrapolated for materials examined and test rig.
- Seebeck-coefficient increase over temperature is stronger for the polymers used than for metals.

6.2. Measurement Techniques

6.2.1. Results of Dry Sliding RCA and TFL-Thickness Measurement

6.2.1.1. Correlation between RCA and Electrical Resistance

The electrical resistance of PEEK-TC material as functions of contact surface and normal pressure is given in Figure 24 a). This investigation was conducted by machining specimen with different cross section sizes (compare section 5.1.2.5) in order to determine their influence on electrical conductivity. A close dependency of electrical resistance on the contact surface according to the equation presented in section 4.1.2.1 is obvious. Therefore it should be possible to conduct RCA measurements with polymer compounds using their intrinsic electrical conductivity as meter for the RCA.

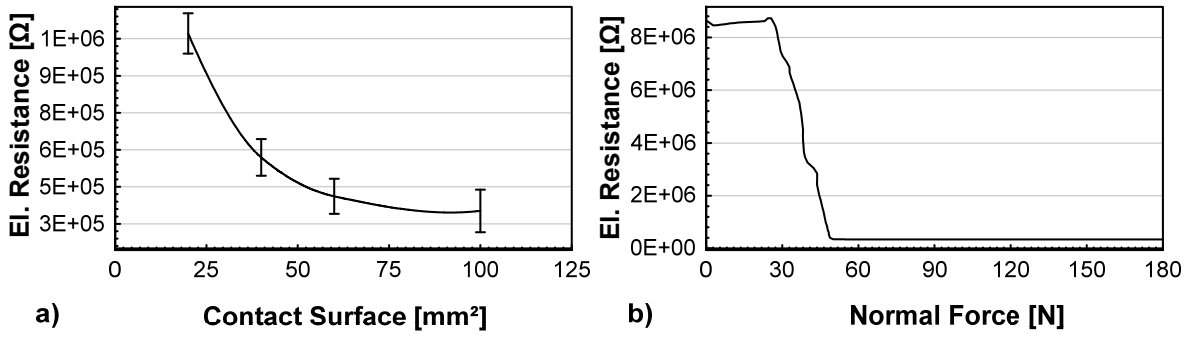

Figure 24: Electrical resistance for PEEK-TC as functions of contact surface (a)) and pressure (b))

In order to determine the resistance as function of the contact surface both contacting surfaces were painted with argent finish. The influence of an unpainted surface in contact with a steel ring as counterbody as a function of normal force is given in Figure 24 b). As soon as a normal force of 60 N is reached, almost no further change in electrical resistance is evident. This load equals a normal pressure of ~4 MPa. This value is of course dependent on the pre-treatment of the specimen and the actual fiber and graphite distribution on the surface. For the following tribology tests a force of 200 N seemed to be sufficient to determine the minimum specific electrical resistance of a contact. The values obtained for every specimen regarding electrical conductivity through sliding contact in static conditions were used for scaling of the RCA results. Due to the high normal force this static condition was set as 100 % surface in contact.

Summary:

- Influence on contacting surface is in direct correlation to electrical conductivity as expected from theory.
- At static testing with ~4 MPa full contact between specimen and counterbody ring is achieved. This used as reference with 100 % surface in contact.

6.2.1.2. Measurement Methods for Confocal Based TFL Thickness Determination

The before mentioned routes for temperature compensation regarding confocal measurement of TFL thicknesses were investigated and results are given in Figure 25. All investigations were executed without any specimen attached. The diagram on the left was obtained with permanent measurement on one spot of the counterbody ring while rotating at 1 m/s without any specimen. The changes in the counterbody temperature exert a strong influence on the confocal distance measurement result, giving a deviation of more than 40 µm at a temperature difference of 75 K.

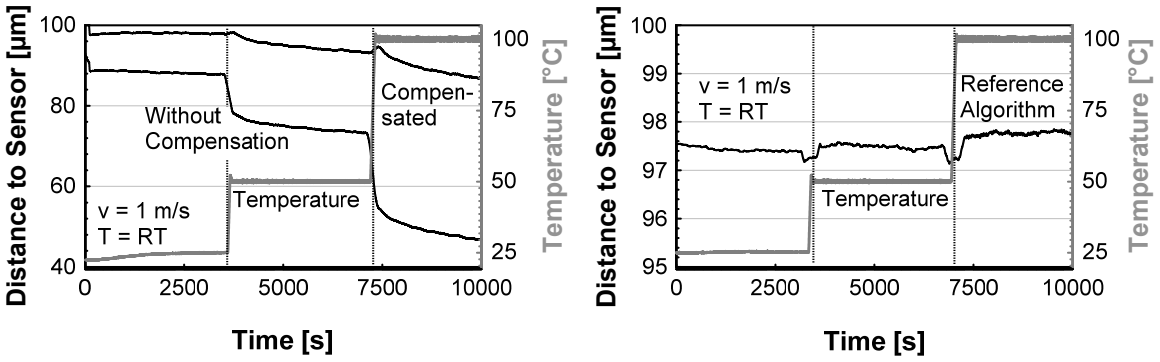

Figure 25: Temperature compensation methods comparison for confocal measurement without specimen

The attempt of a temperature compensation using the measured temperature of the counterbody is also shown, but was not leading to a satisfying result. Although compensation of the counterbody ring temperature seemed to enhance the result, other heating effects of the shaft as well as the confocal measurement unit etc. still remain, leading to several µm deviation over time. The reference-algorithm attempt described in section 4.1.1.2 is given in the right diagram, showing a comparably stable result with only slight deviations. Due to a cycle time of ~40 s for one thickness measurement, a monitoring of rapidly changing conditions is not possible with the reference-algorithm measurement method. Nevertheless, it was the only solution to obtain a thickness measurement for changes in TFL thickness without high additional costs. It was also found that a certain running-in period for the test rig enhanced the results which could be obtained using the reference-algorithm. Due to this effect, the tests carried out afterwards were always performed after the test rig was at “working temperature”, achieved by at least 1 h of running time without specimen at 1 m/s. A reason could be found in the bearings of the shaft as their clearances were smaller at working temperature and the shaft obtains a more rigid guidance leading to smaller deviations. During the experiments also a certain influence of the inductive heating system control loop was found, resulting in a slightly higher measurement noise. This could easily be filtered out in the post processing as a smoothening of the resulting graph or average determination for scalar values has to be performed anyhow. For a reference test without heating and no specimen applied, a standard deviation of 0.12 µm was measured and calculated for 10 h running time at 1 m/s. This basically reflects the accuracy which can be achieved over longer measurement periods. A more precise result may be obtained by intensive post-processing.

Summary:

- A constant measurement is not precisely enough; even if a temperature calibration function is applied.
- The reference-algorithm method is sufficiently insusceptible against temperature influences and achieves results with good local and acceptable time resolution.

6.2.1.3. Determination of Contact Characteristics on Different Counterbodies

The results of the experiments with counterbody rings prepared with different surface roughnesses are given in Figure 27 and Figure 28

Specimens used were made of PEEK-TC. The analyses were conducted using WLP and are given in Table 11 for the initial counterface as well as the TFL trace on the counterbody. Additionally, the average of three heights was determined, measured after the tribological exposure for TFL.

Counterb. Surface	Counterbody Roughness Ra [µm]	Counterbody Roughness Rz [µm]	TFL Roughness Ra [µm]	TFL Roughness Rz [µm]	TFL Height [µm]
As Received	0.31	1.7	0.26	2.1	0.12 ±0.02
Glass	0.55	3.1	1	6.8	2.97 ±0.34
Sand	1.31	6.4	0.72	5.6	5.54 ±0.24

Table 11: Surface roughnesses on counterbody rings

The confocal measurement method of TFL thickness is supposed to be independent of the counterbody surface roughness due to high average building times during measurement. This also implies that it is not possible to monitor whether a uniform TFL forms on the counterbody or e.g. only grooves are filled with transferred material.

The obtained roughness data are in accordance with the SEM pictures given in Figure 26. While for the unmodified counterbody ring only slightly filled roughness grooves are visible, the glass and sand blasted surfaces show a thick TFL. Also the high surface roughness, especially of the TFL which was build up on the glass blasted ring is visible. Both, the glass blasted counterbody ring as well as the sand blasted one, show partially uncovered areas of original steel surface, indicating some inhomogeneous TFL characteristic.

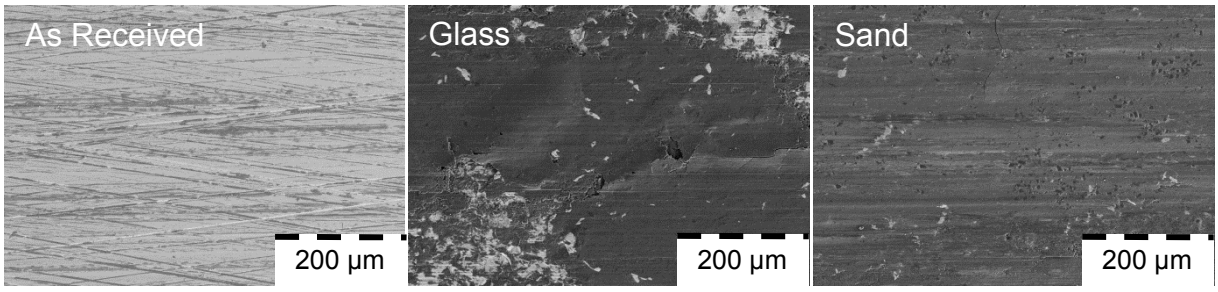

Figure 26: SEM results of TFL on different surface roughnesses

Strong dependence of the CoF on the counterbody surface is evident from Figure 27, indicating the lowest friction for the glass blasted surface while the unmodified coun-

terbody ring remains on a high CoF. The low friction coefficient of the sand blasted surface might result from highest TFL roughness, leading to overall small RCA and therefore low adhesion. Regarding wear the rougher surfaces demand a higher initial filling with transferred material. After several hours of running time the wear rate becomes stable and shows a similar incline to the wear rate of the unmodified counterbody ring.

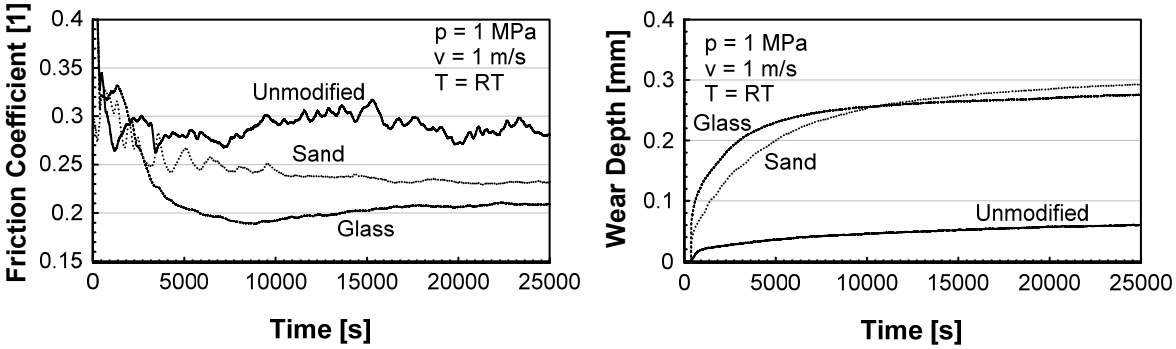

Figure 27: Sliding characteristics for different counterbody roughnesses

The real contact area was calculated using the initial static contact reference. As indicated in the previous chapter it was evident that above a pressure of around 4 MPa full contact seems to be achieved. This reference is regarded as 100 % surface in contact, considering the special characteristics of polymer compounds. For PEEK-TC the matrix material is not conductive, since a percolation threshold can only be achieved if the material contains enough SCF and graphite fillers, which is not the case here. This indicates that the measured real contact area is filler-related. Another aspect must also be taken into account: During investigations on a comparable system regarding matrix and fillers, Noll [83] showed that the percolation threshold for SCF/PPS compound was already reached at 5 wt.% SCF while for graphite/PPS a filler content of 15 wt.% was necessary. The low necessary SCF content is reasonable due to the longer fibers used (~1 mm length).Variations in filler concentration were performed in 5 % steps. Even at 20 wt.% filler content the electrical conductivity showed a difference of two decades between SCF and graphite filled materials. Also it was shown that if 10 wt.% graphite was added to a PPS compound filled with 10 wt.% SCF, the changes in electrical conductivity are comparably small.

PEEK compounds containing 10 wt.% graphite were additionally investigated in the current study for reference. Specimens were obtained from another project, using the same matrix material PEEK 450G (Victrex® Europa GmbH; Germany) with 10 wt.% content of different graphite types. These were RGC39-A, RGC4-A smaller in size, and purified natural type LBG8004 (Superior Graphite Europe, Ltd.; Germany). No matter which of the different graphite types was used, electrical conductivity was too

small to be detected with the equipment used, even for the largest specimen's width of 4 mm x 20 mm. This indicates the fibers can be expected to be the dominant filler regarding electrical conductivity for the PEEK-TC system. The measured real surface area for PEEK-TC is therefore mainly dependent on the contact between steel and SCF. In the following this is called fiber-to-steel real contact area (FSRCA). The influence of the counterbody roughness on the measurement itself can be neglected as the time resolution is not sufficient to determine small events with a fast rotating counterbody ring. Values near the 100 % initial contact area were found in the results, supporting this theoretical simplification.

The results of the TFL thickness measurement and the real contact area are shown in Figure 28. The y-axis for the confocal measurement was adjusted in post-processing using the reference data without specimen attached which is also part of the heat-up phase of the test rig. The progress of developing TFL in various thicknesses is obvious for the different counterbodies. The correlation towards the CoF behavior and the wear progress is especially evident for both of the rougher counterbody rings.

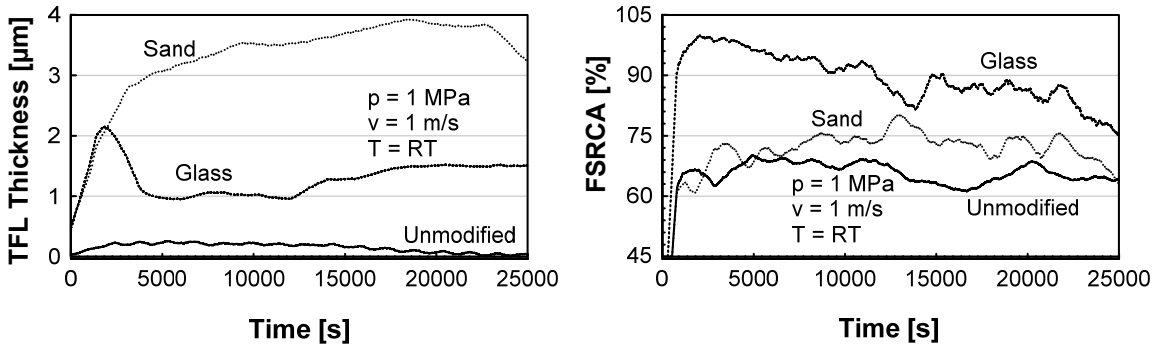

Figure 28: Contact characteristics for different counterbody roughnesses

A comparison of measurement results to theoretical calculations as performed by e.g. Ashby et al. [17] was not found to be suitable. Their calculations were intended for homogeneous materials while PEEK-TC consists of a polymer matrix with a low stiffness if compared with e.g. steel and short, stiffer fibers. If calculations according to Ashby et al. are compared with experiments by Váradi et al. [21] a deviation of one decade, under-estimating the RCA by calculation, is found if best approximated values are used as they were given in their publications. This is especially interesting as Váradi et al. used continuous carbon fibers in a PEEK matrix. They provide a much higher stiffness in normal fiber orientation and therefore should be much better comparable to steel than PEEK-TC. They also found that stiffness has a direct influence on RCA, which is again in accordance with the theory of Ashby et al., claiming the direct influence of material hardness on RCA. For PEEK-TC in Figure 24 it was already obvious that elastic and plastic deformation at ~4 MPa lead to an almost com-

plete contact of fibers on the surface, indicating a RCA of at least ~9 % as the volumetric fiber content is in that range. Theoretical estimations by calculations of Ashby et al. are in this case around two decades less. From this point of view a theoretical calculation does not seem possible. Experimental data with comparable conditions, especially in-situ during sliding, were not available in literature. Concerning the theory of Ashby et al. and experiments by Váradi et al. it is however obvious, that a correlation between RCA and normal pressure exists due to elastic and plastic deformation as a function of materials stiffness. When changing velocities or counterbody temperatures, the lowered E-modulus due to frictional heating can be estimated and therefore be used to prove FSRCA measurement, too. A steady state behavior is achieved for sand blasted and unmodified counterbody rings at ~7500 s already and for glass blasted ring at ~20000 s, which is in good accordance to the CoF behavior. If all results are compared, especially the glass blasted counterbody ring results are of interest. This ring shows a partly closed TFL, which can also be observed optically from the SEM pictures given in Figure 26. This configuration showed the lowest CoF but highest FSRCA and highest surface roughness. This indicates that a majority of fibers in contact can bear the load being in direct contact to steel counterbody or at least partly with transfer film. Additional adhesion effects of pure matrix to TFL are small due to the high surface roughness of the TFL, resulting in an overall small CoF. Additionally, the average thick TFL can also fill initial surface roughness grooves and allow smoother sliding for the fibers on the counterbody ring.

When final TFL heights measured in-situ (Figure 28) are compared to static values measured after tribological tests using WLP (Table 11), the results show a similar relative tendency. Concrete absolute values are in rather good accordance. In SEM pictures (Figure 26) the main reason for deviations between both measurements can be estimated in the inhomogeneity of the TFL. It is evident that for a unmodified counterbody ring in-situ and WLP measurements are in very good accordance while the results for a thicker TFL show an obvious deviation. SEM show that in certain areas there is a TFL, while at a different location on the same ring neat steel surface is still visible. The in-situ measurement can only cover one thin line of the sliding trace. With increasing inhomogeneity of the TFL the risk increases that a line is scanned with non-representative thickness. A reason could be e.g. a carbon fiber of different orientation, “scratching” away a TFL in this section. In view of this, the deviations between both measurement methods are reasonable. However, relative changes in results of both measurement methods are in good accordance. This indicates that valuable measurements and results can be conducted using the new enhanced measurement method with a quality comparable to post WLP analysis. For a further

improvement of the measurement accuracy, several lines on the sliding trace must be scanned in-situ. Due to thermal expansion effects and time resolution this is only possible using a second confocal sensor, which is then only used for temperature compensation.

Summary:

- The TFL thickness measurement is in a good relatively accordance to the thickness determined ex-situ using WLP. Deviations can be explained by the TFL morphology. The executed measurement is usable for in-situ TFL thickness determination.
- RCA determination was found to measure the real contact area between carbon fibers and steel; declared as FSRCA.
- Crosslinks to literature using metal sliding partners are not feasible.
- Measurement results for TFL thickness and FSRCA determination correlate with CoF, wear rate and SEM analysis. FSRCA measurement is indicated to work properly.

6.2.1.4. Correlations under Various Load Cases

Clear correlations for CoF, real contact area and TFL thickness with changing normal pressures are shown in Figure 29. It is difficult to compare the wear depth with the formation of a transfer film as the material needed for a sub-micrometer scale TFL is comparably small. The wear depth was always calibrated for new load conditions. A slightly increased, fiber-related real contact area due to higher elastic deformations in the polymer compound resulting from increased pressure from 1 to 5 MPa is notable. Such behavior was also expected by Ashby et al., claiming an increasing RCA for higher normal pressures in their theory. For the second increase of the load such behavior is not present, indicating that most of the possible local elastic deformations are already exceeded. Again, the better fiber-counterbody contact due to filled grooves may be the reason for the close correlation of FSRCA and TFL thickness.

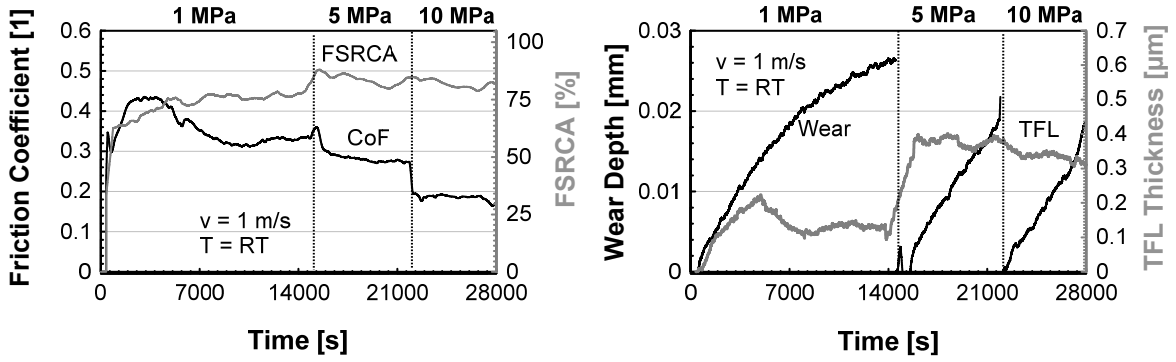

Figure 29: Contact characterization pressure variation

For variations in sliding velocity (Figure 30) a decreasing fiber-related real contact area is in correlation with the CoF, showing similar tendencies. The measured TFL thickness increases if a higher energy input is introduced to the sliding contact.

In contrast to the variation of normal pressure, the fiber-related real contact area decreases with increased velocity. This is owed to the contact condition. In contrast to the increased pressure a less “tight” contact occurs for higher velocities and therefore separation effects of the slightly thicker TFL are more severe.

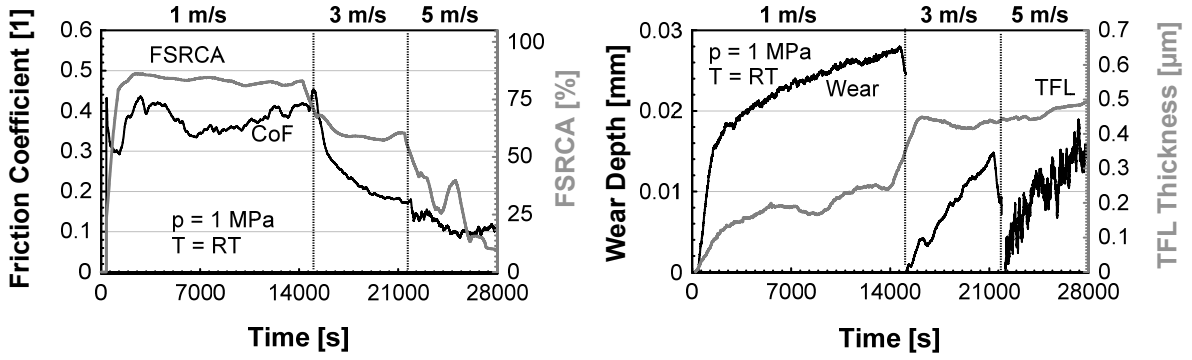

Figure 30: Contact characterization velocity variation

The variation in the counterbody’s temperature supplies further, clearer data for analysis. The change from 50 °C to 100 °C and 150 °C always leads to a descending CoF and increasing fiber-related real contact area, as shown in Figure 31.

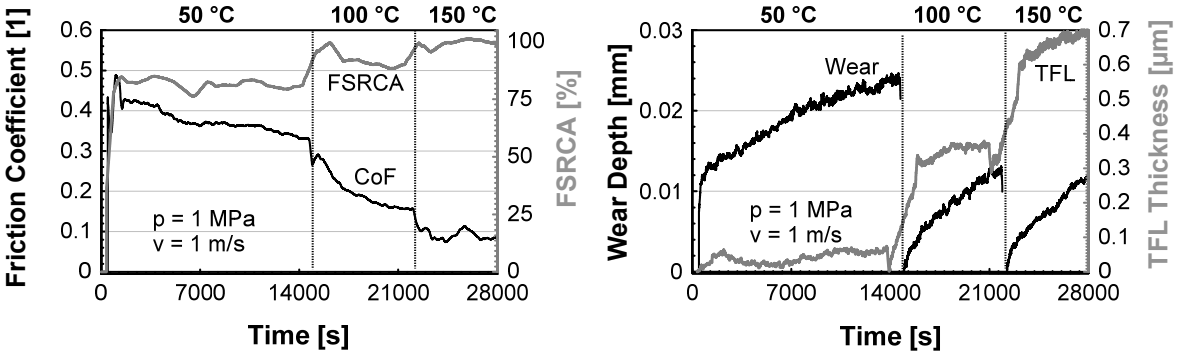

Figure 31: Contact characterization counterbody temperature variation

Reasons for these correlations can be found in a hotter counterbody temperature, introducing massive energy into the polymer compound specimen, resulting in a softening of the matrix. In case of 150 °C counterbody temperature the maximum measured temperature on the specimen’s outside surface was ~125 °C. As this temperature is already close to glass-transition temperature of the specimen it can be assumed that inside the specimen glass-transition onset is surely reached in regions near the sliding interface. This can also be the case for 100 °C counterbody temperature in a smaller depth. However, that may remain in an assumption. A softened matrix leads to a lowered E-modulus and by this according to Ashby et al. to an increas-

ing RCA [17]. Therefore, for a polymer compound, more fibers are in direct contact with the steel counterbody due to the softened matrix. The increase in TFL thickness is in direct contrast to the decrease of the CoF. Again, this can be explained by a smoother sliding behavior, with fibers hitting fewer walls of grooves. The rapid increase of the TFL for every change in counterbody temperature is in good accordance with the higher wear progress at the initial stages of each load case as can be seen in Figure 31. Although the changes in the wear graph are small, their direct correlation to the TFL thickness change is evident. It should be noted that the real wear in these initial stages is expected to be even higher. But due to thermal expansion of the polymer specimen the real wear is under-estimated during these periods.

Summary:

- Results of TFL and FSRCA measurement can be correlated to each other and CoF as well as to the wear rate under increasing sliding velocity, normal pressure and counterbody temperature.
- Correlations are indicating the correct function of both measurement methods and can be referred to tribological mechanisms.

6.2.2. Results of Lubricated Sliding RCA and TFL-Thickness Measurement

Regarding lubricated sliding the results of the continuous sliding test are given in Figure 32. It shows that the CoF increases while FSRCA decreases in the beginning. This behavior is reasonable due to the PoR setup. Using this configuration, the maximum Hertzian contact pressure is lowered with progressing wear. A lowered normal pressure in combination with lower oil viscosity due to frictional heating leads to increased oil film coverage within the sliding contact. Usually it would be expected that a better surface coverage by the oil film lowers the CoF. The lubrication regime for this test is boundary friction. It was explained in section 2.1.8 that molecular interdependencies between surface and oil as well as surface characteristics are dominant influencing parameters in this lubrication regime. Strong correlations between FSRCA and CoF cannot be established by these results. Nevertheless, a smooth and constant behavior regarding the FSRCA measurement is evident and correlations may be found under changing load cases.

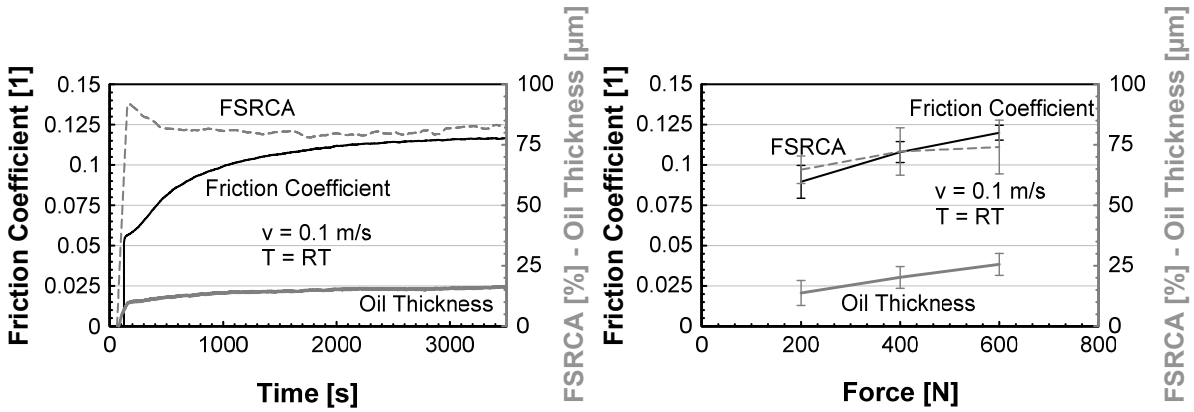

Figure 32: Continuous sliding and force variation

The oil film thickness measurement outside the sliding contact using a confocal sensor had to be conducted without alternating reference-algorithm because of the oil-adhesion in the reference scan area. Therefore changes in temperature were to be considered in post-processing. However, it is evident that the measured values are much higher than the temperature expansion. For temperature variation (Figure 33) initial offsets for the three temperatures were added in the results during post-processing. The offsets were calculated from the results given in section 6.2.1.2. For the continuous sliding test a slight increase in the measured oil film thickness outside sliding contact can be found. The measured values are in the range of several µm and in contrast to the CoF behavior. For normal force variation (Figure 32) an even stronger increase is evident with increasing normal force. An explanation was found during the test runs as it became obvious that in some areas oil adheres to the counterbody ring after it passed the sliding contact. This additionally attached oil is of course measured by the confocal sensor, too. From beginning it was unsure how the measured oil film thickness outside the sliding contact may correlate with the real oil film thickness within the sliding contact. These results, in combination with observations during the test runs, lead to the conclusion that this measurement procedure is not suitable nor supplies comparable correlations. In contrast, the measured FSRCA correlates very well with the CoF under increasing normal force (Figure 32). According to Stribeck's theory, given in section 2.1.8, the higher force leads to a shift of lubrication regime towards boundary friction. This results in less separation effects by oil and more FSRCA, leading to an increased CoF. Additionally, the FSRCA is also increased by more nominal contact area due to higher maximum Hertzian pressure as well as wear progress. These effects are clearly visible in the results and therefore are correlations evident, proofing correct usage of the FSRCA measurement technique. For a variation in sliding velocity (Figure 33) also close correlations between the CoF and the FSRCA measurement can be determined in reference to the Stribeck curve. Due to the increasing sliding speed, the CoF drops as the lubrication

regime changes from boundary to mixed and finally hydrodynamic or elasto-hydrodynamic respectively. While changes in contact conditions are not recognizable from the CoF after a sliding speed of 0.3 m/s is reached, the FSRCA measurement still provides visible differences. Sliding velocities higher than 1.5 m/s indicated an increase of the FSRCA in combination with rising CoF. According to the Stribeck curve for higher sliding velocities the CoF can increase again due to turbulent flow within the oil layer. The combination with the FSRCA measurement shows for the current system that a slight break down of the oil film occurs. This matches observations during the test runs as oil started to fly away from the counterbody ring at high velocities.

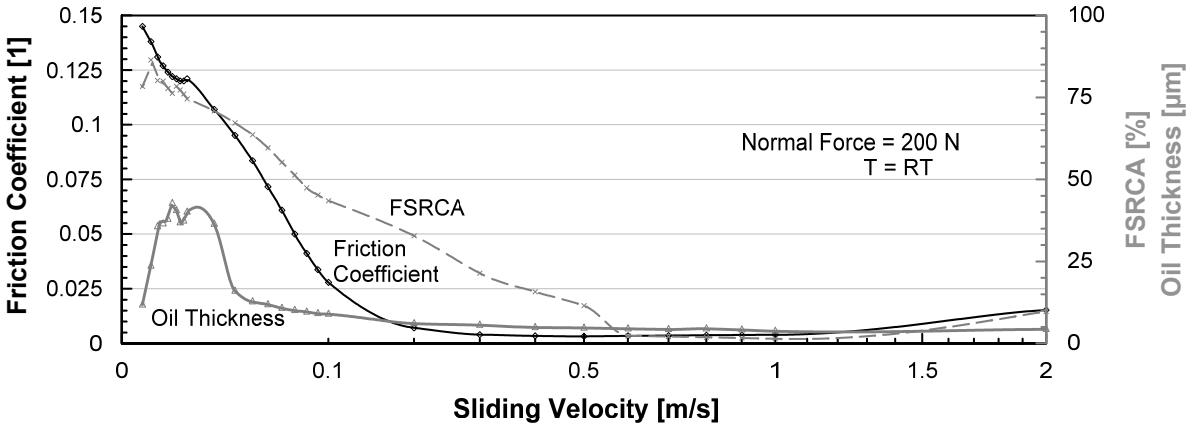

Figure 33: Velocity variation

The equations based on Mohrenstein-Ertel with enhancements by Dowson and Higginson, which were presented in section 2.1.8.4, are used with the experimental data. An EHD onset point was calculated using Ra values obtained after the test for counterbody ring and specimen. As mentioned in section 2.1.8 there is no information in literature concerning the use of either Ra or Rz in order to calculate λ. The use of Rz delivered an EHD onset point of ~13 m/s which appears high if correlated with the experimentally obtained CoF, indicating EHD already at 0.3 m/s - 0.4 m/s. Using Ra results in an EHD onset point at 0.37 m/s. Calculations according to Dowson and Higginson [141, 142] result in similar EHD onset point whereas the sum of counterbody and specimen Ra is exceeded twice at 0.33 m/s. For onset point using Rz again a higher velocity of 4 m/s is calculated. If the CoF is compared with the EHD onset points for different surface roughness parameters Ra and Rz, it is evident that for ~0.4 m/s a majority of surface asperities is separated by EHD lubrication. Some of the highest asperities must still be in contact since the complete surface roughness is not exceeded at this sliding velocity. This behavior is also indicated by the FSRCA measurement which still indicates significant contact up to 0.6 m/s and has its lowest value at ~1.1 m/s. Although the CoF does not provide any more changes in this re-

gion, the FSRCA measurement does, indicating helpful usage of the measurement technique. Besides effects like the above described oil-film break down, the most interesting issue regarding FSRCA measurement may be the wear characteristics. Although the CoF already gives an impression of an EHD regime, still solid contacts occur, resulting in a higher wear rate. Using FSRCA measurement this can be considered for a further optimization of the system by e.g. slightly changed sliding velocity.

The influence of temperature on the viscosity and therefore on the adhesion of the oil after sliding contact towards counterbody is obvious (Figure 34). With decreasing viscosity due to higher temperature less oil sticks to the counterbody ring resulting in a smaller oil film thickness measured. The increased sliding velocity within the temperature variations again shows an antipodal correlation between measured oil film thickness and velocity, unlike theoretical expectations. In summary no usable information can be obtained by this measurement method.

The above discussed correlation between CoF and FSRCA measurement with increasing velocity is again found in Figure 34. Additionally, with increasing temperature and therefore decreasing oil viscosity a shift of the sliding conditions within the Stribeck curve is evident. At higher temperatures more and more FSRCA is measured and from the CoF it is obvious that the hydrodynamic lubrication regime is no longer reached. While at 75 °C mixed lubrication could still be expected for higher velocities, at 100 °C primarily boundary friction takes place.

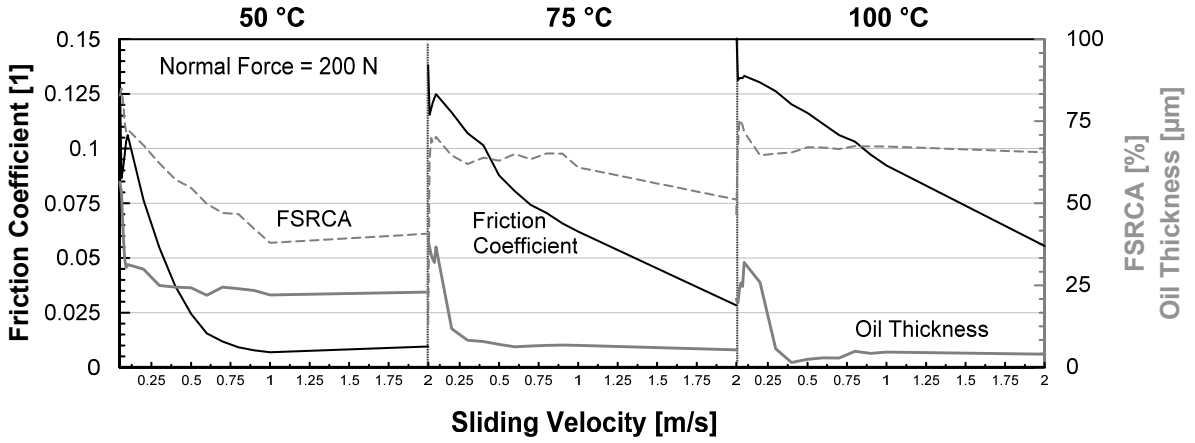

Figure 34: Temperature variation

The results are in agreement to the Stribeck curve theory as influences of sliding velocity, normal force and oil viscosity (dependent on temperature) could be observed and clearly correlated between CoF and FSRCA measurement. In section 2.2.6.2 the state of the art regarding resistance measurement under lubricated sliding was presented. It was assumed that the tested material can be a key factor in the success of

the current set-up, contrary to other studies which covered metals as specimens that provide comparably high electrical conductivity. The overall resistance of the contact area results of the amount of single contact junctions. In an equivalent circuit diagram this can be described as many resistors in parallel. If low resistance is already achieved with a few junctions due to high conductivity of the material, the resolution of measurement equipment is soon limited. The inconstant sliding conditions increase the difficulties. For less conductive polymer materials a much bigger measurement range up to MΩ is feasible and therefore the resolution is increased.

Summary:

- Oil film thickness measurement outside the sliding contact does not provide useful results.
- FSRCA determination is in good accordance with CoF and calculated EHD onset point, offering helpful information about the sliding contact, under changing load conditions as well.
- In contrast to the state of the art regarding resistive RCA measurements for metallic sliding partners, the methodology was found to deliver good results for the used PEEK-TC.

6.2.3. Results of an In-Situ Measurement of Interface Temperature

6.2.3.1. Results of Simulations

In order to prove whether the counterbody bulk temperature can be used to solve the modified equation in the dynamic thermocouple measurement, simulations of the sliding system were conducted. The principle structure of the simulation and the input parameters (Table 4) are given in section 5.3. The temperature at a specific nodal point on the counterbody disc surface and a couple of points on the specimen surface, for which the average was calculated, were used for results. An overview of a completed simulation with quick heat distribution in the counterbody is given in Figure 35. The heat for these simulations was only generated by frictional energy.

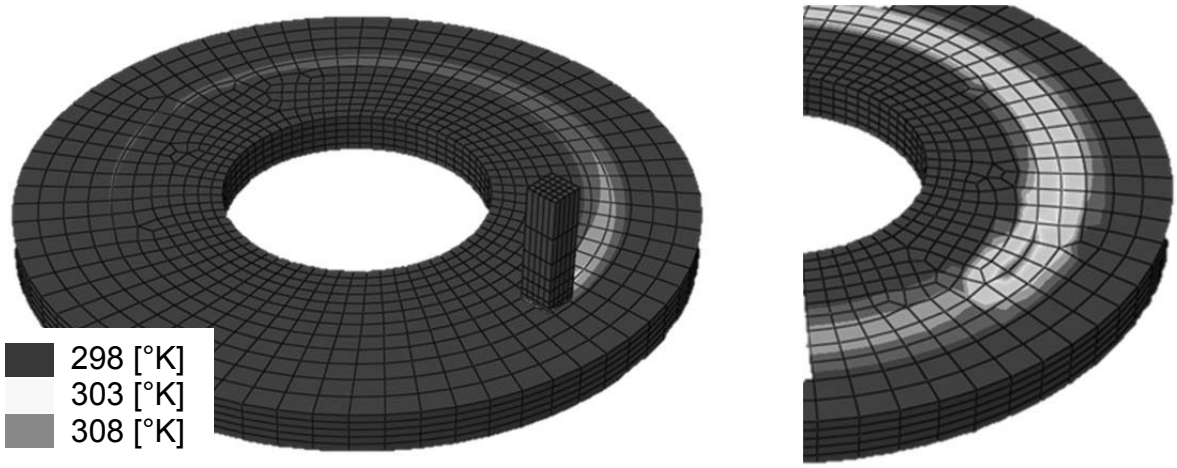

Figure 35: Simulation result for 100 % (left) and 1 % (right) surface of specimen in contact with counterbody disc

The evaluation of the simulations is given in Figure 36. It is obvious that the heating up of the counterbody ring is comparably small and less than 0.7 K for every contact period. Introduced heat is almost completely dissipated into the bulk material during the non-contacting time. No radiation and film coefficient was applied for the disc and the cooling is only due to bulk material. Even if only 1 % instead of 100 % of the pin surface is in contact with the counterbody ring, only a small difference in surface temperature of counterbody ring is noticeable.

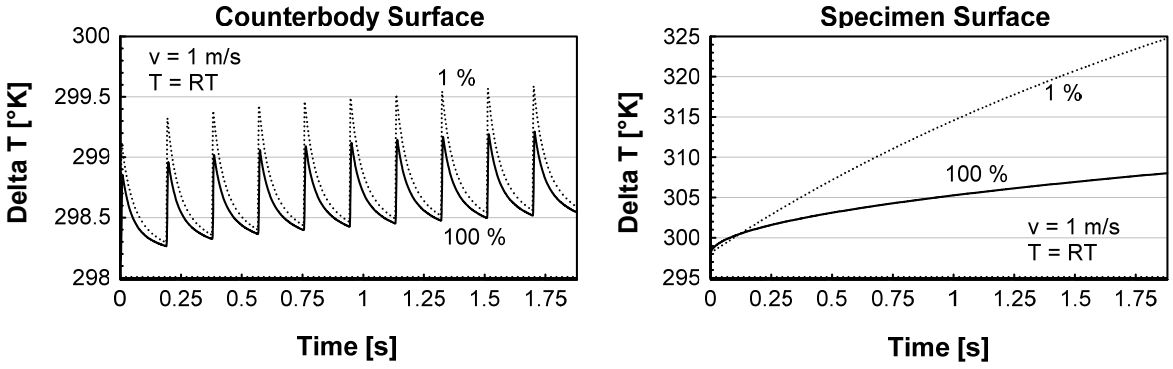

Figure 36: Temperatures on counterbody and specimen

Regarding the surface temperature of the specimen, strong differences are noticeable between complete contact (100 %) and only 1 % of surface in contact. This corresponds with the theoretical assumptions by e.g. Bowden an Ridler [190]. They claim that the surface temperature of a specimen in continuous contact is strongly related to the RCA and rises extensively if only a fraction of the surface is in contact. The simulation with much smaller specimens contact surface is only a simple approach, not considering proper bulk material cooling, radiation, film coefficient etc. But it is absolutely sufficient to give a tendency and a basic understanding. While for this simulation set-up the specimen obtains a much higher heating rate, the influence on counterbody heating is small. Theoretically this seems correct as the amount of

energy remains the same; it is only introduced over a shorter time period with higher intensity. For the specimen the difference can be found by the circumstance that the same energy must be dissipated through a much smaller surface. These results establish that the earlier assumptions are valid and the bulk material temperature of the counterbody can be used for Seebeck-effect related volumetric contact temperature measurements, in order to obtain the specimen's hot spot temperature. The experimental approach for this theory is analyzed in the next chapter and will provide additional proof.

Summary:

- The counterbody surface temperature differs from the specimen surface temperature; different thermal gradients are evident.
- The counterbody surface temperature is only slightly different from the counterbody bulk temperature.
- The RCA has only marginal influence on the counterbody surface heating.
- The counterbody bulk temperature is valid for use in the modified thermocouple equation as replacement for the counterbody surface temperature.

6.2.3.2. Results of Dynamic Contact Experiments

The dynamic contact experiments were set up in order to investigate thermal characteristics of the Seebeck-effect. Depending on these investigations it is possible to determine if different volumetric contact temperatures in specimen and counterbody can be expected. This is a prerequisite for the use of the modified dynamic thermocouple equation. Results of the dynamic contact experiments performed with different specimens are shown in Figure 37. It must be noted that the initial contact point is used to normalize the individual graphs as only relative changes in measured voltage are of interest and not the absolute Seebeck-effect related values. Counterbody temperature was kept at 100 °C ± 2 °C except for one experiment which used 160 °C.

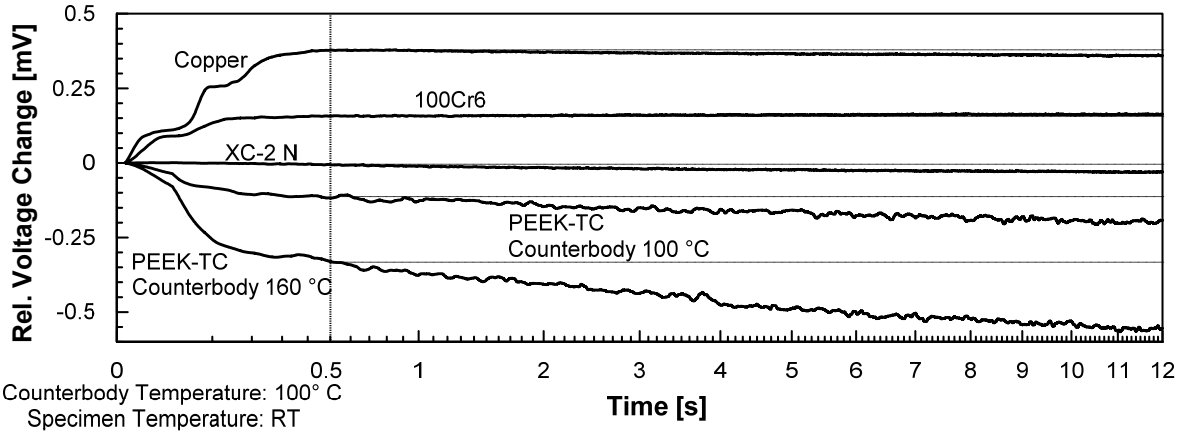

Figure 37: Dynamic contact experiment results

The reason for some graphs developing in positive and some in negative direction is found in the Seebeck-coefficient of the specimen being smaller or larger than the Seebeck-coefficient of the counterbody, which is made of 100Cr6. Except for XC-2 in normal fiber orientation towards the counterbody all combinations exhibit strong changes within the first 0.5 s of contact. The initial change in voltage already indicates the main benefit of these experiments as it clearly shows that the Seebeck-effect related voltage measured is based on time-dependent dynamic thermal processes. Detailed results are discussed separately for a better understanding of the individual mechanisms:

- 100Cr6 vs. 100Cr6: After the first thermal equilibrium is achieved the measured voltage remains completely stable. While the first 0.5 s are dominated by heat exchange from counterbody to specimen the further trend is dominated by thermal conductivities of the contacting bodies. In this combination both bodies obtain the same Seebeck-coefficient and same thermal conductivity. Therefore, no other change occurs. It could be misleading that a change in measured voltage is presented in Figure 37 since for identical materials no Seebeck voltage should evolve. Reason for this behavior is found in the way results were normalized in initial contact point. At first contact a voltage was already present due to RT of the specimen, which was in post processing then set to zero.

- Copper vs. 100Cr6: Due to the high thermal conductivity of copper the thermal equilibrium is reached rapidly, followed by cooling of the contact area for the same reason, resulting in a small drift after ~3 s.

- XC-2 N vs. 100Cr6: This is the only combination which doesn’t clearly show an initial change. This can be ascribed to the very high thermal conductivity of the fibers along the axial direction in combination with a bad thermal conductivity in radial direction. In combination with the small mass each of the fibers obtains, a very quick heating of these is possible. This heating process is too fast for the comparably slow contacting speed of 10 mm/min. Therefore initial adaption cannot be monitored and only the subsequent deviation due to cooling of the counterbody is observable. XC-2 with other fiber directions was not tested additionally since the adiabatic isolation of the horizontally stacked fibers are expected to result in similar tendencies as the PEEK-TC material.

- PEEK-TC vs. 100Cr6: All above specimens which were evaluated showed a recession of the voltage after reaching a maximum or remained stable. This is reasonable as the other materials –or the fibers in them- had higher thermal conductivities than the 100Cr6. This resulted in a continuous cooling of the steel counterbody. Due to its low thermal conductivity the initial heating of PEEK-TC is not completed after 0.5 s and may even exceed 10 s-15 s because there is always enough thermal energy present from the more conductive counterbody. This is in contrast to e.g. copper, which cooled down the 100Cr6 after the initial 0.5 s.

- PEEK-TC vs. 100Cr6 @ 160 °C: The effect of a higher contact temperature is obvious as deviation rises and gives an even better impression of the thermal effect having an influence on the Seebeck-effect related measurement. It can also be seen that longer time is required to reach a steady-state condition, as the thermal energy which must be exchanged is larger. Compared to PEEK-TC @ 100 °C, the steady state is not fully reached in the specimen. It is not yet completely heated up after the measurement sequence.

The time-related thermal effects causing a delay in heating and therefore Seebeck-effect dependent voltage generation by one of the contact partners are obvious and consistent. The time period necessary to achieve equilibrium is in the range of several 100 msec, even for materials with good thermal conductivities. This is about 2 decades above contact time in tribological sliding tests for common speeds such as 1 m/s. It can be concluded that the dynamic contact experiment supports theoretical and simulative approaches, delivering a consistent model for thermal effects occurring after initial contact of two bodies with different temperatures.

Summary:

- The Seebeck-effect is dependent on thermal flows.
- Therefore full formation of Seebeck-voltage requires a specific contact time, which is strongly dependent on the thermal conductivities of contact partners.
- It was proved that two differentvoluminetric thermal gradients may occur in contact partners for short contact times. The extended equation for surface temperature calculation as proposed in section 4.2 is therefore valid.

6.2.3.3. Definition of the Measured Temperatures

It was shown above that volume increments contributing to the Seebeck-effect related voltage require a specific contact time for the thermal heating process. Therefore the temperature near to the contact area on the counterbody ring can be used as volume-contact temperature. The question of what is the actually measured temperature using this method remains. Furey [193] established that peaks found in oscilloscope traces mark the so-called “flash temperatures” while the average trace gives the surface bulk temperature, also influenced by colder junctions. The difference can be found in terms of junctions. Some junctions can often be in contact forming a so-called “hot spot” while other junctions obtain only a random, seldom contact. This indicates that the measured value depends on the input resistance of the measurement equipment. A definition whether these temperatures are on both or only one of the sliding partners is missing. Bowden and Ridler [190], Furey [193] and Chang et al. [191, 192, 194] assumed that energy and heat dissipation is around 50 % into each sliding partner as the differences in thermal conductivities of both materials were usually small. Without taking into account the large differences in contact time for specimen and counterbody, temperatures are expected to be same. For a steady-state condition this may be a close approximation for higher sliding speeds when heat distribution becomes uniform in both sliding partners and is mostly dominated by heat sink conductivities. In case of reciprocating sliding in the experiments of Chang et al. [191, 192, 194] the movement distance is comparable to the specimen size. Regarding this, parts of specimen and counterbody surfaces are always in contact with each other and therefore the hottest temperatures on both bodies are the same.

The situation is more complicated in the present study by using polymer compounds as specimens. Although most of the frictional heat is dissipated in the counterbody it is expected from theory, simulation and experiment that surface heating for sliding contacts can be neglected. Therefore the counterbody bulk temperature instead of the counterbody volumetric contact temperature can be used for calculation of the specimen volumetric contact temperature .Fibers are commonly accepted as the load carrying part in polymer specimens. The load-carrying fibers are also forming the contacting areas and generating the hot spots obtaining flash temperatures at their contact surfaces after a running-in period. Even though the volume fraction of load-carrying fibers is small, often most of the load is carried by them. Owing to the high input resistance of the modern measurement equipment the measured and calculated temperature is expected to be the fiber-related hot spot temperature. The temperature of the other contact points, e.g. of pure matrix, is not obtained as it is electrical-

ly isolating. Other electrically conductive fillers, e.g. graphite flakes, are unable to carry a mentionable amount of load and cannot build up hot spots comparable to fibers.

Summary:

- The temperature, which is measured using a modified dynamic thermocouple method (compare section 4.2.1.3) is the temperature of hot spots on the specimen surface.
- According to electrical conductivities of matrix and fillers, it is assumed that temperatures of hot spots, formed by carbon fibers, are measured.

6.2.3.4. Comparison with Other Publications

After a consistent measurement model with adaption to the discovered thermal contact phenomena had been established, the question came up how this affects results of studies of others.

Chang et al. [191, 192, 194] did their investigations using reciprocating sliding. In [194], the contact radius of specimens was reported to be 5 mm while the stroke was 7 mm. This resulted in an area of constant contact with the counterbody. This eliminates the influence of only short contact periods and therefore their measurement technique is valid. Different thermal conductivities may lead to slight deviations of temperatures in the two bodies but the difference is assumed to be in a relatively small range. Therefore their measurement set-up is almost independent from current results and could probably be improved only slightly by the new methodology.

Furey [193] investigated a constantan ball on a steel counterbody. Static calibration was carried out without considering the Seebeck-coefficients of materials as they were not necessary for this method. He reported a mean surface temperature of ~320 °C and an average surface temperature of 115 °C measured via embedded thermocouples. These values were determined in a steady state condition of the sliding system. No information about the counterbody temperature and whether it is already constant is available in literature. In Furey's experiments more heat is distributed towards the counterbody due to the worse thermal conductivity of constantan in comparison to steel. A relatively high sliding speed of 2.24 m/s leads to a frequent contact of the same sections on the counterbody (diameter 44.45 mm). In the light of this, the temperature on the counterbody is expected to be more or less equal to the average specimen surface temperature and is therefore used for the upcoming calculation. Not all original data from their experiments is available in literature. Therefore some approximations had to suffice. The Seebeck-coefficient curve for constantan could be obtained from literature values [276] while for 100Cr6 steel the temperature

related Seebeck-coefficient was determined in the present study. Using this data a deviation of ~7 %, resulting in higher specimen contact temperature can be calculated if the original results are re-calculated with the modified theoretical model. Although the thermal conductivity of constantan is less than half of 100Cr6, the effect of different conductivities is not as significant when compared to a polymer compound. This can easily be explained by assumptions of Bowden and Ridler [190], claiming that the influence of the thermal conductivity on the hot spot temperature is evident. It is stated that a direct correlation exists if the ratio of the square roots of thermal conductivities of sliding partners is used as a factor for the flash temperature increase under comparable conditions. The thermal conductivity ratio of polymer towards steel is much higher than constantan to steel and therefore the effect is much stronger for polymer.

The fact that the deviation between calculations using the modified dynamic thermocouple theory and Furey's measurements is not as severe as in our present study can be ascribed to the relatively small difference of the thermal conductivities of the sliding bodies. In Furey's measurements the main thermoelectric influence is dominated by constantan. The influence of a steel counterbody with an ~8 times lower Seebeck-coefficient at RT in comparison to constantan is small. It is even smaller for different temperature gradients in both contact partners due to a stronger incline of the Seebeck-coefficient of constantan for higher temperatures. Results of Bowden and Ridler [190] for constantan on steel sliding are comparable and also reviewed by Furey [193]. Calculations using the modified dynamic thermocouple methodology could not be done for their results due to missing information and data. The comparison of melting points to experimentally obtained hot spot temperatures has to be specially addressed. In the publication of Bowden and Ridler [190] very close correlations are presented for other specimen materials, e.g. lead. Without additional data about measurement set-up, disc diameter, Seebeck-coefficients of the materials, standard deviations, testing times, input resistance of measurement equipment, CoF etc. correct estimations cannot be made and the discussion cannot be conclusive. However, assuming a slight under-estimation of the hot spot temperatures according to the new dynamic thermocouple methodology would imply that temperatures were above the melting temperature of the specimen. In recent publications Kalin and Vižintin claimed that the top layer of a metal sliding specimen can actually be in a melting state [280]. If melting of the metal is already given, an even higher temperature of the melt is presumed.

Summary:

- In the available literature no investigations were found which disagree with the modified measurement model.
- Former studies covered metal sliding pairs. Since the sliding partners and test set-ups used exhibit similar material characteristics, only insignificant improvements can be expected by application of the modified measurement model.

6.2.3.5. Results of Validation Tests and Influence of Different Load Cases

Figure 38 shows a typical behavior of sliding characteristics after initial contact between specimen and counterbody for PEEK-TC material. The maximum surface temperature measured via IR-camera shows a strong rise within the first few seconds, followed by a decrease after reaching a maximum at approximately 47 °C. The hot spot temperature, which was calculated according to modified thermocouple method presented in section 4.2.1.3, shows an even stronger increase and is after a short decrease constantly increasing. During further testing time this increase is still notional as it can be seen in e.g. Figure 39. While such behavior and an initial peak on the specimen bulk temperature were not described in literature, the explanation for polymeric compounds is simple. The specimen surface at initial contact is a mix of matrix and fillers. After a certain amount of time more and more fibers are in contact as they are the load carrying part of the compound. It was shown in section 6.2.1 that the measured FSRCA, which is mostly related to the fiber contact areas, shows a strong rise during the first approximately 20 s for similar conditions. As the FSRCA grows, the RCA of the matrix may reduce, resulting in an overall less RCA. If the same frictional energy must dissipate through smaller area this results in higher temperatures, here of the hot spot temperatures. Meanwhile the bulk temperature declines again due to fewer matrix material in the load-carrying contact and better heat dissipation by the SCF in contact.

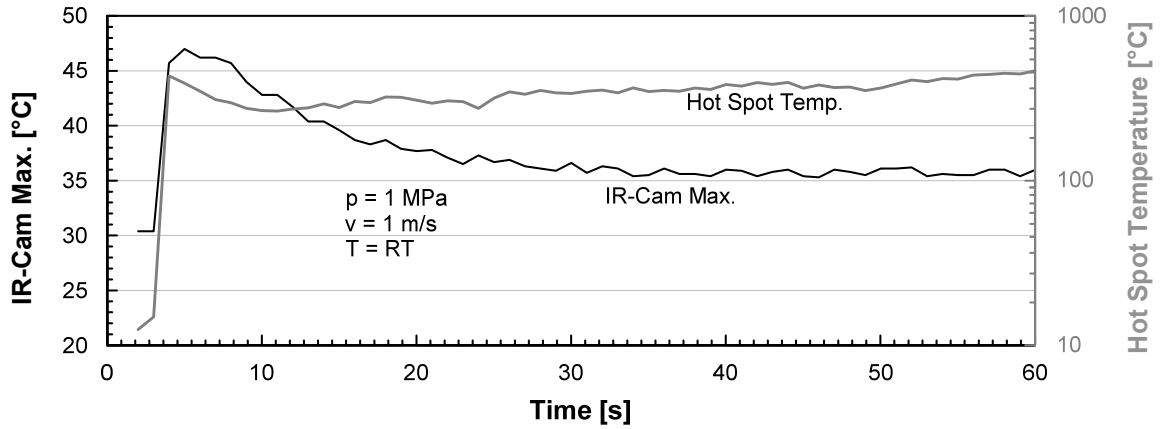

Figure 38: Start period temperature observations

Thermal gradients within a sliding specimen are easily described for homogeneous materials, e.g. steel. For compound materials matrix and fillers need to be described separately. The effect of local “overheating” of the matrix near the sliding contact results from high initial frictional heat insertion. It is followed by smaller heat intrusion, leading to lower bulk material temperature near the sliding contact. This can be ascribed to the even lower thermal conductivity of the matrix material in comparison to the compound which leads to a heat impound. The decline of temperature can be directly related to the load carried by the matrix as it decreases when more and more fibers start carrying the load.

For fibers in sliding contact some special behaviors must be considered to describe their thermal characteristics. Even with fibers in parallel alignment to the sliding direction always only a minor part of the surface can be in contact with the counterbody. For theoretical calculations, only the tip of the fiber is assumed to be in sliding contact while the rest of the fiber is in contact with the matrix. The diameter of a PAN fiber is described to be approximately 7 µm [281]. Via matrix burned and with OM analyzed PEEK-TC material an average fiber length of 104.5 µm ± 56.3 µm was determined. These dimensions lead to an aspect ratio of 1:60.7 for heat-gathering to heat emitting surface. If the matrix material supporting the fiber melts, the fiber is likely to be pulled out, leading to abrasive wear as a result of the thermal collapse. This condition was also investigated in the following experiments of combined tribological tests. Regarding the thermal gradient, the high aspect ratio indicates that the thermal gradient within the fiber must be extremely high. Due to the fibers’ high axial thermal conductivity of 100 W/mK and a good radial conductivity of 11 W/mK [59] it can be assumed that all fiber-matrix contact surfaces obtain comparable temperatures as the thermal conductivity of the matrix is low. Flash temperatures or hot spot temperatures are leveled out after a very short distance towards specimen heat sink as described by e.g. Ashby et al. [17]. This is also the reason why such temperatures are not measurable with an embedded thermocouple or similar technique.

As there is currently no other measurement technique available for proper comparison of the measured hot spot temperatures, they are compared by analytical calculations. During the validation tests several experiments with combined loading conditions were conducted, starting with 1 MPa at 1 m/s at RT. The results of three experiments in combination with known dimensions and parameters are used, assuming the compound is a homogeneous material while applying equations from Blok, Archard and Ashby as presented in section 2.1.9. The input parameters as well as the resulting flash temperatures are given in Table 12.

Parameter	Value	Obtained by
Sliding Speed	1 [m/s]	Defined
Normal Pressure	1 [MPa]	Defined
PEEK-TC Thermal Conductivity	0.86 [W/mK]	Compare section 5.1.2.4
100Cr6 Thermal Conductivity	44.6 [W/mK]	Literature [270, 278]
Friction Coefficient	0.46 [1]	Average from 3 tests between 6 and 10 [min] sliding time
Hot Spot Temperature	743 [°C]	
Flash Temperature Blok	207 [°C]	Calculated according to [17, 150, 151]. Equations presented in section 2.1.9
Flash Temperature Archard	772 [°C]	
Flash Temperature Ashby	805 °C	

Table 12: Temperature calculation input and output for PEEK-TC

For calculation according to Blok an extended equation was used, which allows to consider two different material characteristics for specimen and counterbody, and a flash temperature of 207 °C was calculated. Although this is much lower than the actual experimental results it is still reasonable as these equations only use the nominal contact area. The under-estimation using Blok's equation is also found in other publications [280].

Calculation according to Archard delivers a result of 772 °C for the flash temperature which is very close to the results according to Ashby's method which claims 805 °C for flash temperature. Here flash temperatures are assumed to be more or less equal to hot spot temperatures as explained above. The deviation of experimental to analytically calculated hot spots temperatures is within the range of 3.9 % for calculations according to Archard and 8.3 % for calculations according to Ashby. Taking into account many uncertainties of the validity of equations for inhomogeneous materials, the results for hot spot temperatures are in very good accordance, indicating a proper operation of the measurement.

Variations in normal pressure are given in Figure 39. The good correlation of hot spot temperature to CoF is evident. The changes of the normal load were conducted during the run, resulting in a drop of the hot spot temperature under increasing pressure. Additionally a rise of the temperature, monitored via IR-camera, can be observed at higher normal pressure.

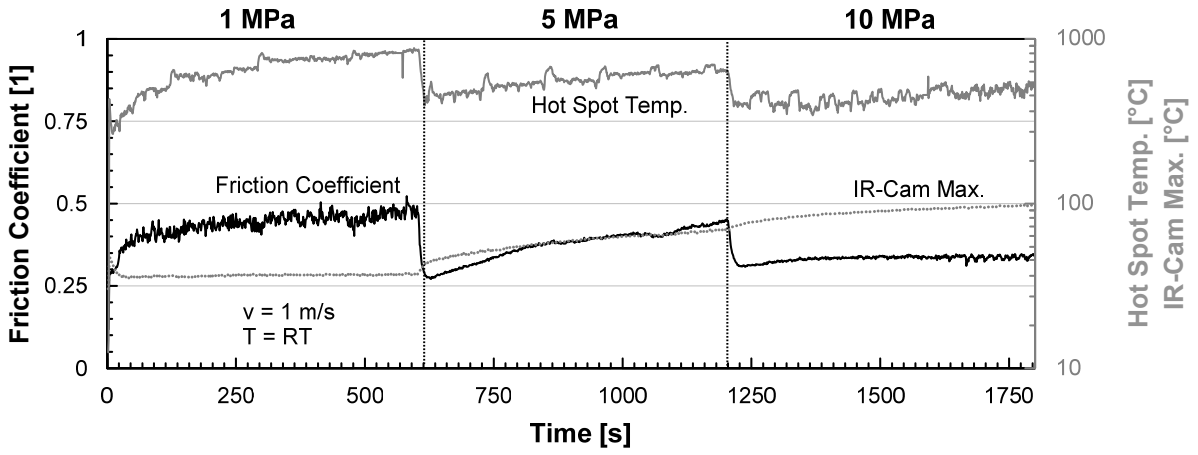

Figure 39: Pressure variation at temperature measurements validation

The drop in hot spot temperature can be explained by contact asperities as discovered by Archard [22]. At a higher normal pressure, elastic and also partly plastic deformations of the contact asperities increase, resulting in more asperities in contact. In the present investigations this leads to more area for frictional heat dissipation, which itself is also considerably lowered due to the drop in CoF. Correlations can be found if compared to results of FSRCA experiments from section 6.2.1.4, although testing times are varying. The FSRCA rises suddenly with every change in normal pressure while according to the new measurement the hot spot temperature drops. During the following load case the fiber-related contact area is lowered in the FSRCA experiments while the hot spot temperature increases at current discussed measurements. The FSRCA remains on a higher level which corresponds to the fact that more heat must be carried away. The total energy amount which must be dissipated by the specimen can be monitored indirectly by the maximum temperature observed via the IR-camera. It indicates that changes in the FSRCA, resulting from higher normal pressure, are dominating and outperform changes in the CoF, leading to a higher total energy amount produced during sliding. The total frictional energy can be calculated by multiplication of friction force with sliding distance, resulting in Joule [J]. If the power should be quoted, the sliding speed can be used instead of sliding distance, leading to Joule per second [J/s], what is equal to Watt [W].

The influence of different sliding velocities can be taken from Figure 40. It should be noted that experiments were conducted using three different speeds, namely 1, 3 and 5 m/s. Although the test was repeated several times, the speed of 5 m/s was found to be unsuitable for proper analyses, due to vibrations on the test rig resulting from resonance-frequencies. For the subsequent conducted, combined experiments this was changed by shifting resonance-frequencies to a less disturbing range.

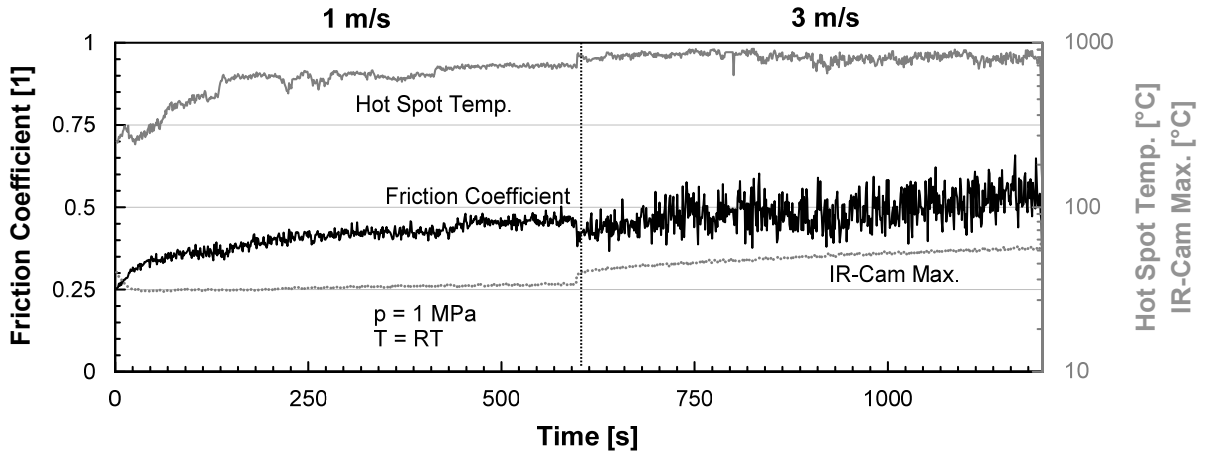

Figure 40: Velocity variation at temperature measurements validation

The behavior of the CoF between 1 and 2 m/s was found to be consistent throughout several repeats. In the example given, the CoF obtains no significant change except some noise on the signal, usually resulting from less uniform sliding conditions. Changes in frictional energy dissipated by heat are visible in maximum temperature observed by IR-camera. In section 6.2.1.4 a drop in FSRCA was determined, which is assumed to be similar to the phenomena observed in the present experiment. A smaller fiber contact area in combination with higher energy input to the sliding contact is believed to be responsible for the higher hot spot temperature, which is also found for 3 m/s sliding velocity. Again, the theory regarding total energy input and dissipation via frictional heat is in accordance with experimental results for hot spot temperature measurement with respect to FSRCA.

The results of a variation in counterbody temperature during the test, given in Figure 41, are again in accordance to the total frictional energy input, the FSRCA and measured hot spot temperatures. In section 6.2.1.4 it was shown that the FSRCA increases with rising counterbody temperatures, assumed to be caused by a softening of the polymer compound. As a result, more heat can be transported away from the sliding interface and therefore the hot spot temperature drops.

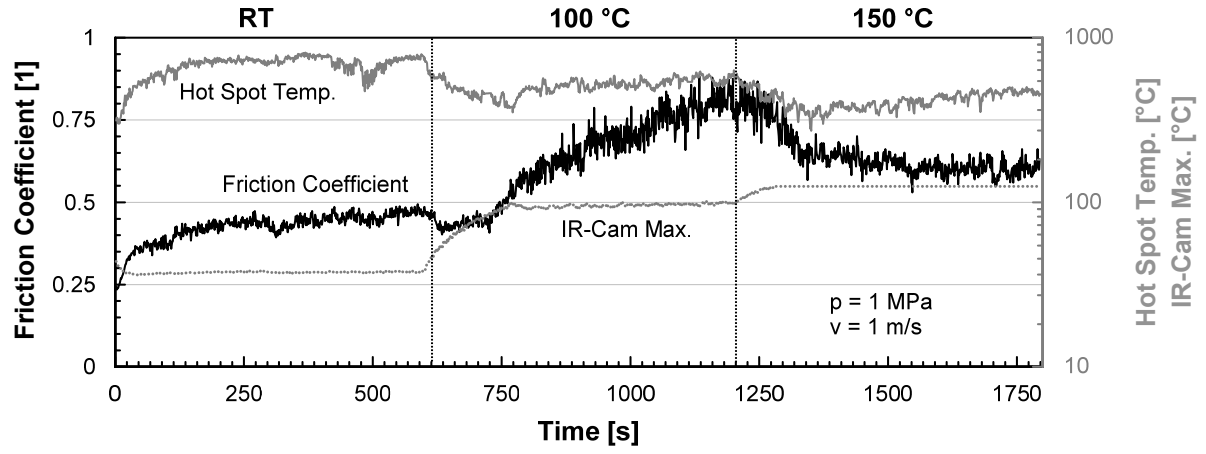

Figure 41: Temperature variation at temperature measurements validation

The total energy input to the pin is not observable by the IR-camera maximum values as the bulk temperature seems to be strongly dominated by the counterbody temperature, not showing any correlations to the CoF. The correlation between CoF and hot spot temperature is not obvious. This again indicates that the influence of the FSRCA has a greater impact on the hot spot temperature than the absolute CoF of the entire system.

Summary:

- Using the modified dynamic thermocouple method, in-situ determined values for hot spot temperatures correlate very well with calculations according to Archard [151] and Ashby et al. [17], showing deviations of 3.9 % and 8.3 %.
- Correlations between hot spot temperature, IR-camera temperature, CoF and total energy input could be established.
- A strong influence of the FSRCA on the hot spot temperature is expected.

6.2.3.6. Influence of Different Thermal Conductivities

Obviously thermal conductivities of specimen and counterbody exert a strong influence on temperatures within the sliding contact. The XC-2 material shows strongly anisotropic values regarding the thermal conductivity. For a normal fiber orientation (N) towards sliding interface a high thermal conductivity is given for the compound material.. For axial (A) and parallel (P) fiber orientation a good thermal distribution at the sliding contact was expected while the thermal flow towards the specimen heat sink is much worse. For the results given in Figure 42 individual tests were chosen, showing a similar CoF for better comparison. In this case the CoF for axial and parallel fiber orientation was approximately 0.5 for the last 30 % of the testing time while a normal orientated specimen showed a CoF of about 0.6.

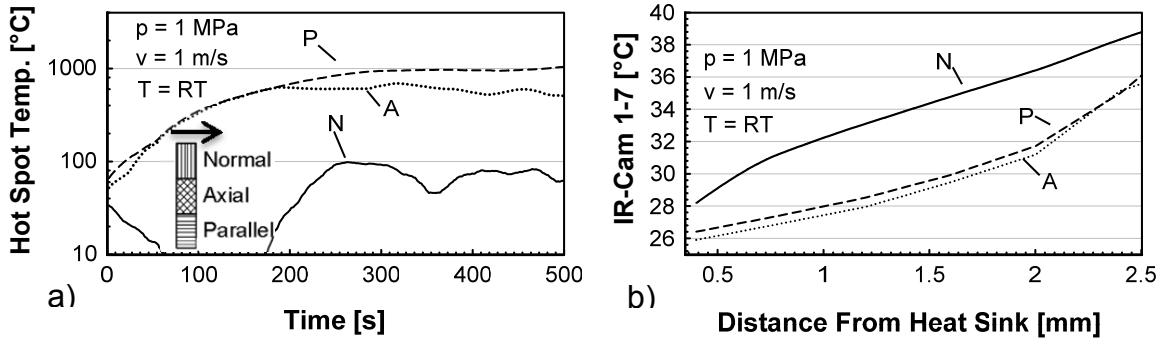

Figure 42: Temperatures for different thermal conductivities

The hot spot temperatures of both axial and parallel fiber orientated specimens are high and the thermal gradients from sliding contact towards heat sink are similar, showing the effect of thermal impound near the sliding contact as a bend in the

graph. The specimen with normal orientated, continuous fibers shows only temperatures slightly above the measured bulk surface temperature. This can be explained by the very high conductivity of the individual fibers, allowing all introduced heat to be transported away quickly. When compared to the PEEK-TC material it has to be pointed out that the fibers are continuous and the material has higher fiber volume content. Regarding this, an adiabatic isolation of the fibers does not take place for normal orientated fibers. This is also indicated by the via IR-camera measured temperatures. In Figure 42b the temperatures are given as a function of the distance from the specimen's heat sink, indicating better heat dissipation by normal orientated fibers since its outside temperature is higher. Figure 42a shows for the running-in period of the specimen with normal orientated fibers for the first ~150 s temperatures below RT or even 0 °C. During the first running-in, such effects can happen since the sliding contacts do not yet show a stable behavior due to strong wear mechanisms which are not yet stable. The specimens with normal orientated fibers are especially susceptible for such disturbances, because hot spot temperatures are comparably low, resulting in also small voltages. Such effects happened rarely during the experiments and usually disappeared after certain running-in time.

For variations in normal pressure, sliding velocity and counterbody temperature always at least 30 % of the time towards the end of a load case was used for average and standard deviation calculations. A similar behavior in CoF and maximum measured temperature by the IR-camera can be determined for variations of normal pressure, given in Figure 43. The maximum temperature observed by the IR-camera again indicates a higher total heat input due to frictional energy.

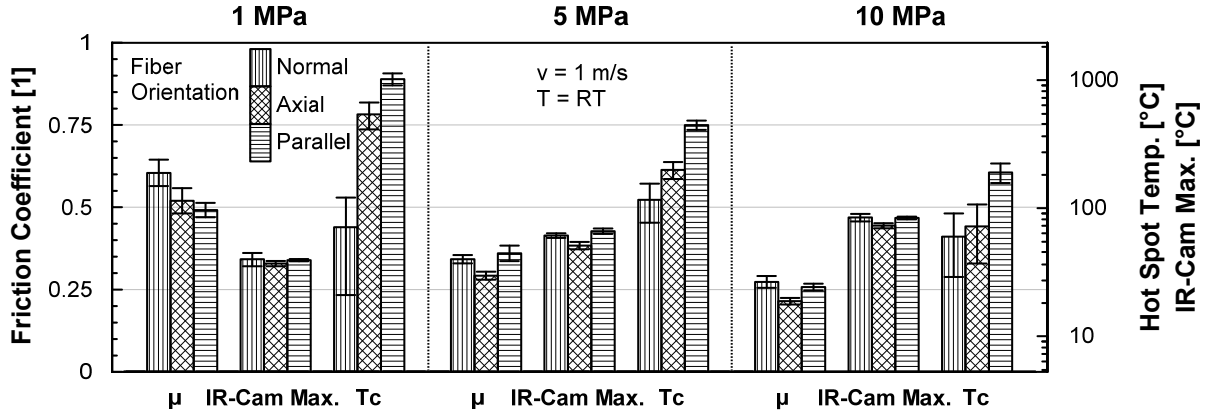

Figure 43: Pressure variation on different fiber orientations

While hot spot temperatures on specimen T_c for axial and parallel orientated fibers drop comparable to PEEK-TC pressure variation, the hot spot temperature of normal orientated fiber specimen remains stable at a low level. The hot spots temperature of normal orientated fibers cannot be lowered any further as it is already similar to bulk

material temperature. The drop for axial and parallel orientated fiber specimens is reasonable due to higher FSRCA, as expected by the theory of Ashby et al. [17] for higher normal pressures. Similar results were found for experimental FSRCA measurements. Higher FSRCA allows more heat dissipation and therefore lowers hot spot temperatures.

Variation in sliding velocity as shown in Figure 44 indicates lowered hot spot temperatures for axial and parallel fiber orientation while normal fiber orientation shows a strong increase. Again, the total thermal energy input rises at higher velocities on all specimens, as is visible in maximum IR-camera temperature.

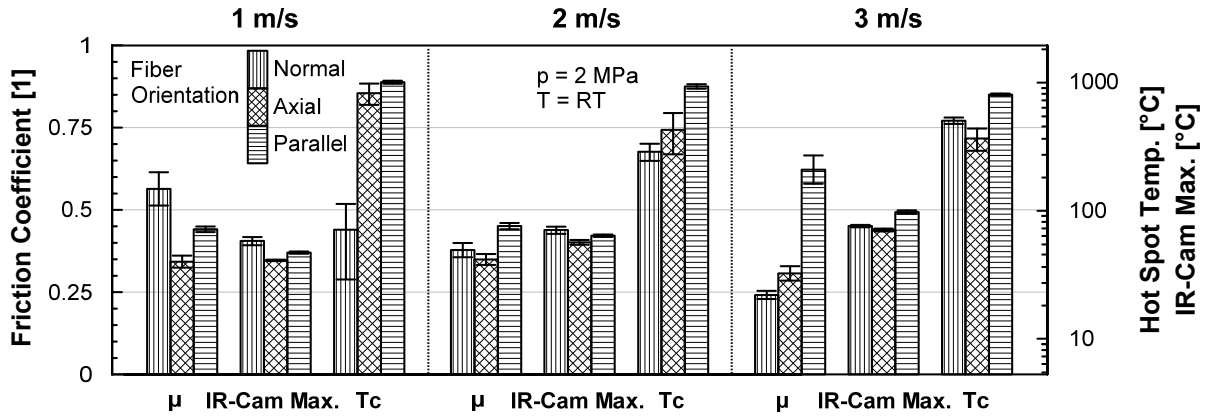

Figure 44: Velocity variation on different fiber orientations

The influence of CoF on the total thermal energy input is hardly noticeable and overpowered by the total energy input due to velocity increase as visible in maximum temperature observed via the IR-camera. The analysis of the increasing or decreasing hot spot temperatures for axial and parallel or normal fiber orientation, respectively, can be based on FSRCA in combination with directional E-modulus (compare Figure 22). For this analysis the results given in Figure 45 can also be taken into account, showing a similar behavior regarding hot spot temperatures when varying the counterbody temperature.

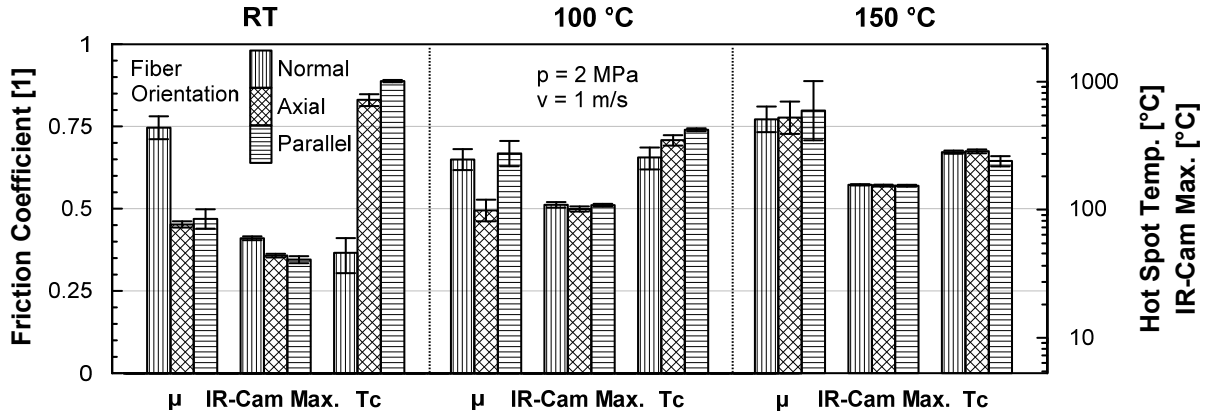

Figure 45: Counterbody temperature variation on different fiber orientations

CoF changes up to now were several times of smaller impact; so the increasing and decreasing behaviors of CoF for counterbody temperature and sliding velocity variation will not be compared.

An increasing amount of thermal energy is introduced to the sliding contact for variations in sliding velocity and counterbody temperature. The softening of the matrix material as a result of enhanced bulk temperature, observable by e.g. maximum IR-camera temperature, is obvious. For normal orientated fibers the influence of the softened matrix on stiffness is similar to other orientations as evident from Figure 22. It showed that the relative softening behavior is comparable. The E-modulus in the direction of normal orientated fibers is even at 300 °C much higher than for other orientations at RT. As long as the matrix can stabilize the fiber well on its sides it will still provide a higher stiffness than only the matrix between horizontally stacked fibers. According to the FSRCA theory by Ashby et al. [17] this results in only a slight possible increase regarding the FSRCA for normal orientated fibers. Subsequently this leads to higher hot spot temperatures as a surface of similar size must bear and transport higher a amount of frictional heat. In contrast, horizontally stacked fibers for axial and parallel fiber orientation may allow an increased FSRCA due to further softening of the matrix material near the sliding contact.

Summary:

- Fiber orientations and therefore thermal conductivities of the contact junctions exert massive influence on hot spot temperatures and total thermal characteristics of the specimen.
- Correlations of hot spot temperature, IR-camera temperature, CoF and total energy input could be determined under changing load conditions, comparable to PEEK-TC.
- The FSRCA is again expected to be a major influencing parameter on hot spot temperatures. Correlations in the behavior of hot spot temperatures with mechanical characteristics of specimen, which have a strong influence on the FSRCA, were evident.

6.2.3.7. A Closer Look at Fiber Hot Spot Temperatures

Experimental and simulative results were presented above in order to prove the validity of dynamic thermocouple temperature measurements for utilization in tribological applications with polymer compounds. The results show temperatures up to 1000 °C. Such high temperatures are usually not expected to occur on materials with a melting point of in our case 342.8 °C. Nevertheless, many correlations to other sys-

tem characteristics were evident and an enhanced calculation method and theoretical model were developed and proved. Also explanations were found as to how such high temperatures can exist as they are only expected for e.g. the fiber tips or small contact areas on the fibers. The polymer itself, of course, cannot withstand such high temperatures and can be in a molten state as it was also found for the top layers in metal specimens in literature [280]. It is assumed that molten polymer adheres to the counterbody ring as a progressing TFL, which could extend the theory of transferred and compressed particles for TFL evolution.

In order to provide some additional proof, several calculations were done according to the in section 2.1.9 earlier introduced equations of Blok, Archard and Ashby. Flash temperatures calculated according to Archard and Ashby et al. were presented, showing only a slight deviation of 3.9 % and 8.3 % if compared to experimental results.

Bowden and Ridler [190] explained in their work why such high temperatures are reasonable. Based on experimental observations they proposed following relationship:

Eq. 39:
$$\frac{(T_f - T_R)Material\ 1}{(T_f - T_R)\ Material\ 2} = \frac{\sqrt{Conductivity\ Material\ 1}}{\sqrt{Conductivity\ Material\ 2}} \quad [190]$$

This means that if two different specimens with different thermal conductivities are tribologically exposed under the same conditions with the same sliding characteristics, the flash temperature will be in direct relationship to the materials' thermal conductivities. In experiments such conditions are difficult to realize as the CoF must be similar for both materials under the same sliding conditions. If theoretically a steel on steel (100Cr6) sliding would take place and for example a flash temperature of 500 °C would occur, then a polymer specimen would be expected to have a ~7.3 times higher flash temperature of ~3650 °C. This is a comparably high expectation for flash temperatures of polymers, by far exceeding current experimental results. Although this assumption does not take into account the RCA or any other sliding characteristics, it claims that there is no obvious reason why a polymer material should obtain lower temperatures than metals under the same conditions. Regarding its thermal conductivities they should be even higher.

Summary:

- Measured hot spot temperatures can be explained in various ways.
- The TFL evolution may be due to melting polymer surface layers.

6.2.1. Measurement Techniques Application Notes

Enhanced measurement methods for FSRCA, TFL thickness, LFT and hot spot temperature determination were developed and investigated in several experiments within the above sections. It was established that it is not possible to determine a LFT by measuring the thickness of the film outside the sliding contact and give correlations to other sliding characteristics. FSRCAs measurement gave good indications under dry and lubricated conditions. Results were in accordance with the theory regarding EHD onset point and CoF as well as measured TFL thickness. The TFL thickness itself was proven by post-analysis WLP profilometry, showing some deviations in absolute values which were reasonable due to differences in measurement approaches and the TFL inhomogeneity. Additionally, profound research was done on the measurement of hot spot temperatures, using a modified theoretical model and calculation method. Especially these results were discussed and proved by various other calculations, simulations and theories, leading to a new understanding of tribological sliding contacts, expecting high volumetric contact temperatures for fiber reinforced polymer compounds.

In the following combined measurements all proved measurement methods are applied together in the same model test rig to demonstrate the use in basic research of the failure point of a material under tribological exposure and increasing load. Because the same material (PEEK-TC) is used, no further considerations were required. If the newly developed measurement methods are to be applied to another material or even test rig or application, several issues need to be discussed.

- For the FSRCA and hot spot temperature measurement the basic principle is relying on the electrically conductive fraction of the material. It has to be considered whether fibers are still the dominating conductive filler or if other fillers may disturb or even change the measurement itself.

- It is important to keep the disturbance of electromagnetic induction (EMI) low for the FSRCA and especially hot spot temperature measurements. Measurements are used in critical areas of low conductivity and very small voltages. Proper electrical grounding and shielding is absolutely necessary, although this would be challenging if the measurement technique shall be used in applications for e.g. surveillance.

- The TFL thickness measurement is comparably robust, but requires access to the counterbody surface where the TFL can be observed. In order to avoid the

need of a reference-algorithm, an additional sensor can be used. However, it has to be considered that confocal sensors are rather expensive. But besides a higher time resolution, its use would also offer the possibility to scan the whole TFL area instead of one single trace.

Summary:

- Enhanced measurement techniques could provide additional information to the sliding system. Some design issues should be considered.
- Since measurements are material dependent, it is important to ensure what exactly is measured.

6.3. Results of Investigation of Failure Mechanisms

The critical pressure x velocity (pv) factor of PEEK6 material for the combined measurements was found to be at a pressure of 16 MPa in combination with 8 m/s sliding speed. Figure 46 shows that with increasing pv the CoF drops after a first increase to a very low level. For the last three loading conditions a rise of CoF can be observed until a failure begins. Failure in this case is seen as severe wear up to a scale of several mm/h. At 12 MPa with 6 m/s sliding speed, the FSRCA starts to drop and the linear wear rate increases. The FSRCA is on more or less 100 % until this load case is applied, sometimes even showing values over 100 %. This can be caused by the high load and inconsistencies in filler distribution, leading to more contacting fibers on the surface in contrast to the reference-determination situation. The drops in FSRCA are found to be first taking place for increased velocity. This corresponds with earlier investigations. Contrary to earlier investigations in the measurement techniques validation section 6.2.1 changes in the FSRCA are also evident between 14 MPa and 16 MPa, indicating less fiber to steel surface contact area. Here the material failures can take place, which is also evident from the TFL thickness as this loading condition change leads to the most rapid increase in the TFL thickness.

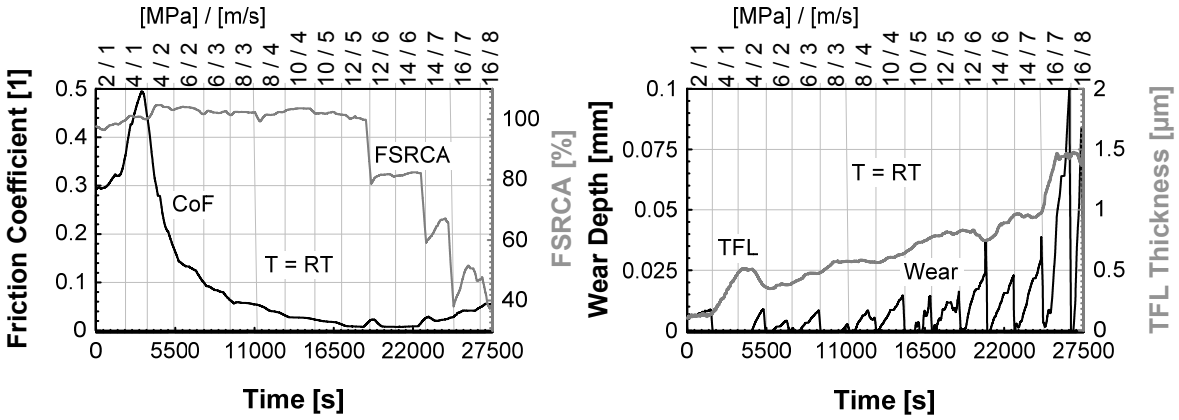

Figure 46: Combined measurements sliding characteristics 1/2

The TFL thickness is almost constantly rising with increased pv. Only at 4 MPa and 2 m/s a small decrease is noticed which is correlating to the drastically dropping CoF. A compaction of a TFL and reduction to a groove filling TFL seems to be reasonable for such a reduced CoF. The constant increase is also in good correlation to former experiments, as increased load always led to an incline in TFL thickness in validation experiments as well (compare section 6.2.1). A selection of the images, which were obtained automatically during the test is presented in Figure 47. Images with the counterbody ring not moving and the ring rotating at 1 m/s were taken. Those taken during rotation were found to have a better contrast. An increase in TFL thickness and coverage of counterbody steel surface with advanced testing time can be observed. Especially the last two images which were taken near and after the occurrence of material failure give a good impression of the significantly increased TFL thickness, also visible in the measurement.

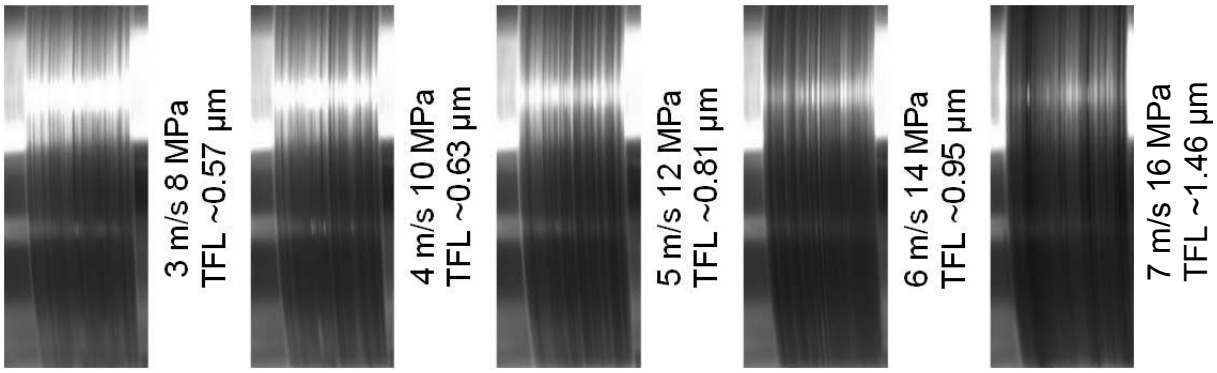

Figure 47: TFL observations

The surfaces of worn specimens and counterbody rings were later analyzed using SEM microscopy and WLP. On the worn specimen surface well aligned carbon fibers were found. Many of them seem to be very parallel to the sliding surface. Figure 48 shows that many fibers are visible in nearly their full length.

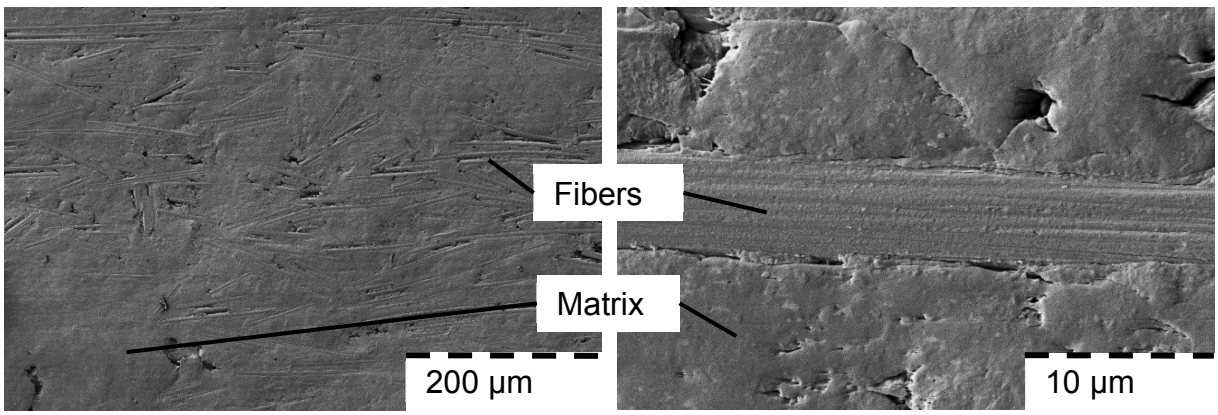

Figure 48: SEM analysis of worn specimen surface

Many fibers on the surface at a first view do not seem to correlate with the FSRCA measurement. Therefore also the counterbody ring must be investigated for complete understanding. Using WLP a surface roughness Ra of the TFL of 0.27 µm was determined, revealing a comparable roughness to the initial ring surface. In contrast Rz is given with 3.8 µm, what is considerably higher than 1.7 µm of the initial ring surface. Together with SEM images presented in Figure 49 it can easily be concluded that the FSRCA measurement is correct. It was stated above that the conducted RCA measurement refers to the FSRCA. If the counterbody is largely covered by a TFL it is possible that separation effects take place and fibers only come in contact with non-conductive TFL. The TFL thickness measurement supports this interpretation.

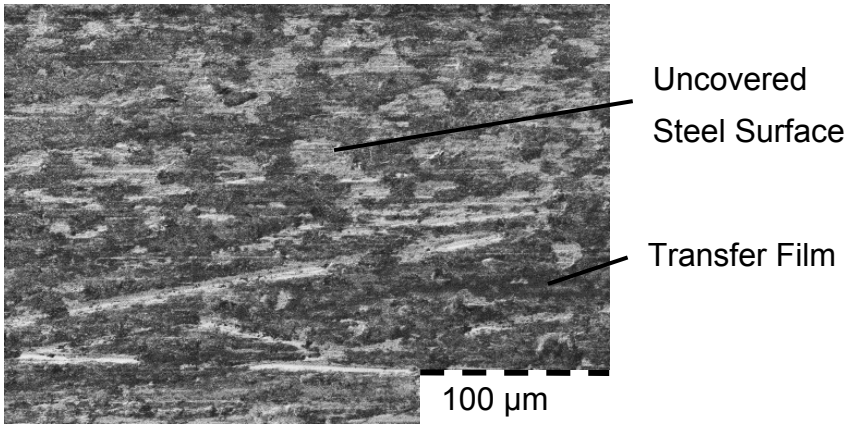

Figure 49: SEM surface observation of TFL

These results are not contrary to the former experiments (section 6.2.1). Although an increase of the TFL was evident for sand and glass blasted rings, asperities and large uncovered areas on the counterbody were found and a thick TFL was therefore not limiting the FSRCA measurement. Also a “lubricating” effect of polymer, as it was found in SEM results, did not take place in these former experiments. The frictional energy can easily be calculated as the quotient of friction force and sliding velocity Results of temperatures and total frictional energy input in Figure 50 show comparable starting points for the change in system characteristics towards failure at 12 MPa and 6 m/s. The lowered hot spot temperature behaves contrarily to the increasing maximum surface temperature observed using an IR-camera.

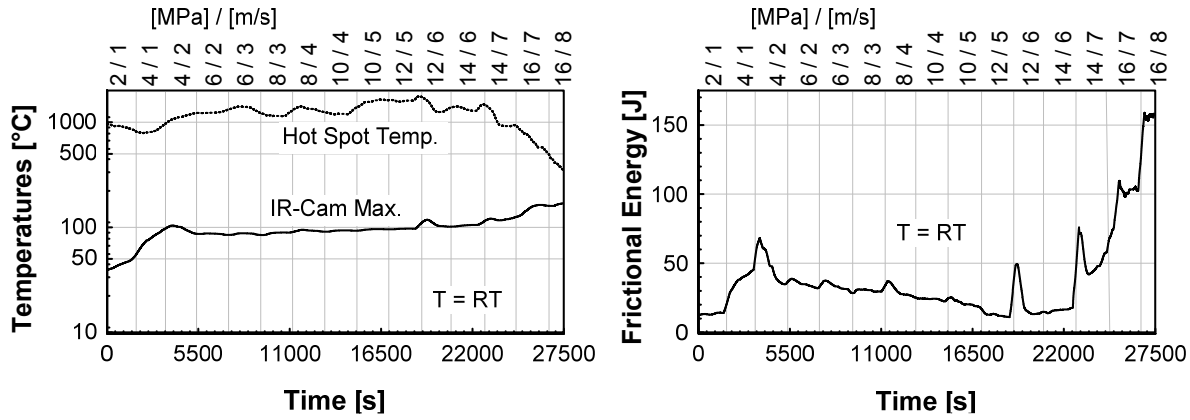

Figure 50: Combined measurements sliding characteristics 2/2

In section 6.2.3 the frictional energy was already expected to show a better correlation towards hot spot temperatures and specimen surface temperatures under changing load conditions than CoF alone. Although relative changes and tendencies are comparable, the massive rise of frictional energy towards the failure point is obvious. The investigation of frictional energy is probably an efficient way to determine sliding characteristics under changing load conditions, i.e. normal pressure and sliding velocity. The rise in total frictional energy is also visible in the maximum surface temperature IR-Cam Max. Hot spot temperatures incline slightly with increased sliding velocity and mostly remain stable or decline slightly with increased normal pressure. This is in accordance to former experiments in section 6.2.3. The decline of the hot spot temperatures at enhanced pv near the failure point is in accordance with the lower FSRCA and increased TFL thickness. The fibers are in less direct contact with the counterbody and the polymer matrix starts to carry an increasing amount of load. This results in an overall stronger heating, higher total frictional energy due to adhesion and abrasion effects of the polymer and, of course, further increasing TFL thickness. Especially the higher adhesion is visible in the SEM images in Figure 48 and Figure 49, giving the impression of rubbing polymer surfaces.

The increase of frictional energy near failure conditions as well as other obtained data leads to the impression that the failure is mainly caused by thermal collapse. Since the frictional energy is determined and thermal conductivities of both sliding partners are known, the share of energy can be calculated which each sliding partner has to discharge from the sliding interface. For this calculation it is assumed that 100 % of frictional energy is transferred into heat. The maximum thermal energy which can be absorbed by the specimen can also be calculated. The maximum possible dissipation is assumed if the polymer at the sliding interface is at its melting point of 343 °C. With 14 MPa and 7 m/s the frictional energy is still 38 % below the calculated maximum while for 16 MPa and 7 m/s it is already 4 % above the calculated maximum, indicat-

ing that the polymer on the specimen surface must be at its molten state. The significantly increased wear rate and rapidly enhanced TFL thickness can be interpreted as signs of this surface layer melting. The frictional energy input for the highest obtainable pv of 16 MPa and 8 m/s is already 30 % above the maximum thermal energy which can be dissipated through the specimen. Severe wear, a thick TFL, increasing specimen surface temperature, decreasing hot spot temperature and an especially strong decrease of FSRCA, indicating that the sliding characteristics are no longer fiber dominated, correspond to the material failure due to thermal collapse.

The alignment of many fibers on the surface layer can be explained by the melting of the specimen surface layer. For comparison a cross section of the specimen was prepared and observed via optical microscopy. Additionally, a cut parallel to the sliding surface was prepared. This cut was done in just a few 100 µm depth away from the sliding surface. Figure 51 shows that a fiber orientation took place during injection molding.

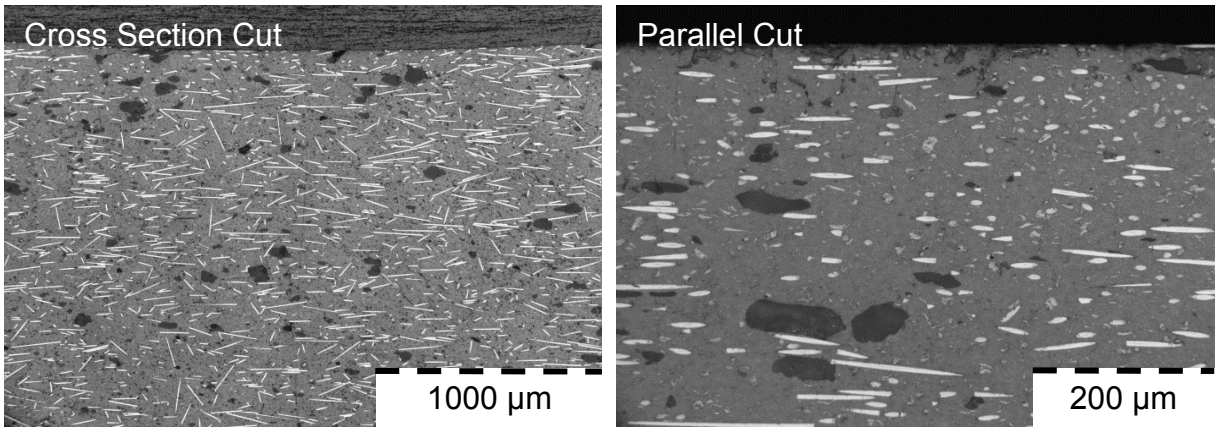

Figure 51: Cross section and surface parallel to the sliding surface of the specimen

Statistical analyses revealed that ~65 % of the fibers have an angle of less than 16 ° towards the sliding surface. Their average deviation in angle is 7.1 ° in sliding direction. When the polymer top layer has melted, another slight alignment of fibers, which are already aligned nearly parallel could perhaps take place. The observations of the cut parallel to the sliding surface in Figure 51 support this assumption, as obviously fewer fibers in similar good alignment are found in the entire parallel cut compared to the worn sliding surface given in Figure 48. This indicates a molten top layer on the sliding surface. In this condition the tribological behavior is dominated by the matrix. Compared to theoretical considerations regarding hot spot temperatures in section 6.2.3.7, very high temperatures on fiber contacts become even more reasonable.

The second experiment was conducted using a normal pressure of 14 MPa at 6 m/s sliding speed. At this load condition the sliding characteristics of the former experi-

ments were still stable with a low CoF, but the FSRCA already started to drop. After heating of the shaft a stepwise failure of the polymer specimen was found when the temperature reached 180 °C on the counterbody. The failure happened suddenly and several mm of wear occurred within a few seconds.

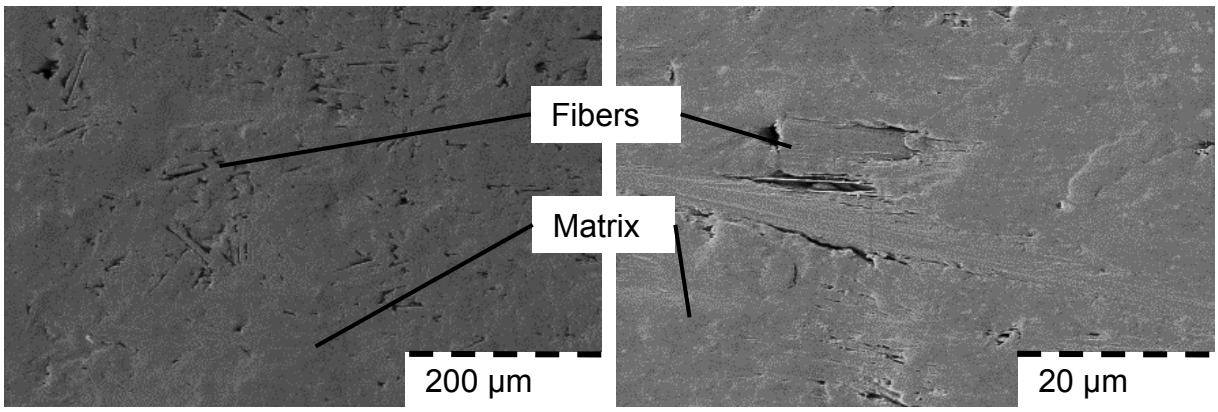

Figure 52: SEM analysis of worn pin surface for high counterbody temperature

The occurrence of a thermal collapse is evident from SEM morphologies of the worn specimen surface as shown in Figure 52. The rubbing effect of the polymer is obvious and also polymer-covered fibers are clearly visible. Although CoF and total frictional energy were still on a low level, a failure of material took place.

An explanation is found when counterbody and specimen surface temperatures, observed by the IR-camera, near the failure condition are compared. In the first experiment with increased pv a shaft temperature of 124 °C with a specimen surface temperature of 172 °C is found while in the increased counterbody temperature experiment 180 °C for counterbody and 214 °C for specimen surface is evident. The difference between counterbody and specimen temperature for both experiments is in a similar range as a result of thermal conductivities and the share of frictional heat which must be dissipated by both sliding partners. The FSRCA of the second experiment was only slightly lowered until the failure point and its influence on the hot spot temperature was less severe while the CoF remained stable. Although none of the measurements detected severe changes in sliding characteristics, a thermal collapse is evident. Contrary to increased pv it is based on macroscopic failure of the whole specimen due to counterbody heating and not a microscopic thermal collapse of the sliding surface as result of frictional heat. The influence on hot spot temperatures by the heated counterbody is considered to be small as these hot spots obtain much higher temperatures anyway. Nevertheless, the influence on the entire specimen temperature is evident, leading to a matrix softening at high temperatures and therefore to failure.

The experiments described above clarified several issues concerning the usability of enhanced measurement methods and also the design of sliding systems. It was demonstrated that materials failure due to frictional heating results in obvious changes of the sliding surface. **Less FSRCA in combination with lowered fiber hot spot temperatures and increasing TFL thickness resulted in a higher CoF, wear rate and total frictional energy.** However, the high counterbody temperature did not increase friction and wear up to a sudden breakdown. As long as frictional heat generation for PEEK6 material remained on a stable low level, the counterbody temperature had only a minor influence, unless matrix material was significantly softened. Therefore, from a design point of view, a cool sliding contact is less efficient than e.g. a near and efficient heat sink for the polymer compound bearing or coating.

7. Conclusions

Methodologies for enhanced measurements were developed, which allow accurate in-situ characterization of the frictional processes within sliding contacts, e.g. transfer film thickness, volumetric contact temperatures and real contact area between fibers and steel counterbody. The understanding of tribological mechanisms at different loading conditions can help in the development of polymer composites and optimized application layouts. Detailed conclusions can be drawn:

- While many in-situ measurement methods exist, especially for metal sliding pairs, only a few of them were found to be suitable for polymer tribology.
- FSRCA and TFL thickness measurement proved to be functional under various loading conditions in dry sliding while FSRCA determination also showed superior functionality under lubricated conditions. The differences to the state of the art for FSRCA measurement are explainable by the significantly different material characteristics.
- The use of a dynamic thermocouple for polymer tribology was successfully applied. In addition to a new theoretical model for the measurement method itself, new equations had to be established. Simulations as well as experiments were necessary for proof and measurement preparation. Also reasonable explanations for the experienced differences to other studies, using metal sliding pairs, had to be found to proof the new model. Hot spot temperatures of several materials with different mechanical and thermal properties showed strong correlations to other sliding characteristics under various loading cases.
- FSRCA determination as well as hot spot temperature measurement requires certain considerations of the tested specimen material regarding its conductive fraction for clear description of the measurements.
- Final experiments applying all enhanced measurement methods gave a profound insight on failure mechanisms under increasing pv and counterbody temperature. It was established, that the counterbody temperature has less influence than frictional energy introduction except thermal collapse of the matrix material due to counterbody heating sets in.
- The enhanced measurement methods were proved and show reliable and robust results. Although their application is demanding, a daily lab use is feasible. Adaption to applications is possible for monitoring and research issues.

8. Summary

This work covers the development of additional in-situ measurement techniques for tribological investigations. After a profound literature research, several essential parameters were selected for additional on-line characterization. These parameters include the real contact area of specimen and counterbody, the intermediate layer thickness between both sliding partners as well as the volumetric contact temperatures.

To find suitable methods for determination of the selected parameters, a review of measurement techniques in metal-tribology was conducted. For the determination of the real contact area between fiber and steel counterbody a resistive measurement method was applied. The selection of this method was based on the fact that the conductive fraction of a polymer in contact with the metallic counterbody is in direct relation to the electrical resistance through the sliding surface. The intermediate layer thickness was determined with a confocal distance measurement system for observation of the layer on the counterbody ring outside the sliding surface. For contact temperature, the only suitable solution found was the use of a dynamic thermocouple technique as all other methodologies had major drawbacks.

After successful implementation of all three measurement methods, the validation stage achieved good results for fiber to steel real contact area in both, dry and lubricated environments. Intermediate layer thickness measurements could only be proved for a dry sliding environment. The temperature measurement method had to be modified according to different thermal characteristics of the sliding partners in contrast to metal tribology. Additional experiments for suddenly contacting solids as well as a simulation of a tribological exposure similar to the test rig system were performed. It was found that the volumetric contact temperature on the counterbody ring is only slightly above average ring surface temperature near the sliding surface. Therefore a modified mathematical description of the dynamic thermocouple theory was created and used for measuring of the pin volumetric contact temperature. The modified model is based on different thermal gradients within specimen and counterbody and achieves reasonable results of measurement which could be successfully correlated with analytical calculations.

Although for each measurement method different load cases were examined individually, a combined test applying all enhanced measurements was conducted. With increasing velocity and pressure an increase in transfer film thickness could be monitored, together with decreasing fiber to steel real contact area. Together with de-

creasing hot spot temperatures, increasing overall counterbody temperature and frictional energy, they determined the evolving thermal collapse of the tribological system.

The demonstration of the additional measurement methods for failure mechanisms already shows the potential for upcoming studies. The developed measurement methods enable a cost efficient testing with profound information about tribological mechanisms within sliding contacts. The straight-forward implementation of the measurements in the model test rig can easily be adopted for industrial applications with regard to development or monitoring issues.

9. References

[1] DIN 50 323; Teil 1: Tribologie: Begriffe. (1988)

[2] Zum Gahr, K. H.: Tribologie: Reibung - Verschleiß - Schmierung. Naturwissenschaften, Vol. 72, Nr. 5 (1985), pp. 260–267

[3] Jost, H. P.: Committee on Tribology Report. Great Britain Ministry of Technology (1968)

[4] Lienhard, J. H.: The engines of our ingenuity an engineer looks at technology and culture.
URL: http://books.google.de/books?hl=de&id=qJdXre60T0kC&q=3500#v=snippet&q=3500&f=false. Retrieved 2013-05-31

[5] Urbakh, M. ; Meyer, E.: Nanotribology: The renaissance of friction. Nature Materials, Vol. 9, Nr. 1 (2010), pp. 8–10

[6] Bhushan, B.: Micro Nanotribology and Its Applications. Berlin: Springer, 1997. ISBN 0792343867

[7] Popov, V. L.: Kontaktmechanik und Reibung von der Nanotribologie bis zur Erdbebendynamik. Heidelberg: Springer, 2010. ISBN 9783642133022

[8] Gross, D. ; Hauger, W. ; Schnell, W.: Technische Mechanik. Berlin: Springer, 2004. ISBN 3540221670

[9] Persson, B. N. J.: Sliding friction: physical principles and applications, nanoscience and technology. 2nd. ed. Berlin: Springer, 2000. ISBN 3540671927

[10] Dowson, D.: History of tribology. London: Longman, 1979. ISBN 0582447666

[11] Prehn, R.: Tribologisch optimierte polymere Hochleistungsverbundwerkstoffe für den Einsatz unter abrasiven Bedingungen. Kaiserslautern, TU Kaiserslautern, Ph.D. Thesis 2006

[12] Steinhilper, W. ; Sauer, B.: Konstruktionselemente des Maschinenbaus 1: Grundlagen der Berechnung und Gestaltung von Maschinenelementen. Berlin: Springer, 2006. ISBN 3-540-22033-X

[13] Wiendl, S.: Mikrotribologische Untersuchungen an fettgeschmierten Wälzlagern. Hannover, Universiät Hannover, Ph.D. Thesis 2005

[14] Bowden, F. P. ; Tabor, D.: The friction and lubrication of solids. Oxford; New York: Clarendon Press; Oxford University Press, 2001. ISBN 0198507771

[15] Archard, J. F.: Contact and Rubbing of Flat Surfaces. Journal of Applied Physics, Vol. 24, Nr. 8 (1953), pp. 981-988

[16] Bowden, F. P. ; Tabor, D.: The Area of Contact between Stationary and between Moving Surfaces. Proceedings of the Royal Society of London. Series A, Mathematical and Physical Sciences, Vol. 169 (1939), pp. 391-413

[17] Ashby, M. F. ; Abulawi, J. ; Kong, H.S.: Temperature Maps for Frictional Heating in Dry Sliding. Tribology Transactions, Vol. 34, Nr. 4 (1991), pp. 577–587

[18] Buchner, B. ; Buchner, M. ; Buchmayr, B.: Determination of the real contact area for numerical simulation. Tribology International, Vol. 42, Nr. 6 (2009), pp. 897–901

[19] Krick, B. A. ; Vail, J. R. ; Persson, B. N. J. ; Sawyer, W. G.: Optical In Situ Micro Tribometer for Analysis of Real Contact Area for Contact Mechanics, Adhe-sion, and Sliding Experiments. Tribology Letters, Vol. 45, Nr. 1 (2011), pp. 185–194

[20] Spijker, P. ; Anciaux, G. ; Molinari, J.-F.: Dry Sliding Contact Between Rough Surfaces at the Atomistic Scale. Tribology Letters, Vol. 44, Nr. 2 (2011), pp. 279–285

[21] Váradi, K. ; Néder, Z. ; Friedrich, K. ; Flöck, J.: The real contact area between composite and steel surfaces in sliding contact. Composites Science and Technology, Vol. 61, Nr. 13 (2001), pp. 1853 – 1862

[22] Archard, J. F.: Elastic Deformation and the Contact of Surfaces. Nature, Vol. 172 (1953), pp. 918–919

[23] Czichos, H. ; Habig, K. H.: Tribologie-Handbuch: Reibung und Verschleiss. Wiesbaden: Vieweg + Teubner, 2007. ISBN 3834800171

[24] Schlecht, B.: Maschinenelemente 2: Lager und Getriebe. München: Addison Wesley in Pearson Education Deutschland, 2009. ISBN 9783827371461

[25] Holmberg, K. ; Ronkainen, H. ; Laukkanen, A. ; Wallin, K.: Friction and wear of coated surfaces — scales, modelling and simulation of tribomechanisms. Surface and Coatings Technology, Vol. 202, Nr. 4-7 (2007), pp. 1034–1049

[26] DIN 50 320; Verschleiß: Begriffe. (1979)

[27] Rabinowicz, E.: Friction and wear of materials. New York: Wiley, 1995. ISBN 0471830844

[28] Beitz, W. ; Grote, K.-H. ; Dubbel, H.: Taschenbuch für den Maschinenbau. Berlin: Springer, 2001. ISBN 3540677771

[29] Harraß, M.: Tribologische Beanspruchung ausgewählter technischer Kunststoffe und Roll-Gleit-Kontakt. Kaiserslautern: Institut f. Verbundwerkstoffe GmbH - Schriftenreihe, 2009

[30] DIN 50 321; Verschleiß: Meßgrößen. (1979)

[31] American Society for Testing and Materials: ASM International: Friction and Wear Testing: Source Book of Selected References from ASTM Standards and ASM Handbooks. West Conshohocken: ASM, 1997. ISBN 0871706172

[32] Steinhilper, W. ; Sauer, B.: Konstruktionselemente des Maschinenbaus 2: Grundlagen von Maschinenelementen für Antriebsaufgaben. Berlin: Springer, 2006. ISBN 3540296298

[33] Hertz, H.: Ueber die Berührung fester elastischer Körper. Journal für die reine und angewandte Mathematik (Crelle's Journal), Vol. 1882, Nr. 92 (1881), pp. 156–171

[34] Renouf, M. ; Massi, F. ; Fillot, N. ; Saulot, A.: Numerical tribology of a dry con-tact. Tribology International, Vol. 44, Nr. 7-8 (2011), pp. 834–844

[35] Lim, S. C. ; Ashby, M. F. ; Brunton, J. H.: Wear-rate transitions and their rela-tionship to wear mechanisms. Acta Metallurgica, Vol. 35, Nr. 6 (1987), pp. 1343–1348

[36] Molinari, J. F. ; Ortiz, M. ; Radovitzky, R. ; Repetto, E. A.: Finite-element model-ing of dry sliding wear in metals. Engineering Computations, Vol. 18, Nr. 3/4 (2001), pp. 592–610

[37] Põdra, P. ; Andersson, S.: Simulating sliding wear with finite element meth-od. Tribology International, Vol. 32, Nr. 2 (1999), pp. 71–81

[38] El Tobgy, M. S. ; Ng, E. ; Elbestawi, M. A.: Finite element modeling of ero-sive wear. International Journal of Machine Tools and Manufacture, Vol. 45, Nr. 11 (2005), pp. 1337–1346

[39] Bevill, S. L. ; Bevill, G. R. ; Penmetsa, J. R. ; Petrella, A. J. ; Rullkoetter, P. J.: Finite element simulation of early creep and wear in total hip arthroplas-ty. Journal of Biomechanics, Vol. 38, Nr. 12 (2005), pp. 2365-2374

[40] O'Brien, S. ; Luo, Y. ; Wu, C. ; Petrak, M. ; Bohm, E. ; Brandt, J.-M.: Predic-tion of backside micromotion in total knee replacements by finite element simulation. Proceedings of the Institution of Mechanical Engineers, Part H: Journal of Engineering in Medicine, Vol. 226, Nr. 3 (2012), pp. 235-245

[41] Kubica, M. ; Skoneczny, W. ; Jedrzejczyk, D.: Application of finite element method to analysis of tribological properties of aluminum oxide nano-layers. Proceedings of the Institution of Mechanical Engineers, Part J: Journal of Engineering Tribology, Vol. 227, Nr. 8 (2013), pp. 861–867

[42] Flöck, J.: Beitrag zur experimentellen und modellhaften Beschreibung der Gleitverschleissmechanismen kohlenstoffaserverstärkter Polyetheretherke-ton- (PEEK)-Verbunde. Kaiserslautern: Institur f. Verbundwerkstoffe GmbH, 2001. ISBN 3934930190

[43] DIN 50 322; Verschleiß: Kategorien der Verschleißprüfung. (1986)

[44] Breuer, U. P.: Lecture Notes: Civil Aircraft Composite Technology. Institut f. Verbundwerkstoffe GmbH Kaiserslautern, 2013/2014

[45] Deutsches Institut für Normung: Tribologie: Grundlagen, Prüftechnik, tribo-technische Konstruktionselemente ; Normen. Berlin: Beuth, 1990. ISBN 3410123539

[46] Friedrich, K. ; Schlarb, A. K.: Tribology of polymeric nanocomposites: Fric-tion and wear of bulk materials and coatings. Tribology and interface engi-neering series. Oxford: Elsevier Science, 2008. ISBN 9780444531551

[47] Saechtling, H. ; Oberbach, K.: Kunststoff-Taschenbuch: mit 223 Tafeln. München: Hanser, 2001. ISBN 3446216057

[48] Brostow, W. ; Kovačević, V. ; Vrsaljko, D. ; Whitworth, J.: Tribology of polymers and polymer-based composites. Journal of Materials Education, Vol. 32, Nr. 5-6 (2010), pp. 273–290

[49] Tewari, U. S. ; Sharma, S. K. ; Vasudevan, P.: Polymer Tribology. Journal of Macromolecular Science, Part C: Polymer Reviews, Vol. 29, Nr. 1 (1989), pp. 1-38

[50] Czichos, H. ; Feinle, P.: Tribologisches Verhalten von thermoplastischen gefüllten und glasverstärkten Kunststoffen: Kontaktdeformation, Reibung und Verschleiß, Oberflächenuntersuchungen. Bundesanst. für Materialprüfung, 1982

[51] Menges, G.: Werkstoffkunde Kunststoffe. München; Wien: Hanser, 2002. ISBN 3446212574

[52] Friedrich, K.: Microstructural efficiency and fracture toughness of short fiber/thermoplastic matrix composites. Composites Science and Technology, Vol. 22, Nr. 1 (1985), pp. 43-74

[53] Karger-Kocsis, J.: Instrumented impact fracture and related failure behavior in short- and long-glass-fiber-reinforced polypropylene. Composites Science and Technology, Vol. 48, Nr. 1-4 (1993), pp. 273-283

[54] Sanadi, A. R. ; Pigott, M. R.: Interfacial effects in carbon-epoxies Part 3: Toughness with short fibres. Journal of Material Science, Vol. 21, Nr. 5 (1986), pp. 1642-1646

[55] Karger-Kocsis, J. ; Friedrich, K.: Microstructural details and the effect of testing conditions on the fracture toughness of injection-moulded poly(phenylene-sulphide) composites. Journal of Material Science, Vol. 22, Nr. 3 (1987), pp. 947-961

[56] Zhang, G. ; Karger-Kocsis, J. ; Zou, J.: Synergetic effect of carbon nanofibers and short carbon fibers on the mechanical and fracture properties of epoxy resin. Carbon, Vol. 48, Nr. 15 (2010), pp. 4289–4300

[57] Piggott, M. R.: The effect of aspect ratio on toughness in composites. Journal of Materials Science, Vol. 9, Nr. 3 (1974), pp. 494–502

[58] Tanaka, K. ; Yamaguchi, M. ; Takahashi, T. ; Miyagawa, H. ; Yoshimatsu, H.: Electrical conductivity of poly(vinyl chloride) filled with PAN-based and pitch-based carbon short-fibers. Advanced Composite Materials, Vol. 4, Nr. 1 (1994), pp. 1-15

[59] Schuster, J. ; Heider, D. ; Sharp, K. ; Glowania, M.: Thermal conductivities of three-dimensionally woven fabric composites. Composites Science and Technology, Vol. 68, Nr. 9 (2008), pp. 2085–2091

[60] Strümpler, R. ; Glatz-Reichenbach, J.: Conducting Polymer Composites. Journal of Electroceramics, Vol. 3, Nr. 4 (1999), pp. 329-346

[61] Leute, U.: Kunststoffe und EMV: elektromagnetische Verträglichkeit mit leitfähigen Kunststoffen. Renningen: Expert-Verl., 2009. ISBN 9783816929536

[62] Jain, V. K.: Investigation of the wear mechanism of carbon-fiber reinforced acetal. Wear, Vol. 92, Nr. 2 (1983), pp. 279–292

[63] Friedrich, K. ; Zhang, Z. ; Schlarb, A. K.: Effects of various fillers on the sliding wear of polymer composites. Composites Science and Technology, Vol. 65, Nr. 15-16 (2005), pp. 2329-2343

[64] Guo, Q. B. ; Lau, K. T. ; Rong, M. Z. ; Zhang, M. Q.: Optimization of tribological and mechanical properties of epoxy through hybrid filling. Wear, Vol. 269, Nr. 1-2 (2010), pp. 13-20

[65] Voss, H. ; Friedrich, K.: On the wear behaviour of short-fibre-reinforced peek composites. Wear, Vol. 116, Nr. 1 (1987), pp. 1-18

[66] Lu, Z. P. ; Friedrich, K.: On sliding friction and wear of PEEK and its composites. Wear, Vol. 181-183, Nr. 2 (1995), pp. 624 – 631

[67] Zhang, G. ; Sebastian, R. ; Burkhart, T. ; Friedrich, K.: Role of monodispersed nanoparticles on the tribological behavior of conventional epoxy composites filled with carbon fibers and graphite lubricants. Wear, Vol. 292-293 (2012), pp. 176–187

[68] Zhang, G. ; Rasheva, Z. ; Schlarb, A. K.: Friction and wear variations of short carbon fiber (SCF)/PTFE/graphite (10Vol.%) filled PEEK: Effects of fiber orien-tation and nominal contact pressure. Wear, Vol. 268, Nr. 7-8 (2010), pp. 893-899

[69] Friedrich, K.: Advances in composite tribology. Amsterdam: Elsevier, 1993. ISBN 0444890793

[70] Friedrich, K. ; Lu, Z. ; Hager, A. M.: Recent advances in polymer composites' tribology. Wear, Vol. 190, Nr. 2 (1995), pp. 139–144

[71] Samyn, P. ; De Baets, P. ; Schoukens, G. ; Van Driessche, I.: Friction, wear and transfer of pure and internally lubricated cast polyamides at various testing scales. Wear, Vol. 262, Nr. 11-12 (2007), pp. 1433–1449

[72] Wu, C. L. ; Zhang, M. Q. ; Rong, M. Z. ; Friedrich, K.: Tensile performance improvement of low nanoparticles filled polypropylene composites. Composites Science and Technology, Vol. 62, Nr. 10-11 (2002), pp. 1327-1340

[73] Zhang, H. ; Zhang, Z. ; Friedrich, K. ; Eger, C.: Property improvements of in situ epoxy nanocomposites with reduced interparticle distance at high nanosilica content. Acta Materialia, Vol. 54, Nr. 7 (2006), pp. 1833-1842

[74] Ma, J. ; Mo, M.-S. ; Du, X.-S. ; Rosso, P. ; Friedrich, K. ; Kuan, H.-C.: Effect of inorganic nanoparticles on mechanical property, fracture toughness and toughening mechanism of two epoxy systems. Polymer, Vol. 49, Nr. 16 (2008), pp. 3510-3523

[75] Wetzel, B. ; Rosso, P. ; Haupert, F. ; Friedrich, K.: Epoxy nanocomposites – fracture and toughening mechanisms. Engineering Fracture Mechanics, Vol. 73, Nr. 16 (2006), pp. 2375-2398

[76] Wang, Q.-H. ; Xu, J. ; Shen, W. ; Xue, Q.: The effect of nanometer SiC filler on the tribological behavior of PEEK. Wear, Vol. 209, Nr. 1-2 (1997), pp. 316-321

[77] Wang, Q. ; Xue, Q. ; Shen, W. ; Zhang, J.: The Friction and Wear Properties of Nanometer ZrO2-Filled Polyetheretherketone. Journal of Applied Polymer Science, Vol 69, Nr. 1 (1998), pp. 135-141

[78] Zhang, M. Q. ; Rong, M. Z. ; Yu, S. L. ; Wetzel, B. ; Friedrich, K.: Improvement of Tribological Performance of Epoxy by the Addition of Irradiation Grafted Nano-Inorganic Particles. Macromolecular Materials and Engineering, Vol. 287, Nr. 2 (2002), pp. 111-115

[79] Wetzel, B. ; Haupert, F. ; Friedrich, K. ; Zhang, M. Q. ; Rong, M. Z.: Impact and Wear Resistance of Polymer Nanocomposites at Low Filler Content. Polymer Engineering & Science, Vol. 42, Nr. 9 (2002), pp. 1919-1927

[80] Zhang, G. ; Schlarb, A. K. ; Tria, S. ; Elkedim, O.: Tensile and tribological behaviors of PEEK/nano-SiO2 composites compounded using a ball milling technique. Composites Science and Technology, Vol. 68, Nr. 15-16 (2008), pp. 3073-3080

[81] Bahadur, S. ; Sunkara, C.: Effect of transfer film structure, composition and bonding on the tribological behavior of polyphenylene sulfide filled with nano particles of TiO2, ZnO, CuO and SiC. Wear, Vol. 258, Nr. 9 (2005), pp. 1411-1421

[82] Pegel, S. ; Pötschke, P. ; Petzold, G. ; Alig, I. ; Dudkin, S.M. ; Lellinger, D.: Dispersion, agglomeration, and network formation of multiwalled carbon nanotubes in polycarbonate melts. Polymer, Vol. 49, Nr. 4 (2008), pp. 974-984

[83] Noll, A.: Effektive Multifunktionalität von monomodal, bimodal und multimodal mit Kohlenstoff-Nanoröhren, Graphit und kurzen Kohlenstofffasern gefülltem Polyphenylensulfid. Kaiserslautern, Institut f. Verbundwerkstoffe GmbH, Ph.D. Thesis 2012

[84] Uetz, H. ; Wiedemeyer, J.: Tribologie der Polymere: Grundlagen u. Anwendungen in d. Technik ; Reibung, Verschleiß, Schmierung. München: Hanser, 1984. ISBN 3446140506

[85] Seipenbusch, M. ; Rothenbacher, S. ; Weber, A. P. ; Kasper, G.: Interparticle forces in Nanoparticle Agglomerates. Austria, Salzburg: Proceedings of European Aerosol Conference (2007)

[86] Bonnet, M.: Kunststoffe in der Ingenieuranwendung: verstehen und zuverlässig auswählen. Wiesbaden: Vieweg + Teubner, 2009. ISBN 9783834803498

[87] Domininghaus, H. ; Elsner, P. ; Eyerer, P. ; Hirth, T.: Kunststoffe Eigenschaften und Anwendungen. Berlin: Springer, 2008. ISBN 9783540724018

[88] Myshkin, N. K. ; Petrokovets, M. I. ; Kovalev, A. V.: Tribology of polymers: Adhesion, friction, wear, and mass-transfer. Tribology International, Vol. 38, Nr. 11-12 (2005), pp. 910–921

[89] Grellmann, W.: Kunststoffprüfung. München: Hanser, 2011. ISBN 9783446427228

[90] Yu, L.-G. ; Yang, S.-R.: Investigation of the transfer film characteristics and tribochemical changes of Kevlar fiber reinforced polyphenylene sulfide composites in sliding against a tool steel counterface. Thin Solid Films, Vol. 413, Nr. 1-2 (2002), pp. 98–103

[91] Bahadur, S.: The development of transfer layers and their role in polymer tribology. Wear, Vol. 245, Nr. 1-2 (2000), pp. 92–99

[92] Schwartz, C. J. ; Bahadur, S.: Studies on the tribological behavior and transfer film–counterface bond strength for polyphenylene sulfide filled with nanoscale alumina particles. Wear, Vol. 237, Nr. 2 (2000), pp. 261–273

[93] Mergler, Y. J. ; Schaake, R. P. ; Huis in't Veld, A. J.: Material transfer of POM in sliding contact. Wear, Vol. 256, Nr. 3-4 (2004), pp. 294–301

[94] Vande Voort, J. ; Bahadur, S.: The growth and bonding of transfer film and the role of CuS and PTFE in the tribological behavior of PEEK. Wear, Vol. 181-183, Nr. 1 (1995), pp. 212 – 221

[95] Feng, X. ; Lu, Z. ; Zhang, R.: Analysis of electron spectroscopy for chemical analysis of the transferred film formed during sliding wear for carbon fibre reinforced polyetheretherketone and its composites. Journal of Materials Science, Vol. 34, Nr. 14 (1999), pp. 3513–3524

[96] Jintang, G.: Tribochemical effects in formation of polymer transfer film. Wear, Vol. 245, Nr. 1-2 (2000), pp. 100–106

[97] Cong, P. ; Xiang, F. ; Liu, X. ; Li, T.: Morphology and microstructure of polyamide 46 wear debris and transfer film: In relation to wear mechanisms. Wear, Vol. 265, Nr. 7-8 (2008), pp. 1100–1105

[98] Smurugov, V. A.: On the thickness and effectiveness of friction transfer films. Soviet Journal of Friction and Wear, Vol. 9, Nr. 1 (1988), pp. 159–162

[99] Sebastian, R. ; Noll, A. ; Zhang, G. ; Burkhart, T. ; Wetzel, B.: Friction and wear of PPS/CNT nanocomposites with formation of electrically isolating transfer films. Tribology International, Vol. 64 (2013), pp. 187–195

[100] Chang, L. ; Friedrich, K. ; Ye, L.: Study on the Transfer Film Layer in Sliding Contact Between Polymer Composites and Steel Disks Using Nanoindentation. Journal of Tribology, Vol. 136 (2014), pp. 021602-1 – 021602-12

[101] Friedrich, K. ; Chang, L.: On Sliding Wear of Nanoparticle Modified Polymer Composites. Italy, Ischia: Proceedings of AIP Converence (2010), Vol. 1255, pp. 240-242. ISBN 0735408041

[102] Yang, E.-L. ; Hirvonen, J.-P. ; Toivanen, R. O.: Effect of temperature on the transfer film formation in sliding contact of PTFE with stainless steel. Wear, Vol. 146, Nr. 2 (1991), pp. 367-376

[103] Váradi, K. ; Néder, Z. ; Friedrich, K. ; Flöck, J.: Contact and thermal analysis of transfer film covered real composite-steel surfaces in sliding contact. Tribology International, Vol. 33, Nr. 11 (2000), pp. 789-802

[104] Ramachandra, S. ; Ovaert, T. C.: The effect of controlled surface topographical features on the unlubricated transfer and wear of PEEK. Wear, Vol. 206, Nr. 1-2 (1997), pp. 94–99

[105] Marcus, K. ; Ball, A. ; Allen, C.: The effect of grinding direction on the nature of the transfer film formed during the sliding wear of ultrahigh molecular weight polyethylene against stainless steel. Wear, Vol. 151, Nr. 2 (1991), pp. 323-336

[106] Jia, J. ; Chen, J. ; Zhou, H. ; Hu, L. ; Chen, L.: Comparative investigation on the wear and transfer behaviors of carbon fiber reinforced polymer composites under dry sliding and water lubrication. Composites Science and Technology, Vol. 65, Nr. 7-8 (2005), pp. 1139–1147

[107] Scherge, M. ; Kramlich, J. ; Böttcher, R. ; Hoppe, T.: Running-in due to material transfer of lubricated steel/PA46 (aliphatic polyamide) contacts. Wear, Vol. 301, Nr. 1-2 (2013), pp. 758-762

[108] Friedrich, K. ; Flöck, J. ; Váradi, K. ; Néder, Z.: Experimental and numerical evaluation of the mechanical properties of compacted wear debris layers formed between composite and steel surfaces in sliding contact. Wear, Vol. 251, Nr. 1-12 (2001), pp. 1202 – 1212

[109] Eiss, N. S. ; Wood, K. C. ; Herold, J. A. ; Smyth, K. A.: Model for the Transfer of Polymer to Rough, Hard Surfaces. Journal of Lubrication Technology, Vol. 101, Nr. 2 (1979), pp. 212-218

[110] Kopeliovich, D.: General classification of lubricants. URL: http://www.substech.com/dokuwiki/doku.php?id=classification_of_lubricants. Retrieved 2013-06-20

[111] Flannery, M. ; Jones, E. ; Birkinshaw, C.: Analysis of wear and friction of total knee replacements part II: Friction and lubrication as a function of wear. Wear, Vol. 265, Nr. 7-8 (2008), pp. 1009–1016

[112] Chen, B. ; Wang, J. ; Yan, F.: Friction and Wear Behaviors of Several Polymers Sliding Against GCr15 and 316 Steel Under the Lubrication of Sea Water. Tribology Letters, Vol. 42, Nr. 1 (2011), pp. 17–25

[113] Wang, J. ; Yan, F. ; Xue, Q.: Friction and Wear Behavior of Ultra-High Molecular Weight Polyethylene Sliding Against GCr15 Steel and Electroless Ni–P Alloy Coating Under the Lubrication of Seawater. Tribology Letters, Vol. 35, Nr. 2 (2009), pp. 85–95

[114] Yamada, Y. ; Tanaka, K.: Effect of the degree of crystallinity on the friction and wear of poly(ethylene terephthalate) under water lubrication. Wear, Vol. 111, Nr. 1 (1986), pp. 63–72

[115] Kadokawa, J.: Ionic Liquids - New Aspects for the Future. InTech, 2013. ISBN 978-953-51-0937-2

[116] Stribeck, R.: Die wesentlichen Eigenschaften der Gleit und Rollenlager. VDI-Zeitschrift, Vol. 46, Nr. 36, 37, 38 (1902), pp. 1341-1348, 1432-1438; 1463-1470

[117] Hild, W.: Tribologische Untersuchung an Mikrosystemen: Einfluss der Benetzbarkeit. Ilmenau, TU Ilmenau, Ph.D. Thesis 2005

[118] Roberts, E. W.: Space tribology: Its role in spacecraft mechanisms. Journal of Physics: Applied Physics, Vol. 45, Nr. 50 (2012), pp. 1-17

[119] Narayan R.: Biomedical Materials. Boston: Springer US, 2009. ISBN 978-0-387-84871-6

[120] Bhushan, B.: Modern tribology handbook, Mechanics and materials science series. Boca Raton: CRC Press, 2001. ISBN 0849384036

[121] Wang, Y. Q. ; Li, C.: Numerical Analysis of Hydrodynamic Lubrication on Water-Lubricated Rubber Bearings. Advanced Materials Research, Vol. 299-300 (2011), pp. 12-16

[122] Müser, M. H.: Lubricants under high local pressure: Liquids act like solids. Materialwissenschaft und Werkstofftechnik, Vol. 35, Nr. 10-11 (2004), pp. 603-609

[123] Zilberman, S. ; Persson, B. N. J. ; Nitzan, A.: Theory and simulations of squeeze-out dynamics in boundary lubrication. The Journal of Chemical Physics, Vol. 115, Nr. 24 (2001), pp. 11268-11277

[124] Zilberman, S. ; Persson, B. ; Nitzan, A. ; Mugele, F. ; Salmeron, M.: Boundary lubrication: Dynamics of squeeze-out. Physical Review, Vol. 63, Nr. 5 (2001), pp. 055103-1 - 055103-4

[125] Sfantos, G. K. ; Aliabadi, M. H.: Total hip arthroplasty wear simulation using the boundary element method. Journal of Biomechanics, Vol. 40, Nr. 2 (2007), pp. 378-389

[126] Cheng, H. S.: Mixed Lubrication and Lubricated Wear. Proceedings of the 19th Leeds-Lyon Symposium on Tribology (1993). Thin Films in Tribology, Vol. 25. ISBN 9780444897893

[127] Wen, S. ; Luo, J. ; Hu, Y.: Physics and Chemistry of Micro-Nanotribology. West Conshohocken: ASTM, 2008. ISBN 978-0-8031-7006-3

[128] Martini, A. ; Zhu, D. ; Wang, Q.: Friction Reduction in Mixed Lubrication. Tribology Letters, Vol. 28, Nr. 2 (2007), pp. 139–147

[129] Hu, Y.-Z. ; Zhu, D.: A Full Numerical Solution to the Mixed Lubrication in Point Contacts. Journal of Tribology, Vol. 122, Nr. 1 (2000), pp. 1-9

[130] Zhu, D. ; Hu, Y.-Z.: A Computer Program Package for the Prediction of EHL and Mixed Lubrication Characteristics, Friction, Subsurface Stresses and Flash Temperatures Based on Measured 3-D Surface Roughness. Tribology Transactions, Vol. 44, Nr. 3 (2001), pp. 383–390

[131] Zhu, D. ; Hu, Y.-Z.: Effects of Rough Surface Topography and Orientation on the Characteristics of EHD and Mixed Lubrication in Both Circular and Elliptical Contacts. Tribology Transactions, Vol. 44, Nr. 3 (2001), pp. 391–398

[132] Liu, Y. ; Wang, Q. J. ; Zhu, D. ; Wang, W. ; Hu, Y.: Effects of Differential Scheme and Viscosity Model on Rough-Surface Point-Contact Isothermal EHL. Journal of Tribology, Vol. 131, Nr. 4 (2009), pp. 044501-044501-5

[133] Dauber, O.: Elastohydrodynamische Rollreibung in Stahl-Keramik-Kontakten. Karlsruhe, Institut für Maschinenkonstruktionslehre und Kraftfahrzeugbau, Universität Karlsruhe (TH), Ph.D. Thesis 2001

[134] Van Leeuwen, H. J. ; Schouten, M. J. W.: Die Elastohydrodynamik: Geschichte und Neuentwicklung. VDI Berichte, Nr. 1207 (1995)

[135] Goodyer, C. E.: Adaptive numerical methods for elastohydrodynamic lubrication. Leeds, The University of Leeds, Ph.D. Thesis 2001

[136] Dowson, D. ; Higginson, G. R.: The effect of material properties on the lubrication of elastic rollers. Journal of Mechanical Engineering Science, Vol. 2, Nr. 3 (1960), pp. 188–194

[137] Dowson, D. ; Higginson, G. R.: A numerical solution to the elastohydrodynamic problem. Journal of Mechanical Engineering Science, Vol. 1, Nr. 1 (1959), pp. 6–15

[138] Křupka, I. ; Hartl, M.: Experimental Study of Microtextured Surfaces Operating Under Thin-Film EHD Lubrication Conditions. Journal of Tribology, Vol. 129, Nr. 3 (2007), pp. 502-508

[139] Mohrenstein-Ertel, A.: Die Berechnung der hydrodynamischen Schmierung gekrümmter Oberflächen unter hoher Belastung und Relativbewegung. Düsseldorf: Verein Deutscher Ingenieure, 1984. ISBN 3181415014

[140] Dowson, D.: Elastohydrodynamic lubrication, International series on materials science and technology. New York: Pergamon Press, 1977. ISBN 0080213030

[141] Sperrfechter, T.: Keramische Bauteile im elastohydrodynamischen Kontakt. IKM-Schriftenreihe: IKM 024, 1998

[142] Dowson, D.: Elastohydrodynamics. Proceedings of the Institution of Mechanical Engineers, Vol. 182, Nr. PT 3A (1968), pp. 151–167

[143] Wisniewski, M.: Elastohydrodynamische Schmierung: Grundlagen und Anwendungen ; mit 12 Tabellen. Renningen-Malmsheim: Expert-Verl., 2000. ISBN 3816917453

[144] Komanduri, R.: Machining and Grinding: A Historical Review of the Classical Papers. Applied Mechanics Reviews, Vol. 46, Nr. 3 (1993), pp. 80-132

[145] Kennedy, F. E.:Surface Temperature Measurement. In: ASM International: Friction and Wear Testing: Source Book of Selected References from ASTM Standards and ASM Handbooks. West Conshohocken: ASM, 1992. ISBN 0871703807, pp. 438-444.

[146] Hao, Y. S. ; Zhang, B. G. ; Peng, B.: Analysis of Tribological Characteristics between Plastic and Steel Helical Gear. Advanced Materials Research, Vol. 383-390 (2011), pp. 2097-2102

[147] Jie, L. ; Lei, Z. ; Qi, Z.: Comparison and Analysis on Different Finite Element Models of Gear Interfacial Contact Temperature. China, Sanya: Proceeding of ICCMS 2 (2010), pp. 132–136

[148] Jie, L. ; Zhang Lei ; Zhao Qi: Finite element modeling and analysis on interfacial contact temperature of gears based on ANSYS. China, Wenzhou: Proceedings of CAID & CD (2009), pp. 668-673

[149] Wu, L. ; Wen, Z. ; Li, W. ; Jin, X.: Thermo-elastic–plastic finite element analysis of wheel/rail sliding contact. Wear, Vol. 271, Nr. 1-2 (2011), pp. 437-443

[150] Blok, H.: The flash temperature concept. Wear, Vol. 6, Nr. 6 (1963), pp. 483-494

[151] Archard, J. F.: The temperature of rubbing surfaces. Wear, Vol. 2, Nr. 6 (1959), pp. 438–455

[152] Anton Paar OptoTec GmbH. URL: http://www.anton-paar.com/Tribologie-Messzelle-%E2%80%94-Reibung-Schmierung-und-Verschlei%C3%9F-messen/Rheometer/60_Corporate_de?product_id=66#parent=45. Retrieved 2013-06-20

[153] Werner Stehr Tribologie. URL: http://www.werner-stehr-tribologie.com/. Retrieved 2013-06-18

[154] Stachowiak, G. W. ; Batchelor, A. W. ; Stachowiak, G.: Experimental methods in tribology. Amsterdam: Elsevier, 2004. ISBN 9780444515896

[155] D02 Committee: Test Method for Measurement of Extreme-Pressure Properties of Lubricating Fluids (Four-Ball Method). ASTM D2783 - 03 (2009)

[156] D02 Committee: Test Method for Measurement of Extreme-Pressure Properties of Lubricating Fluids (Timken Method). ASTM D2782-02 (2008)

[157] G02 Committee: Test Method for Ranking Resistance of Plastics to Sliding Wear Using Block-on-Ring Wear Test--Cumulative Wear Method. ASTM G176 - 03 (2009)

[158] G02 Committee: Test Method for Wear Testing with a Pin-on-Disk Apparatus. ASTM G99 - 05 (2010)

[159] DIN 51834-1; Prüfung von Schmierstoffen - Tribologische Prüfung im translatorischen Oszillations-Prüfgerät – Teil 1: Allgemeine Arbeitsgrundlagen. (2010)

[160] G02 Committee: Test Method for Linearly Reciprocating Ball-on-Flat Sliding Wear. ASTM G133 - 05 (2010)

[161] D02 Committee: Test Method for Determining Extreme Pressure Properties of Solid Bonded Films Using a High-Frequency, Linear-Oscillation (SRV) Test Machine. ASTM D7217 - 11 (2011)

[162] D02 Committee: Test Method for Measuring Friction and Wear Properties of Extreme Pressure (EP) Lubricating Oils Using SRV Test Machine. ASTM D6425 - 11 (2011)

[163] Dillmann, R.: Lecture Notes: Robotik III, Sensoren in der Robotik. Institut für Prozessrechentechnik, Automation und Robotik. Technische Universität Karlsruhe, 2013

[164] Rose, T.: Lecture Notes: Sensortechnik 1-Grundlagen und Anwendung von Sensoren. FH Münster, 2010

[165] Sautter, D. ; Weinerth, H.: Lexikon Elektronik und Mikroelektronik. Berlin: Springer, 1993. ISBN 978-3-642-63431-4

[166] Barber, A.: Handbook of noise and vibration control. Oxford: Elsevier Advanced Technology, 1992. ISBN 1856170799

[167] Hoffmann, K.: An Introduction to Measurements using Strain Gages. Darmstadt: Hottinger Baldwin Messtechnik GmbH, 1989

[168] Hottinger Baldwin Messtechnik GmbH. URL: http://www.hbm.com. Retrieved 2013-06-19

[169] ME-Meßsysteme GmbH. URL: www.me-systeme.de. Retrieved 2013-06-19

[170] Loadstar Sensors. URL: http://www.loadstarsensors.com/. Retrieved 2013-06-19

[171] Rocha, J. G. ; Mendez, S. L.: Sensors: Focus on Tactile Force and Stress Sensors: InTech, 2008. ISBN 978-953-7619-31-2

[172] Lautzenhiser, T. V.: Laser force-measuring system biasing, Patent: US 4155251 A. (1979)

[173] ChenYang Technologies GmbH & Co. KG. URL: http://www.chenyang-ism.com/EddyCurrent.htm. Retrieved 2013-06-19

[174] Bayerl, T. ; Schlarb, A. K.: Welding of tribologically optimized polyether-ether-ketone films with metallic substrates. Tribology International, Vol. 43, Nr. 5-6 (2010), pp. 1175–1179

[175] Shi, G. ; Zhang, M. Q. ; Rong, M. Z. ; Wetzel, B. ; Friedrich, K.: Friction and wear of low nanometer Si3N4 filled epoxy composites. Wear, Vol. 254, Nr. 7-8 (2003), pp. 784–796

[176] Gåhlin, R. ; Larker, R. ; Jacobson, S.: Wear volume and wear distribution of hydraulic motor cam rollers studied by a novel atomic force microscope technique. Wear, Vol. 220, Nr. 1 (1998), pp. 1–8

[177] MicroProf 100 Datasheet, FRT Fries Research & Technology GmbH 2013

[178] Reinicke, R. ; Haupert, F. ; Friedrich, K.: On the tribological behaviour of selected, injection moulded thermoplastic composites. Composites Part A: Applied Science and Manufacturing, Vol. 29, Nr. 7 (1998), pp. 763 – 771

[179] Ditrói, F. ; Takács, S. ; Tárkányi, F. ; Corniani, E. ; Smith, R. W. ; Jech, M. ; Wopelka, T.: Sub-micron wear measurement using activities under the free handling limit. Journal of Radioanalytical and Nuclear Chemistry, Vol. 292, Nr. 3 (2012), pp. 1147–1152

[180] Scherge, M. ; Pöhlmann, K. ; Gervé, A.: Wear measurement using radionuclide-technique (RNT). Wear, Vol. 254, Nr. 9 (2003), pp. 801–817

[181] Birring, A. S. ; Kwun, H.: Ultrasonic measurement of wear. Tribology International, Vol. 22, Nr. 1 (1989), pp. 33–37

[182] Long, M. ; Rack, H. J.: Ultrasonic in situ continuous wear measurements of orthopaedic titanium alloys. Wear, Vol. 205, Nr. 1-2 (1997), pp. 130–136

[183] Matsuoka, K. ; Forrest, D. ; Ming-Kai, T.: On-line wear monitoring using acoustic emission. Wear, Vol. 162–164, Part A (1993), pp. 605–610

[184] Fan, K. C. ; Lee, M. Z. ; Mou, J. I.: On-Line Non-Contact System for Grinding Wheel Wear Measurement. International Journal of Advanced Manufacturing Technology, Vol. 19, Nr. 1 (2002), pp. 14–22

[185] Komanduri, R. ; Hou, Z.: A review of the experimental techniques for the measurement of heat and temperatures generated in some manufacturing processes and tribology. Tribology International, Vol. 34, Nr. 10 (2001), pp. 653-682

[186] Dulieu-Barton, J. ; Quinn, S. ; Boldetti, C. ; Pinna, C. ; Howard, I. ; Gutierrez, G.: Experimental measurement of the deformation in hot rolling of aluminium 1% Mn: the grid technique. Applied Mechanics and Materials, Vol. 3-4 (2005), pp 111-116

[187] Yi, J. ; Quiñónez, P. D.: Gear surface temperature monitoring. Proceedings of the Institution of Mechanical Engineers, Part J: Journal of Engineering Tribology, Vol. 219, Nr. 2 (2005), pp. 99–105

[188] Tian, X. ; Kennedy, F. E. ; Deacutis, J. J. ; Henning, A. K.: The Development and Use of Thin Film Thermocouples for Contact Temperature Measurement. Tribology Transactions, Vol. 35, Nr. 3 (1992), pp. 491–499

[189] Kennedy, F. E. ; Frusescu, D. ; Li, J.: Thin film thermocouple arrays for sliding surface temperature measurement. Wear, Vol. 207, Nr. 1-2 (1997), pp. 46-54

[190] Bowden, F. P. ; Ridler, K. E. W.: Physical Properties of Surfaces. III. The Sur-face Temperature of Sliding Metals The Temperature of Lubricated Surfaces. Proceedings of the Royal Society A: Mathematical, Physical and Engineering Sciences, Vol. 154, Nr. 883 (1936), pp. 640–656

[191] Chang, Y.: Tribo-electrification mechanisms for dissimilar metal pairs in dry severe wear process Part I. Effect of speed. Wear, Vol. 264, Nr. 11-12 (2008), pp. 1085–1094

[192] Chang, Y.: Tribo-electrification mechanisms for dissimilar metal pairs in dry severe wear process Part II. Effect of load. Wear, Vol. 264, Nr. 11-12 (2008), pp. 1095-1104

[193] Furey, M. J.: Surface Temperatures in Sliding Contact. A S L E Transactions, Vol. 7, Nr. 2 (1964), pp. 133–146

[194] Chang, Y. ; Chiou, Y. ; Lee, R.: The transition mechanisms of tribo-electrification for self-mated metals in dry severe wear process. Wear, Vol. 257, Nr. 3-4 (2004), pp. 347–358

[195] Thevenet, J. ; Siroux, M. ; Desmet, B.: Measurements of brake disc surface temperature and emissivity by two-color pyrometry. Applied Thermal Engineering, Vol. 30, Nr. 6-7 (2010), pp. 753–759

[196] Bowden, F. P. ; Thomas, P. H.: The Surface Temperature of Sliding Solids. Proceedings of the Royal Society A: Mathematical, Physical and Engineering Sciences, Vol. 223, Nr. 1152 (1954), pp. 29–40

[197] Siroux, M. ; Kasem, H. ; Thevenet, J. ; Desmet, B. ; Dufrenoy, P.: Local temperatures evaluation on the pin–disc interface using infrared metrology. International Journal of Thermal Sciences, Vol. 50, Nr. 4 (2011), pp. 486-492

[198] Suzuki, S. ; Kennedy, F. E.: The Detection of Flash Temperatures in a Sliding Contact by the Method of Tribo-Induced Thermoluminescence. Journal of Tribology, Vol. 113, Nr. 1 (1991), pp. 120-127

[199] Wright, P. K. ; Trent, E. M.: Metallographic Methods for Determining Temperature Gradients in Cutting Tools. Journal of the Iron and Steel Institute, Vol. 211, Nr. 5 (1973), pp. 364–368

[200] Mikroskopie Grundlagen Universität Wien. URL: http://www.univie.ac.at/mikroskopie/1_grundlagen/optik/opt_instrumente/6_grenzen.htm. Retrieved 2013-06-22

[201] Zabel, H.: Vorlesungsskript Experimentalphysik WS 10-11. URL: http://www.ep4.rub.de/imperia/md/content/skripte/ws10-11/medipol/37_lek_mikroskop.pdf. Retrieved 2013-06-25

[202] Shaha, K. P. ; Pei, Y. T. ; Martinez, D. ; Hosson, J. T. M.: Influence of Surface Roughness on the Transfer Film Formation and Frictional Behavior of TiC/a-C Nanocomposite Coatings. Tribology Letters, Vol. 41, Nr. 1 (2010), pp. 97-101

[203] Pawley, J.: Handbook of biological confocal microscopy. New York,: Springer, 2006. ISBN 9780387259215

[204] Kreis, T.: Handbook of holographic interferometry optical and digital methods. Weinheim: Wiley-VCH, 2005. ISBN 3527604928

[205] Korres, S. ; Feser, T. ; Dienwiebel, M.: In situ observation of wear particle formation on lubricated sliding surfaces. Acta Materialia, Vol. 60, Nr. 1 (2012), pp. 420-429

[206] Yu, L. ; Bahadur, S.: An investigation of the transfer film characteristics and the tribological behaviors of polyphenylene sulfide composites in sliding against tool steel. Wear, Vol. 214, Nr. 2 (1998), pp. 245–251

[207] Williams, D. B. ; Carter, C. B.:Transmission Electron Microscopy. New York: Springer, 1996. ISBN 978-0-306-45324-3

[208] Anantheshwara, K. ; Bobji, M. S.: In situ transmission electron microscope study of single asperity sliding contacts. Tribology International, Vol. 43, Nr. 5-6 (2010), pp. 1099–1103

[209] Meyer, E.: Atomic force microscopy. Progress in Surface Science, Vol. 41, Nr. 1 (1992), pp. 3–49

[210] Cleveland, J. P. ; Anczykowski, B. ; Schmid, A. E. ; Elings, V. B.: Energy dissipation in tapping-mode atomic force microscopy. Applied Physics Letters, Vol. 72, Nr. 20 (1998), pp. 2613-2615

[211] Chunzeng, L.: Lecture Notes: PeakForce Tapping Mode AFM and Quantitative Nanomechanical Measurements. University of Science and Technology Bejing, 2010

[212] Binnig, G. ; Quate, C. F.: Atomic Force Microscope. Physical Review Letters, Vol. 56, Nr. 9 (1986), pp. 930–933

[213] Randall, N. X. ; Bozet, J. L.: Nanoindentation and scanning force microscopy as a novel method for the characterization of tribological transfer films. Wear, Vol. 212, Nr. 1 (1997), pp. 18–24

[214] Bhushan, B.: Nanoscale tribophysics and tribomechanics. Wear, Vol. 225-229, Part 1 (1999), pp. 465–492

[215] Bhushan, B.: Micro/nanotribology using atomic force microscopy/friction force microscopy: state of the art. Proceedings of the Institution of Mechanical Engineers, Part J: Journal of Engineering Tribology, Vol. 212, Nr. 1 (1998), pp. 1-18

[216] Meyer, E. ; Lüthi, R. ; Howald, L. ; Güntherodt, H. J. ; Güntherodt H. J. ; Anselmetti D. ; Meyer E.: Forces in Scanning Probe Methods. Dordrecht: Springer Netherlands, 1995. ISBN 978-94-010-4027-3

[217] VDI 2602-2, Verein Deutscher Ingenieure (2008)

[218] Kasem, H. ; Bonnamy, S. ; Berthier, Y. ; Jacquemard, P.: Characterization of surface grooves and scratches induced by friction of C/C composites at low and high temperatures. Tribology International, Vol. 43, Nr. 11 (2010), pp. 1951-1959

[219] Neder, Z. ; Varadi, K. ; Friedrich, K.: Quantitative evaluation of wear grooves in a fine particulate reinforced soft polymer coating system by laser profilometry and computer aided scratch analysis. Advanced composites letters, Vol. 9, Nr. 5 (2000), pp. 315-328

[220] Barkoula, N. M. ; Karger-Kocsis, J.: Solid particle erosion of unidirectional GF reinforced EP composites with different fiber/matrix adhesion. Journal of reinforced plastics and composites, Vol. 21, Nr. 15 (2002), pp. 1377-1388

[221] Kok, Y. N. ; Akid, R. ; Hovsepian, P. E.: Tribocorrosion testing of stainless steel (SS) and PVD coated SS using a modified scanning reference electrode technique. Wear, Vol. 259, Nr. 7-12 (2005), pp. 1472–1481

[222] Laux, K. A. ; Schwartz, C. J.: Effects of contact pressure, molecular weight, and supplier on the wear behavior and transfer film of polyetheretherketone (PEEK). Wear, Vol. 297, Nr. 1-2 (2013), pp. 919–925

[223] Neslen, C. L. ; Mall, S. ; Sathish, S.: Nondestructive Characterization of Fretting Fatigue Damage. Journal of Nondestructive Evaluation, Vol. 23, Nr. 4 (2004), pp. 153–162

[224] Matikas, T. E. ; Shell, E. B. ; Nicolaou, P. D. ; Baaklini, G. Y. ; Nove, C. A. ; Boltz, E. S.: Characterization of fretting fatigue damage using nondestructive approaches. USA, Newport Beach: Proceedings of SPIE 3585, Nondestructive Evaluation of Aging Materials and Composites III (1999), pp. 2–10

[225] Colthup, N. B.: Introduction to infrared and Raman spectroscopy. Boston: Academic Press, 1990. ISBN 012182554X

[226] Chang, C. C.: Auger electron spectroscopy. Surface Science, Vol. 25, Nr. 1 (1971), pp. 53–79

[227] Agarwal, B. K.: X-ray spectroscopy: an introduction. Berlin: Springer-Verlag, 1991. ISBN 3540507191

[228] Das, S.: Nuclear magnetic resonance spectroscopy. Resonance, Vol. 9, Nr. 1 (2004), pp. 34–49

[229] Lee, K. H. ; Inoue, Y. ; Sugimura, H. ; Takai, O.: Correlation between wear-resistance and chemical structure of CNx films synthesized by shielded arc ion plating. Surface and Coatings Technology, Vol. 169–170 (2003), pp. 336-339

[230] Lauer, J. L. ; Vlcek, B. L.: Tribology of ceramic and metallic surface in environments of carbonaceous gases - Application of raman and infrared spectrosco-pies. ACS symposium series, Vol. 485 (1992), pp. 112–142

[231] Erdemir, A. ; Bindal, C. ; Fenske, G. R. ; Zuiker, C. ; Wilbur, P.: Characterization of transfer layers forming on surfaces sliding against diamond-like carbon. Surface and Coatings Technology, Vol. 86–87, Part 2 (1996), pp. 692-697

[232] Brainard, W. A. ; Buckley, D. H.: Adhesion and friction of PTFE in contact with metals as studied by Auger spectroscopy, field ion and scanning electron microscopy. Wear, Vol. 26, Nr. 1 (1973), pp. 75–93

[233] Hamilton, G. M. ; Moore, S. L.: Measurement of the oil-film thickness between the piston rings and liner of a small diesel engine. Proceedings of the Institution of Mechanical Engineers, Vol. 188 (1974), pp. 253–261

[234] Visscher, M.: The Measurement of the film thickness and the roughness deformation of lubricated elastomers. Eindhoven, Universität Eindhoven, Ph.D. Thesis 1992

[235] Visscher, M. ; Kanters, A. F. C.: Literature review and discussion on measurements of leakage, lubricant film thickness and friction of reciprocating elasto-meric seals. Society of Tribologists and Lubrication Engineers, Vol. 46, Nr. 12 (1990), pp. 785–791

[236] Crook, A. W.: Elastohydrodynamic Lubrication of Rollers. Nature, Vol. 190 (1961), pp. 1182–1183

[237] Kreil, O.: Einfluss der Oberflächenstruktur auf Druckverteilung und Schmierfilmdicke im EHD-Kontakt. München, TU München, Ph.D. Thesis 2008

[238] Bhushan, B.: The Real Area of Contact in Polymeric Magnetic Media I: Critical Assessment of Experimental Techniques. A S L E Transactions, Vol. 28, Nr. 1 (1985), pp. 75–86

[239] Sick, J. H. ; Ostermeyer, G. P.: In situ measurement of contact area in coated surfaces. Computer Methods and Experimental Measurements for Surface Effects and Contact Mechanics VIII, Vol. 55 (2007), pp. 259–270

[240] Totten, G. ; Wedeven, L. ; Anderson, M. ; Dickey, J. ; Jonsson, U. ; Larsson, R. ; Marklund, O. ; Eriksson, E. ; Uusitalo, O.: The Luleå Ball and Disc Apparatus (eds.). Bench Testing of Industrial Fluid Lubrication and Wear Properties Used in Machinery Applications. West Conshohocken: ASTM, 2001. ISBN 0803128673

[241] Guo, F. ; Wong, P. L. ; Fu, Z. ; Ma, C.: Interferometry Measurement of Lubricating Films in Slider-On-Disc Contacts. Tribology Letters, Vol. 39, Nr. 1 (2010), pp. 71–79

[242] Glovnea, R. P. ; Forrest, A. K. ; Olver, A. V. ; Spikes, H. A.: Measurement of Sub-Nanometer Lubricant Films Using Ultra-Thin Film Interferometry. Tribology Letters, Vol. 15, Nr. 3 (2003), pp. 217–230

[243] Meyer, F. ; Loyen, C. J.: The creep of oil on steel followed by ellipsometry. Wear, Vol. 33, Nr. 2 (1975), pp. 317–323

[244] Cavdar, B. ; Ludema, K. C.: Dynamics of dual film formation in boundary lubrication of steels part I. Functional nature and mechanical properties. Wear, Vol. 148, Nr. 2 (1991), pp. 305–327

[245] Cann, P. ; Spikes, H.: In Lubro Studies of Lubricants in EHD Contacts Using FTIR Absorption Spectroskopie. Tribology Transactions, Vol. 34, Nr. 2 (1991), pp. 248-256

[246] Gabelli, A. ; Poll, G.: Formation of Lubricant Film in Rotary Sealing Contacts: Part I—Lubricant Film Modeling. Journal of Tribology, Vol. 114, Nr. 2 (1992), pp. 280-287

[247] Bhushan, B. ; Dugger, M. T.: Real contact area measurements on magnetic rigid disks. Wear, Vol. 137, Nr. 1 (1990), pp. 41–50

[248] Down, M. ; Jiang, L. ; McBride, J. W.: An experimental analysis of the real contact area between an electrical contact and a glass plane. Singapore, Singapore: Proceedings of the icOPEN2013 (2013)

[249] Hendriks, C. P. ; Visscher, M.: Accurate Real Area of Contact Measurements on Polyurethane. Journal of Tribology, Vol. 117, Nr. 4 (1995), pp. 607-611

[250] Ovcharenko, A. ; Halperin, G. ; Etsion, I. ; Varenberg, M.: A novel test rig for in situ and real time optical measurement of the contact area evolution during pre-sliding of a spherical contact. Tribology Letters, Vol. 23, Nr. 1 (2006), pp. 55–63

[251] Boyes, W.: Instrumentation reference book. Amsterdam: Elsevier, 2010. ISBN 9780080941882

[252] eddyNCDT 3300 Datasheet, MICRO-EPSILON MESSTECHNIK GmbH & Co. KG

[253] Application Note on Eddy Current Sensors, MICRO-EPSILON MESSTECHNIK GmbH & Co. KG 2013

[254] Zhang, J. ; Drinkwater, B. W. ; Dwyer-Joyce, R. S.: Monitoring of Lubricant Film Failure in a Ball Bearing Using Ultrasound. Journal of Tribology, Vol. 128, Nr. 3 (2006), pp. 612-618

[255] Dwyer-Joyce, R. S. ; Green, D. A. ; Harper, P. ; Lewis, R. ; Balakrishnan, S. ; King, P. D. ; Rahnejat, H. ; Howell-Smith, S.: The Measurement of Liner - Piston Skirt Oil Film Thickness by an Ultrasonic Means. USA: Detroit: Proceedings of the SAE International Congress (2006)

[256] Gasni, D.: Ultrasonic Reflection for Measurement of Oil Film Thickness and Contact between Dissimilar Materials. Sheffield, The University of Sheffield, Ph.D. Thesis 2012

[257] Tribosonics LtD. URL: http://www.tribosonics.com/. Retrieved 2013-06-30

[258] Baltazar, A. ; Kim, J. ; Rokhlin, S.: Ultrasonic determination of real contact area of randomly rough surfaces in elastoplastic contact. Revista mexicana de física, Vol. 52, Nr. 1 (2006), pp. 37–47

[259] Koinkar, V. N. ; Bhushan, B.: Micro/nanoscale studies of boundary layers of liquid lubricants for magnetic disks. Journal of Applied Physics, Vol. 79, Nr. 10 (1996), pp. 8071-8075

[260] Bhushan, B.: Handbook of micro/nanotribology. Boca Raton: CRC Press, 1999. ISBN 0849384028

[261] Vick, B. ; Schneck, W. C.: Estimation of the Real Area of Contact in Sliding Systems Using Thermal Measurements. Journal of Tribology, Vol. 133, Nr. 3 (2011) pp. 031407-1 - 031407-12

[262] Schneck III, W. C.: Estimation of the Real Area of Contact in Sliding Systems Using Thermal Measurements. Blacksburg, Virginia Polytechnic Institute and State University, Ph.D. Thesis 2009

[263] ConfocalDT Product Overview, MICRO-EPSILON MESSTECHNIK GmbH & Co. KG (Retrieved 2013)

[264] Haynes, W. M. ; Lide, D. R.: CRC handbook of chemistry and physics a ready-reference book of chemical and physical data: 2011-2012. New York: CRC Press, 2011. ISBN 9781439855119

[265] Macherauch, E. ; Zoch, H. W.: Praktikum in Werkstoffkunde. Wiesbaden: Vieweg+Teubner, 2011. ISBN 383480343X

[266] Fluke 8845A/8846A Manual, Fluke Deutschland GmbH

[267] Pelster, R. ; Pieper, R. ; Hüttl, I.: Thermospannungen - Viel genutzt und fast immer falsch erklärt. Physik und Didaktik in Schule und Hochschule, Vol. 1, Nr. 4 (2005), pp. 10–22

[268] Bentley, R. E.: Handbook of temperature measurement. New York: Springer, 1998. ISBN 9814021121

[269] Chiou, Y. C. ; Chang, Y. P. ; Lee, R. T.: Tribo-Electrification Mechanism for Self-Mated Metals in Dry Severe Wear Process - Part I. Pure Hard Metals. Wear, Vol. 254, Nr. 7-8 (2003), pp. 606–615

[270] 100Cr6 Material Data. URL: http://www.dew-stahl.com/fileadmin/files/dew-stahl.com/documents/Publikationen/Werkstoffdatenblaetter/Baustahl/1.3505_de.pdf. Retrieved 2013-07-02

[271] Kramme, R.: Medizintechnik. Berlin: Springer, 2011. ISBN 978-3-642-16186-5

[272] thermoIMAGER TIM Product Overview, MICRO-EPSILON MESSTECHNIK GmbH & Co. KG (Retrieved 2013)

[273] Oster, F. ; Haupert, F. ; Friedrich, K. ; Müller, M. ; Bickle, W.: Neuartige Polyetheretherketon (PEEK)-Beschichtungen für hohe tribologische Beanspruchungen. Materialwissenschaft und Werkstofftechnik, Vol. 35, Nr. 10-11 (2004), pp. 690–695

[274] E37 Committee: Test Method for Thermal Conductivity of Solids by Means of the Guarded-Comparative-Longitudinal Heat Flow Technique. ASTM E1225 - 13 (2013)

[275] DIN EN ISO 3915; Measurement of resistivity of conductive plastics. (1999)

[276] Roberts, R. B.: The absolute scale of thermoelectricity II. Philosophical Magazine Part B, Vol. 43, Nr. 6 (1981), pp. 1125–1135

[277] FRT CWL 300 Datasheet, FRT Fries Research & Technology GmbH

[278] 100Cr6 Datasheet, GRUPPO LUCEFIN S.P.A.

[279] Oster, F.: Hochtemperaturbeständige Polymer-Beschichtungen für tribologische Anwendungen. Kaiserslautern, TU Kaiserslautern, Ph.D. Thesis 2005

[280] Kalin, M. ; Vižintin, J.: Comparison of different theoretical models for flash temperature calculation under fretting conditions. Tribology International, Vol. 34, Nr. 12 (2001), pp. 831–839

[281] Materialdaten AS-4 Carbon Fiber Datasheet, Hexcel (2013)

10. List of Publications

Poster

[1] Sebastian, R.; Noll, A.; Zhang, G.; Burkhart, T.; Wetzel, B.: Friction and wear of PPS/CNT nanocomposites with formation of electrically isolating transfer films. Kaiserslautern: IVW Kolloquium, November 2012

Conferences

[1] Sebastian, R. ; Noll, A. ; Zhang, G. ; Burkhart, T. ; Wetzel, B.: Friction and wear of PPS/CNT nanocomposites with formation of electrically isolating transfer films. Paris: JEC Composites Exhibition, March 2013

[2] Sebastian, R. ; Noll, A. ; Zhang, G. ; Burkhart, T. ; Wetzel, B.: Tribologische Eigenschaften von PPS/CNT Verbundwerkstoffen unter Berücksichtigung der elektrischen Isolationswirkung von Transferfilmen. Göttingen: GFT Conference, September 2012

[3] Sebastian, R. ; Burkhart, T. ; Wetzel, B.: Nano-Functionalized Polymercomposite Bearings for High-End Applications. Kaiserslautern: IVW Kolloquium, November 2012

[4] Cieslik, F. ; Luther, R. ; Rausch, J. ; Sebastian, R. ; Reinicke, R.: Tribologisches Verhalten und Einsatzmöglichkeiten von CNTs in PTFE-basierten Gleitlagern. Göttingen: GFT Conference, September 2013

[5] Cieslik, F. ; Reinicke, R. ; Scherge, M. ; Böttcher, R. ; Luther, R. ; Rausch, J. ; Sebastian, R. ; Pfeiffer, N. ; Burkhardt, T. ; Wuchter, M. ; Schrödter, J.: CarboSlide - CNT für ein Gleitlager mit optimierten Reibungseigenschaften. Fellbach: InnoCNT Congress, February 2013

Journal Publications

[1] Sebastian, R. ; Noll, A. ; Zhang, G. ; Burkhart, T. ; Wetzel, B.: Friction and wear of PPS/CNT nanocomposites with formation of electrically isolating transfer films. Tribology International, vol. 64 (2013), pp. 187–195

[2] Zhang, G. ; Sebastian, R. ; Burkhart, T. ; Friedrich, K.: Role of monodispersed nanoparticles on the tribological behavior of conventional epoxy composites filled with carbon fibers and graphite lubricants. Wear, vol. 292–293 (2012), pp. 176–187

Patents

[1] Sebastian, R. ; Burkhart, T.: Gleitkontaktelement sowie ein Verfahren zur Bestimmung der Temperatur im Bereich des Gleitkontaktes eines ungeschmierten Gleitkontaktelementes in dessen Betriebszustand. DE 10 2012 107 663 B3

11. List of Supervised Student Research and Graduation Projects

1. Liebrecht, J.: Konstruktion und Aufbau eines Prüfstandes für Sitzlehnenversteller, IVW-Bericht 12-049, Institut für Verbundwerkstoffe GmbH, Kaiserslautern, Diplomarbeit, 2012

2. Nguyen, T.-B.: Charakterisierung von Carbon Nanotube verstärktem Polyphthalamid, IVW-Bericht 13-009, Institut für Verbundwerkstoffe GmbH, Kaiserslautern, Studienarbeit, 2013

3. Kühn, F.: Konzeption und Konstruktion eines Hochlastprüfstandes für tribologische Prüfungen, IVW-Bericht 13-016, Institut für Verbundwerkstoffe GmbH, Kaiserslautern, Studienarbeit, 2013

4. Jim, B.-C.: Bestimmung von Reibstellentemperaturen bei tribologischen Modellprüfungen - Ein theoretischer, simulativer und experimenteller Ansatz, IVW-Bericht 13-083, Institut für Verbundwerkstoffe GmbH, Kaiserslautern, Diplomarbeit, 2013

5. Hoffmann, J.: Konfokales in-situ Vermessen von Transferfilmen in tribologischen Modellprüfungen, IVW-Bericht 13-092, Institut für Verbundwerkstoffe GmbH, Kaiserslautern, Studienprojekt, 2013